

Dissertation presented to the Instituto Tecnológico de Aeronáutica, in partial fulfillment of the requirements for the degree of Master of Science in the Graduate Program of Electronic and Computing Engineering, Field of Telecommunications.

João Pedro Turchetti Ribeiro

**CONCURRENT IMAGING MODE APPLIED TO
HIGH-RESOLUTION WIDE-SWATH SAR
IMAGING**

Dissertation approved in its final version by signatories below:

Prof. Dr. Renato Machado
Advisor

Thomas Kraus
Co-advisor

Prof. Dr. Emília Villani
Dean of Graduate Studies and Research

Campo Montenegro
São José dos Campos, SP - Brazil
2022

Cataloging-in Publication Data
Documentation and Information Division

Turchetti Ribeiro, João Pedro
Concurrent Imaging Mode Applied to High-Resolution Wide-Swath SAR Imaging / João Pedro Turchetti Ribeiro.
São José dos Campos, 2022.
129f.

Dissertation of Master of Science – Course of Electronic and Computing Engineering. Area of Telecommunications – Instituto Tecnológico de Aeronáutica, 2022. Advisor: Prof. Dr. Renato Machado. Co-advisor: Thomas Kraus.

1. Synthetic Aperture Radar (SAR). I. Instituto Tecnológico de Aeronáutica. II. Title.

BIBLIOGRAPHIC REFERENCE

TURCHETTI RIBEIRO, João Pedro. **Concurrent Imaging Mode Applied to High-Resolution Wide-Swath SAR Imaging**. 2022. 129f. Dissertation of Master of Science – Instituto Tecnológico de Aeronáutica, São José dos Campos.

CESSION OF RIGHTS

AUTHOR'S NAME: João Pedro Turchetti Ribeiro

PUBLICATION TITLE: Concurrent Imaging Mode Applied to High-Resolution Wide-Swath SAR Imaging.

PUBLICATION KIND/YEAR: Dissertation / 2022

It is granted to Instituto Tecnológico de Aeronáutica permission to reproduce copies of this dissertation and to only loan or to sell copies for academic and scientific purposes. The author reserves other publication rights and no part of this dissertation can be reproduced without the authorization of the author.

João Pedro Turchetti Ribeiro
Rua Elesbão Linhares, 394
29.055-340 – Vitória-ES

CONCURRENT IMAGING MODE APPLIED TO HIGH-RESOLUTION WIDE-SWATH SAR IMAGING

João Pedro Turchetti Ribeiro

Thesis Committee Composition:

Prof. Dr.	Felix Dieter Antreich	Chairperson	-	ITA
Prof. Dr.	Renato Machado	Advisor	-	ITA
	Thomas Kraus	Co-advisor	-	DLR
Prof. Dr.	Dimas Irion Alves	Internal member	-	ITA
Dr.	Michelangelo Villano	External member	-	DLR
Dr.	Rafael Antonio da Silva Rosa	External member	-	Visiona

This paper is dedicated to my mentors and friends at DLR and ITA under whose constant guidance I have completed this thesis. They not only enlightened me with academic knowledge but also gave me valuable advice whenever I needed it the most.

Acknowledgments

First and foremost I would like to express my deepest gratitude to my parents – Maria Isabel Duarte Turchetti and João Carlos Magalhães Ribeiro –, not only for providing me with the best education, but also for encouraging me to pursue seemingly impossible challenges. None of this would have been possible without their support. I extend my gratitude to my girlfriend, brother and the rest of the family for always being truly supportive.

I would like to give special thanks to my co-advisor Thomas Kraus for receiving me at DLR and being extremely helpful and accessible. He is the responsible for guiding me, a previously illiterate in SAR technology, all the way to what is presented in this thesis. Similarly, I am very grateful for having Prof. Renato Machado as my advisor, who always enthusiastically gave me valuable advice and guidance to my academic life. I am forever grateful for the partnership between ITA and DLR made possible by my advisors.

Last but not least, I would like to thank everyone that has been part of my journey. Teachers, professors and friends from the schools and institutions I studied since young are immeasurably responsible for what I am today. This thesis is certainly the outcome of very hard work not only mine, but of everyone involved.

*“A ship in harbor is safe,
but that is not what ships are built for.”*

— J. A. SHEDD

Resumo

Radar de abertura sintética (SAR) está gradualmente se tornando a referência no imageamento da superfície terrestre devido à sua funcionalidade em qualquer condição climática e independência da luz solar. A sua crescente qualidade de imagem atrelada às capacidades de polarimetria, interferometria e tomografia o tornam uma solução tecnológica bastante atrativa para o monitoramento contínuo de fenômenos globais (tais como derretimento de geleiras, desmatamento e cobertura de gelo marítimo), vigilância, agricultura e outras diversas aplicações. Dessa forma, o imageamento de faixas largas com alta resolução (HRWS) é uma linha de pesquisa essencial para a futura geração de sistemas SAR.

Uma das técnicas recentemente propostas para aumentar a capacidade e flexibilidade dos sistemas é o modo de imageamento simultâneo. Esse modo permite aquisições simultâneas de duas áreas por meio do aumento da frequência de repetição de pulso e intercalando a transmissão e recepção de ambos os modos pulso a pulso. Devido a limitações intrínsecas de sistema, essa técnica aplicada a sistemas operacionais atuais, tal como o satélite alemão TerraSAR-X, apresenta fortes compromissos em termos de uma largura de faixa mais limitada e um aumento dos níveis de ambiguidade.

Nesta dissertação de mestrado, várias técnicas são investigadas a fim de aprimorar o modo de imageamento simultâneo considerando o escopo da próxima geração de sistemas SAR. Dado que esses sistemas ainda estão em desenvolvimento e não há restrições estritas sobre o que está disponível, uma vasta gama de tecnologias e possibilidades são analisadas neste trabalho, como multiplexação por divisão de frequência ortogonal (OFDM), varredura de frequência (F-Scan) e técnica de antena de centros de fase deslocada (DPCA). O F-Scan demonstrou cumprir bem os requisitos, alcançando melhorias significativas não apenas no desempenho do alcance, mas também no tamanho da cena, tudo isso em um sistema relativamente simples e barato. Finalmente, simulações de desempenho global e previsões de melhoria são realizadas no âmbito da próxima missão alemã em banda X HRWS, que está planejada para usar o F-Scan operacionalmente.

Abstract

Synthetic aperture radar (SAR) is gradually becoming mainstream for imaging of the Earth's surface due to its all-weather day-and-night functionality. Its increasing image quality tied to the capabilities of polarimetry, interferometry, and tomography turns it into a very attractive technology for a continuous monitoring of global phenomena (such as glacier retreat, deforestation, and sea ice coverage), surveillance, farming and numerous other applications. Therefore, imaging wide swaths with high resolution (HRWS) is a key line of research for the future generation of SAR systems.

One of the recently proposed techniques to increase imaging capability and flexibility is the concurrent imaging mode. This mode allows for simultaneous acquisitions of two areas by increasing the pulse repetition frequency and interleaving the transmission and reception of both modes in a pulse-to-pulse manner. Due to intrinsic system limitations, this technique applied to current operational systems, such as the German satellite TerraSAR-X, comes along with strong trade-offs in terms of limited swath width and increased ambiguity levels.

In this Master's thesis, multiple techniques are investigated to improve the concurrent mode within the scope of the next generation of SAR systems. Given that those systems are still under development and there is no strict restriction on what is available, a vast range of technologies and possibilities are analyzed in this work, such as orthogonal frequency division multiplexing (OFDM), frequency scanning (F-Scan), and displaced phase centers antenna (DPCA) technique. F-Scan is shown to comply well with the requirements, achieving significant improvements not only in range performance but also in scene size, all of this under a relatively simple and inexpensive system. Finally, global performance simulations and improvement predictions are carried out within the framework of the upcoming German X-Band HRWS mission, which is planned to use F-Scan operationally.

List of Figures

FIGURE 2.1 – Schematic visualization of a SAR acquisition geometry.	24
FIGURE 2.2 – Schematic plot in time of the transmit and receive signals for a PRF of 3100 Hz, an incidence angle of 38° , a platform height of 519 km and a duty cycle of 18 %.	27
FIGURE 2.3 – Timing diagram as a function of the incidence angle for a satellite height of 519 km and duty cycle of 18 %.	28
FIGURE 2.4 – Visualization of a scenario with range ambiguities.	30
FIGURE 2.5 – Visualization of the target position and the range ambiguities on the normalized adjusted antenna pattern in elevation for an exemplary acquisition of a target at an incidence angle of 39° with a PRF of 3000 Hz.	32
FIGURE 2.6 – Visualization of the target position and the range ambiguities on the normalized adjusted antenna pattern in elevation for an exemplary acquisition of a target at an incidence angle of 39° with a PRF of 6000 Hz.	33
FIGURE 2.7 – Visualization of the target position and the range ambiguities on the normalized adjusted antenna pattern in elevation for an exemplary acquisition of a target at an incidence angle of 39° with a PRF of 6000 Hz. The target is 12 km away from the scene center towards near range.	34
FIGURE 2.8 – Simulated RASR for the TerraSAR-X Stripmap mode at different range target positions with an incidence angle of 39° . The distance of the simulated target with respect to the scene center (Δ_{rg}) is provided in the legend.	35
FIGURE 2.9 – Visualization of strong range ambiguities on the River Plate near the city of Buenos Aires, Argentina. The ambiguities do not appear focused due to the alternation of up and down chirps on transmit. .	36

FIGURE 2.10 – Acquisition geometry in the slant range plane.	37
FIGURE 2.11 – Visualization of the target Doppler bandwidth and the azimuth ambiguities on the azimuth antenna pattern considering a PRF of 3000 Hz and an oversampling factor $\alpha_{os,a}$ of 1.0.	39
FIGURE 2.12 – Visualization of the target Doppler bandwidth and the azimuth ambiguities on the azimuth antenna pattern considering a PRF of 3000 Hz and an oversampling factor $\alpha_{os,a}$ of 1.4.	39
FIGURE 2.13 – AASR behavior for different azimuth oversampling factors and an antenna size of 4.8 m.	40
FIGURE 2.14 – Visualization of azimuth ambiguities on the Atlantic Ocean near the city of Piúma, Brazil. From left to right, the trade-off between azimuth resolution and AASR is depicted. The lower the Doppler processed bandwidth is, the better and less visible are the azimuth ambiguities.	41
FIGURE 3.1 – Summary of the trade-off between resolution and coverage of the current most typical SAR imaging modes.	45
FIGURE 3.2 – Illustration of the four channels split beam broadening of the DPCA technique.	49
FIGURE 3.3 – Illustration of the uniform sampling achieved by the half antenna displacement of the platform from PRI to PRI.	49
FIGURE 3.4 – Interpolated spectra of the waveforms proposed by Kim for a pulse duration of 100 μ s.	52
FIGURE 3.5 – Schematic comparing the acquisitions for conventional Stripmap SAR mode with the F-Scan. Conventional Stripmap employs a broad beam and receives first from near range. F-Scan, conversely, sweeps across ground range with a pencil beam by linearly increasing the chirp frequency. As a result, the echoes overlap on receive.	55
FIGURE 4.1 – WGS-84 Coordinate System Definition (NATIONAL IMAGERY AND MAPPING AGENCY, 2000).	59
FIGURE 4.2 – F-Scan instantaneous transmit frequency in terms of fast time and look angle of the peak of the main lobe.	61
FIGURE 4.3 – Angular scanning of the F-Scan highlighting the effective imaged scene in contrast to the total imaged area.	62
FIGURE 4.4 – Spherical Earth representation of a SAR acquisition.	63

FIGURE 4.5 – Echo delay as a function of the look angle.	64
FIGURE 4.6 – Reception of the echoes in the time by slant range domain for a fully-overlapped acquisition.	66
FIGURE 4.7 – Reception of the echoes in the slant range by frequency domain for a fully-overlapped acquisition.	67
FIGURE 4.8 – Reception of the echoes in the time by frequency domain for a fully-overlapped acquisition.	67
FIGURE 4.9 – Reception of the echoes in the time by frequency domain for partially-overlapped acquisitions.	68
FIGURE 4.10 – Maximum PRF from a timing point of view of an F-Scan acquisition in comparison with a traditional Stripmap as a function of the pulse duration. The region of interest due to duty cycle and SNR limitation is in green.	70
FIGURE 4.11 – Schematic amplitude representation of the events of a concurrent acquisition in time. The targets are 330 km apart.	72
FIGURE 4.12 – Schematic frequency representation of the events of a concurrent acquisition in time. The targets are 330 km apart.	72
FIGURE 4.13 – Interference matrices for concurrent acquisitions with F-Scan portraying the available PRF combinations and the interference events. The allowed areas are indicated by the white and pink colors. On the left two scenes with 20 km of swath width are considered, while on the right the swaths are increased to 30 km.	75
FIGURE 4.14 – Interference events achieved by varying the duty cycles of each mode. The scenes have a swath width of 30 km, near range incidence angles of 31.50° and 54.57° , and the PRFs used are 5650 Hz and 4600 Hz.	76
FIGURE 4.15 – Schematic frequency representation of the events of a concurrent acquisition in time. The duty cycles have been maximized to improve the efficiency of the time domain usage.	77
FIGURE 4.16 – Schematic representation of the antenna considered in this thesis.	78
FIGURE 4.17 – Linear phased-array considered to derive the antenna patterns.	79
FIGURE 4.18 – Theoretical antenna pattern in azimuth if isotropic elements were considered.	82
FIGURE 4.19 – Theoretical antenna pattern in azimuth at boresight.	83
FIGURE 4.20 – Theoretical antenna pattern in azimuth for a $+1^\circ$ steering.	84

FIGURE 4.21 –Frequency scanning for two arbitrary scenarios. On the upper plot, the antenna is sweeping from the look angles 35.8° to 31.8° . On the lower plot, the scan is from 49.8° to 43.8° . The plot highlights the nearly linear frequency scanning.	87
FIGURE 4.22 –Theoretical antenna pattern in elevation for a steering of 15° and a frequency of 9.8 GHz.	88
FIGURE 4.23 –Theoretical antenna frequency scanning in elevation for a sweeping from $+3^\circ$ to -3°	89
FIGURE 4.24 –Azimuth ambiguity-to-signal ratio for Stripmap acquisitions with a 6.0 m phased-array antenna with 12 elements. A Hamming window with $\alpha = 0.6$ and multiple oversampling factors ($\alpha_{os,a}$) are considered.	90
FIGURE 4.25 –Time by frequency plot for an arbitrary acquisition. The objective of this representation is to facilitate the understanding of the origin of the ambiguities in a concurrent F-Scan scenario.	92
FIGURE 4.26 –Time by frequency plot for an arbitrary acquisition in which the SM echoes are received in the ST echo window, and vice-versa.	93
FIGURE 4.27 –SM same mode range ambiguity and target areas for a concurrent F-Scan imaging with PRFs 5650 Hz and 4600 Hz. The near range targets are at look angles of 28.9° (SM) and 48.9° (ST).	96
FIGURE 4.28 –ST same mode range ambiguity and target areas for a concurrent F-Scan imaging with PRFs 5650 Hz and 4600 Hz. The near range targets are at look angles of 28.9° (SM) and 48.9° (ST).	96
FIGURE 4.29 –SM cross mode range ambiguity areas for a concurrent F-Scan imaging with PRFs 5650 Hz and 4600 Hz. The near range targets are at look angles of 28.9° (SM) and 48.9° (ST).	97
FIGURE 4.30 –ST cross mode range ambiguity areas for a concurrent F-Scan imaging with PRFs 5650 Hz and 4600 Hz. The near range targets are at look angles of 28.9° (SM) and 48.9° (ST).	98
FIGURE 4.31 –SM RASR assessment as a function of the PRFs for a concurrent F-Scan acquisition with targets at look angles of 28.9° (SM) and 48.9° (ST).	99
FIGURE 4.32 –ST RASR assessment as a function of the PRFs for a concurrent F-Scan acquisition with targets at look angles of 28.9° (SM) and 48.9° (ST).	99

FIGURE 5.1 – Target azimuth adjustment for an ascending orbit imaging.	102
FIGURE 5.2 – Target azimuth adjustment for a descending orbit imaging.	102
FIGURE 5.3 – Number of flyovers of the satellite over the target areas within one orbit cycle.	104
FIGURE 5.4 – Slant range resolution as a function of the incidence angle of the scene center for the simulated targets. The selected PRF is the highest available.	106
FIGURE 5.5 – Ground range resolution as a function of the incidence angle of the scene center for the simulated targets. The selected PRF is the highest available.	107
FIGURE 5.6 – Slant range resolution as a function of the distance between the simulated targets. The selected PRF is the highest available.	108
FIGURE 5.7 – RASR as a function of the incidence angle of the scene center for the simulated targets. The selected PRF is the highest available.	109
FIGURE 5.8 – RASR as a function of the distance between the simulated targets. The selected PRF is the highest available.	110
FIGURE 5.9 – RASR as a function of the slant range resolution of the simulated targets. The selected PRF is the highest available.	111
FIGURE 5.10 – Azimuth resolution as a function of the incidence angle of the scene center for the simulated targets. The selected PRF is the highest available.	112
FIGURE 5.11 – AASR as a function of the effective PRF used in the acquisitions. The selected PRF is the highest available.	113
FIGURE 5.12 – AASR as a function of the incidence angle of the scene center for the simulated targets. The selected PRF is the highest available.	114
FIGURE 5.13 – AASR as a function of the distance between the simulated targets. The selected PRF is the highest available.	114
FIGURE 5.14 – Latitude-distance bivariate distribution of the unavailable targets when DPCA is not considered.	115
FIGURE 5.15 – Slant range resolution as a function of the incidence angle of the scene center for the simulated targets. The selected PRF is the closest possible to the target DPCA.	116

FIGURE 5.16 –RASR as a function of the incidence angle of the scene center for the simulated targets. The selected PRF is the closest possible to the target DPCA.	117
FIGURE 5.17 –Azimuth resolution as a function of the incidence angle of the scene center for the simulated targets. The selected PRF is the closest possible to the target DPCA.	118
FIGURE 5.18 –AASR as a function of the effective PRF used in the acquisitions. The selected PRF is the closest possible to the target DPCA.	119
FIGURE 5.19 –Latitude-distance bivariate distribution of the unavailable targets when DPCA is considered.	120

List of Tables

TABLE 3.1 – Stripmap performance for X-Band state-of-the-art spaceborne systems.	47
TABLE 3.2 – ScanSAR performance for X-Band state-of-the-art spaceborne systems.	47
TABLE 3.3 – Staring Spotlight performance for X-Band state-of-the-art spaceborne systems.	47
TABLE 4.1 – WGS-84 primary ellipsoid parameters. (NATIONAL IMAGERY AND MAPPING AGENCY, 2000)	59
TABLE 6.1 – Summary of the performance improvement of the concurrent imaging mode achieved with the F-Scan and DPCA in comparison with traditional Stripmap mode (RIBEIRO <i>et al.</i> , 2022). The ambiguity ratios considered are the 90th percentile.	122

List of Abbreviations and Acronyms

AASR	Azimuth Ambiguity-to-Signal Ratio
DBF	Digital Beamforming
DPCA	Displaced Phase Center Antenna
FFT	Fast Fourier Transform
F-Scan	Frequency Scanning
HRWS	High-Resolution Wide-Swath
ICI	Inter-carrier Interference
ISLR	Integrated Sidelobe Ratio
LEO	Low Earth Orbit
MAPS	Multiple Azimuth Phase Centers
MIMO	Multiple-Input Multiple-Output
NESZ	Noise Equivalent Sigma Zero
OFDM	Orthogonal Frequency Division Multiplexing
PAPR	Peak-to-Average Power Ratio
PRF	Pulse Repetition Frequency
PRI	Pulse Repetition Interval
PSLR	Peak-to-Sidelobe Ratio
RASR	Range Ambiguity-to-Signal Ratio
RCS	Radar Cross-Section
RF	Radio Frequency
SAR	Synthetic Aperture Radar
SCORE	Scan-on-Receive
SNR	Signal-to-Noise Ratio
SM	Stripmap Mode
ST	Staring Spotlight Mode
STC	Space-time Coding
STSO	Short Term Shift Orthogonal
TOPSAR	Terrain Observation by Progressive Scans
TTDL	True Time Delay Line

List of Symbols

α	Hamming window factor
$\alpha_{os,a}$	Azimuth oversampling ratio
β	Look angle
δ_{az}	Azimuth resolution
δ_{rg}	Slant range resolution
Δf_d	Processed Doppler bandwidth
Δ_{rg}	Distance offset in range
γ_w	Broadening factor
λ	Wavelength of the carrier
σ_0	Backscatter coefficient
θ_i	Incidence angle
B_{eff}	Effective bandwidth
B_t	Total bandwidth
c_0	Speed of light in vacuum
f_s	Sampling frequency
f_d	Doppler frequency
L_a	Antenna length in azimuth
R	Slant range
R_0	Slant range of closest approach
t_p	Transmit pulse duration
v_g	Satellite ground speed
v_s	Satellite speed

Contents

1	INTRODUCTION	20
1.1	Context	20
1.2	Motivation	21
1.3	Objective	22
1.4	Thesis outline	22
2	SAR BACKGROUND	23
2.1	PRF Selection Criteria	24
2.2	Timing Diagram	26
2.3	Ambiguities	29
2.3.1	Range Ambiguity-to-Signal Ratio (RASR)	30
2.3.2	Azimuth Ambiguity-to-Signal Ratio (AASR)	36
3	HIGH-RESOLUTION WIDE-SWATH IMAGING	43
3.1	SAR Trade-offs	44
3.2	State-of-the-Art Systems and HRWS Imaging Requirements	46
3.3	Review of Technologies / Proposals for HRWS Imaging	48
3.3.1	Displaced Phase Center Antenna (DPCA)	48
3.3.2	Space-time Coding (STC)	50
3.3.3	Orthogonal Frequency Division Multiplexing (OFDM)	51
3.3.4	Scan-on-Receive (SCORE)	53
3.3.5	Frequency Scanning (F-Scan)	54
3.4	Concluding Remarks	56

4	CONCURRENT IMAGING WITH F-SCAN	58
4.1	HRWS System Parameters	58
4.1.1	Orbital Parameters	58
4.1.2	Platform Parameters	59
4.2	Concurrent F-Scan Timing and Interference Assessment	60
4.2.1	F-Scan Timing Considerations	60
4.2.2	Concurrent Imaging Timing Aspects with F-Scan	71
4.2.3	Interference Assessment	73
4.3	Antenna Modeling	77
4.3.1	Azimuth	78
4.3.2	Elevation	84
4.4	Concurrent F-Scan Ambiguity Calculations	89
4.4.1	Azimuth Ambiguities	89
4.4.2	Range Ambiguities	91
5	GLOBAL PERFORMANCE	101
5.1	Global Performance without DPCA	105
5.1.1	Range	105
5.1.2	Azimuth	111
5.1.3	Unavailable Acquisitions	115
5.2	Global Performance with DPCA	116
5.2.1	Range	116
5.2.2	Azimuth	117
5.2.3	Unavailable Acquisitions	119
6	CONCLUSION	121
6.1	Final Remarks	121
6.2	Outlook for Further Work	123
	BIBLIOGRAPHY	125

1 Introduction

1.1 Context

The term Synthetic Aperture Radar (SAR) refers to a radar imaging technique discovered and first made functional in 1952 by Dr. Carl Wiley at the Goodyear Aircraft Corporation (WILEY, 1985). Twenty-six years later, the first spaceborne satellite carrying a SAR sensor was made operational by the SEASAT mission in 1978. However, it is only since the ERS-1 launch in 1991 that SAR systems have been continuously orbiting and imaging the Earth's surface on a daily basis (CUMMING; WONG, 2005) (CURLANDER; MCDONOUGH, 1991). At the current state of the art, modern systems can acquire images with a resolution in the order of dozens of centimeters (MITTERMAYER *et al.*, 2014). Compared to optical imaging, SAR systems are well known for being all-weather, day and night operational. In other words, as these systems provide their own target illumination and can penetrate through clouds, they can acquire images regardless of bad weather or lack of sunlight.

The SAR technique is a technical improvement of the side-looking airborne radars (SLAR). The latter consists of a real aperture imaging technique that is unsuitable for space applications as very long antennas would be required to achieve reasonable azimuth resolution. To overcome this limitation, SAR systems synthesize a long aperture in azimuth by taking advantage of the relative movement between the target and the radar platform. For example, a virtual 10 km long antenna can be synthesized from a physical length of 10 m in the direction of flight (NASA, 2020). This improvement is enough to bring down the azimuth resolution of spaceborne systems from kilometers to a few meters, thus making the radar imaging implementation feasible.

To comply with different requirements, multiple imaging modes have been developed by the SAR community. These modes consist overall of a trade-off between resolution and image size. Namely, the Stripmap (SM), Staring Spotlight (ST), and ScanSAR (SC) are traditionally some of the operational modes of current state-of-the-art systems (CUMMING; WONG, 2005; CURLANDER; MCDONOUGH, 1991; MITTERMAYER *et al.*, 2014; EINEDER *et al.*, 2013).

The Stripmap and the Staring Spotlight modes are of most interest in this research and deserve a brief explanation in this section. The Stripmap is one of the most traditional and basic imaging modes and has been widely used since the ERS-1 mission. The main objective is to obtain a medium-resolution image – for instance, approximately 1.2 m in range and 3.3 m in azimuth for TerraSAR-X – of a long continuous strip of, theoretically, unlimited length and a swath width of 30 km. The Stripmap azimuth coverage, however, is usually limited by satellite constraints on available power, thermal conditions, and the amount of generated data. The Staring Spotlight mode improves the resolution to 0.6 m and 0.24 m in range and azimuth, respectively. However, the trade-off is a reduction in the scene size to a small patch of $4 \text{ km} \times 3.7 \text{ km}$ (EINER *et al.*, 2013).

1.2 Motivation

One of the limitations of the current state-of-the-art imaging modes is that only one mode can be used at a time. Due to the satellite’s orbit geometry, there is a long interval of up to 11 days (for TerraSAR-X) – a period of the satellite often called a repeat cycle – between consecutive flyovers of the radar to a given target on Earth under the same geometry. If two different acquisitions are required in nearby regions, then it may be necessary to wait up to two weeks. For instance, one could think of a requirement of imaging with sub-meter resolution the cities of Rio de Janeiro and São Paulo, or London and Amsterdam, which are roughly 350 km apart. Generally speaking, any two nearby sites of interest could be required in specific applications. One possible solution would be to deploy a constellation of satellites at different orbit positions so that there is a shorter interval between similar acquisitions. However, this solution is clearly not very cost-effective.

To overcome this physical restriction and increase the image output rate, a concurrent imaging mode was proposed for acquiring two SAR images simultaneously. The details can be found in (KRAUS *et al.*, 2022; RIBEIRO *et al.*, 2022). It was shown that quite some flexibility and increase in imaging capability could be achieved. Nevertheless, ambiguities were demonstrated to be one of the most critical parameters for concurrent acquisitions. Once the potentials and the drawbacks of the novel technique were clear and well established, motivation arose to investigate new technologies capable of improving the overall performance of the concurrent technique, concerning mainly range ambiguities, scene sizes, and imaging flexibility (availability and maximum distance between the areas being imaged).

1.3 Objective

Achieving simultaneous imaging capability of separated areas while maintaining operational performance can be extremely useful and convenient. Therefore, this research aims to improve the overall performance of the concurrent imaging technique. This involves investigating new technologies and their capacity to explore the concurrent imaging concept adequately. The main points of attention are to improve the ambiguity performance in range, and the scene size, without significantly sacrificing other parameters and with reasonable system costs. Ultimately, an evaluation of the novel imaging technique must be carried out to numerically assess and validate the improvements achieved by the proposed methods. The upcoming German X-Band HRWS system parameters will be considered in the simulations.

1.4 Thesis outline

The thesis is divided into six chapters. Chapter 1 introduces the topic, presenting the context, motivation, and objective of the research. Next, Chapter 2 elucidates the relevant SAR background; more specifically, it depicts concepts involved in the timing and ambiguity analyses, which are key to have a clear understanding of this research. Chapter 3 not only presents a literature review of the main technologies being investigated by the scientific community to achieve ever-increasing resolution and scene sizes but also analyzes the best-suited ones to the concurrent mode, taking into consideration performance improvements and implementation costs. A thorough explanation of the novel imaging mode is presented in Chapter 4. In Chapter 5, simulations of targets with randomized positions around the globe obtain the global performance prediction of the designed mode. Finally, Chapter 6 summarizes the thesis, highlighting the main contributions and suggesting possibilities for future work.

2 SAR Background

A SAR acquisition is a fast and highly complex event. A thorough description from scratch of all the parameters and decision making involved in the design of a system would require a dedicated thesis. For instance, mission requirements, hardware definitions, financial budget, power budget, antenna size, mechanical structure, number of satellites in the constellation, number of transmit and receive channels, imaging mode description, and PRF selection are just some of the many decisions and studies that must be carried out to achieve a final system. Each of these topics is a separate field of study, so that one must assume some system parameters to be given to narrow the investigation to a selection of topics.

This thesis will focus on the description of the imaging mode, which is tightly connected to the PRF selection. Consequently, timing constraints, ambiguities prediction and image quality are key in this research. The basic theoretical background required as a starting point to better understand the research is presented in this section. Moreover, some system parameters will eventually be summarily taken as given throughout the thesis. They will be defined, justified and assumed to hold true in order to derive further analyses.

The description of the geometry of a SAR acquisition is the very first step that has to be clear and well defined. Figure 2.1 depicts a schematic of a typical SAR acquisition geometry. The angles β and θ_i represent the look and the incidence angles, while h_s and \vec{v}_s are the height and the velocity of the platform. The Nadir track is defined by the perpendicular projection of the platform trajectory on the ground. Finally, slant range (SR or simply R) and ground range (GR) are two interchangeable domains by the relation

$$\text{GR} = \frac{\text{SR}}{\sin \theta_i}. \quad (2.1)$$

Typically when only the word ‘range’ is used, it refers to the slant range domain.

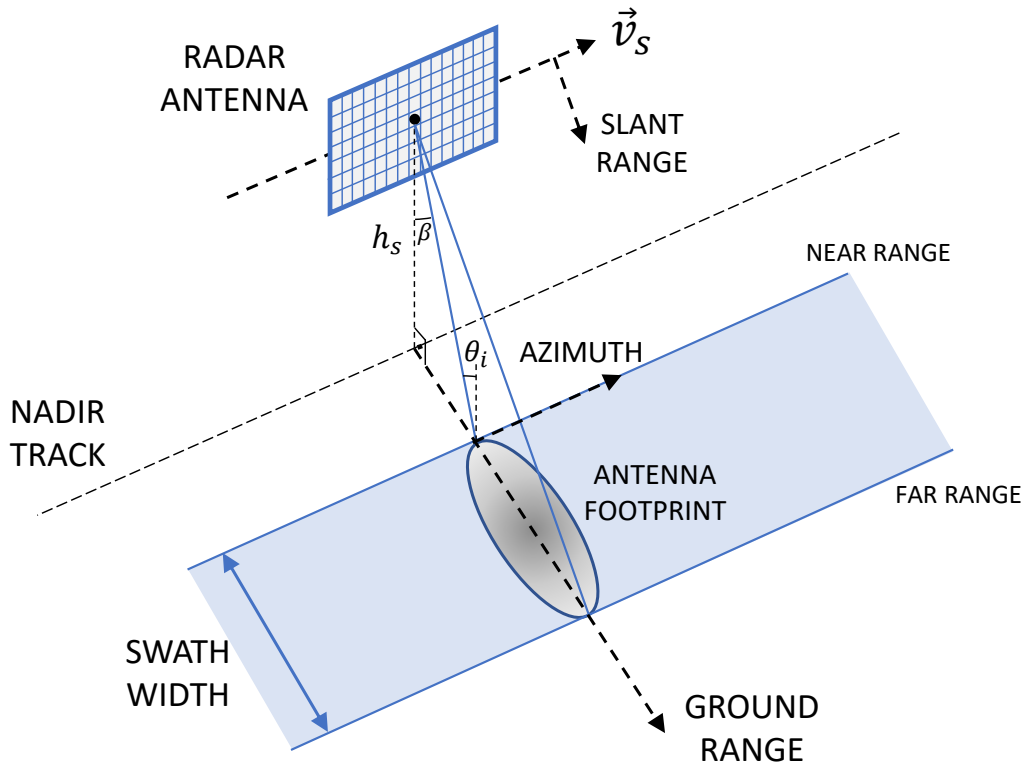


FIGURE 2.1 – Schematic visualization of a SAR acquisition geometry.

2.1 PRF Selection Criteria

One of the most important steps when designing a SAR acquisition is to determine an appropriate pulse repetition frequency (PRF). In monostatic systems, i.e., those in which the transmit and receive antenna are collocated (typically the same), the radar has to stop transmitting to receive the echoes from the imaged area. The PRF is defined as the rate in which this sequence of transmission and reception occurs. The total time between the rising edges of consecutive transmit pulses is the pulse repetition interval (PRI), and is obtained by

$$\text{PRI} = \frac{1}{\text{PRF}}. \quad (2.2)$$

The main constraints involved in the PRF selection are the satellite hardware, the required swath width and azimuth resolution, the Nadir and transmit interferences, the receive window timing, and the range and azimuth ambiguities (CUMMING; WONG, 2005). This section will discuss these factors and, as a final objective, try to clarify all the steps required to select the PRF for a SAR acquisition.

First, the satellite hardware constraints are defined mainly by its antenna and radar electronics limitations. In other words, if the transmission of the antenna can be switched on and off at the required rate and also if it can receive while switched off. Besides, it is also important to ensure that the electronics of the system and the on-board mass memory are capable of dealing with the amount of data defined by the PRF and the sampling rate, as a higher PRF leads to more data being fed into the memory. Lastly, all the acquired data has to be downlinked to the so-called ground stations. This is a special concern for future systems, which will image very large swaths, and will be endowed with very high bandwidth, leading to enormous amounts of data. Moreover, SAR systems are usually in low Earth orbits (LEO), meaning that the downlink to each ground station at each flyover is limited to about ten minutes only (WITTING *et al.*, 2012). These systems, therefore, require a very complex and high data rate downlink.

The next constraint is the required swath width, which is tightly connected to the receive echo window timing. After a pulse is transmitted towards a given target, the delay of the echoes is already defined by the geometry of the acquisition. Then, one must ensure by adjusting the PRF that the radar is not transmitting when the echoes arrive back to the receiving antenna. Besides, reducing the PRF leads to a longer echo window, allowing, thereafter, to receive reflected signals from further ground range positions. Consequently, it is possible to increase the swath width – larger swaths are highly desirable – simply by lowering the PRF. However, by doing so, the azimuth bandwidth and resolution decrease, and the ambiguity levels increase, deteriorating the image quality. The relations between the PRF and the properties in azimuth are described next.

To comply with the conditions defined by the Nyquist theorem, and avoid aliasing effects, a PRF higher than the azimuth processed bandwidth must be used. The ratio between these two parameters is defined as the azimuth oversampling factor ($\alpha_{os,a}$) and is usually about 1.1 to 1.4 (CUMMING; WONG, 2005). By using a PRF lower than the Nyquist rate, the azimuth ambiguities drastically increase resulting in lower quality images. On the one hand, decreasing the PRF at a fixed oversampling rate reduces the azimuth bandwidth, which leads to a worse azimuth resolution. On the other hand, this lower PRF decreases the range ambiguity as the antenna receives signals from less interfering points. In summary, the PRF choice is a trade-off between swath width, azimuth resolution, and range and azimuth ambiguities.

Finally, the most strict conditions are the Nadir and the transmission interferences, both defined by the receive window timing. These conditions define some prohibitive PRF values with which it is not possible to receive without information loss. The Nadir interference occurs when the antenna receives echoes from the Nadir line (satellite ground track) at the same time it receives the target echoes. The main problem is that Nadir echoes are characterized by their very high energy, which leads to a very bright undesired

line in azimuth in the focused image. This high energy coming from the Nadir track is consequence of two main contributions. First, due to the perpendicular incidence – the signals are reflected back directly into the platform – this region right below the satellite has a high backscatter. Moreover, in this region the distance between ground and platform increases very slowly (look angle-wise) compared to the target scenes:

$$\left(\frac{\partial R}{\partial \beta}\right)_{\text{Nadir}} \ll \left(\frac{\partial R}{\partial \beta}\right)_{\text{Target}}, \quad (2.3)$$

so that echoes from a large area on ground is received in a very short period of time, leading to the high energy aspect of the Nadir echoes. This can also be understood from the resolution cell size perspective and (2.1). Once the Nadir is at an incidence angle close to 0° , the resolution cell in ground range quickly increases as the sine factor in the denominator gets closer to zero.

The transmission interference arises from the discrepancy between the very high transmit power and the low power of the echoes arriving from the target scene. Due to the slight mismatch between the feed line and the antenna, the transmit signal is reflected when it reaches the antenna. With a good match and a low return loss, the reflected power is relatively low, but already enough to saturate the receiver. Consequently, the much lower power echoes coming from the target area are completely indistinguishable when received while the antenna is transmitting. Therefore, for the current generation of monostatic systems, PRFs leading to an overlap between transmission and reception must be avoided. The Nadir and transmission restrictions are commonly summarized and identified in the so-called timing diagram.

2.2 Timing Diagram

As previously described, the timing diagram is an intuitive way to visualize the PRFs with which there are neither Nadir nor transmission interference for a given target. To better understand these interferences, it is helpful to observe the signals in the time domain. For an exemplary simplistic acquisition of a point-target, Fig. 2.2 shows the transmit signals (TX) in blue, received echoes (RX) in green and the Nadir echoes in orange. The parameters considered are a PRF of 3100 Hz, an incidence angle of 38° , a satellite/platform height of 519 km and a duty cycle of 18 %.

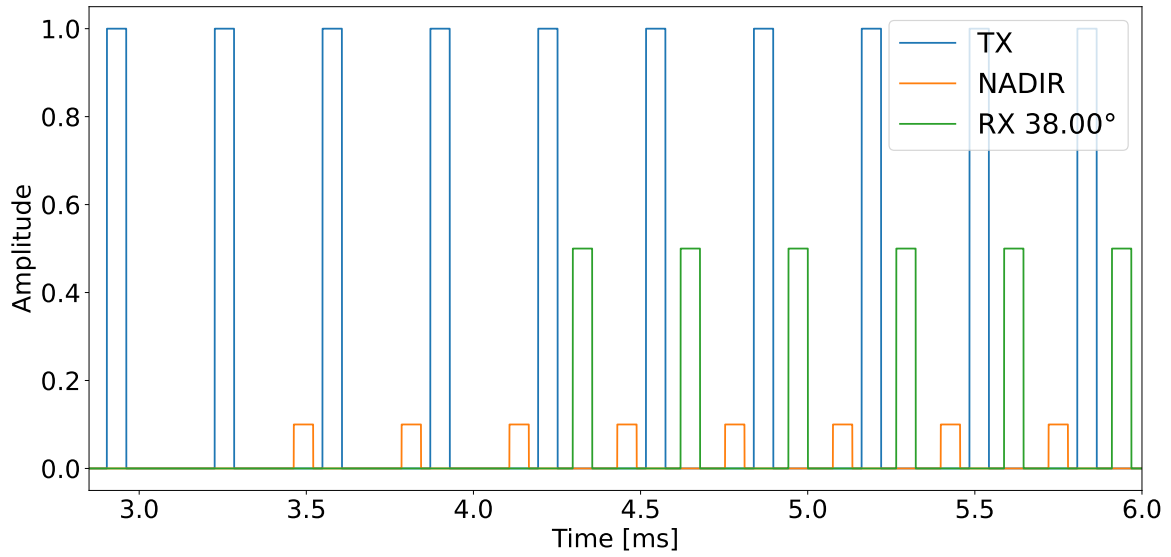


FIGURE 2.2 – Schematic plot in time of the transmit and receive signals for a PRF of 3100 Hz, an incidence angle of 38° , a platform height of 519 km and a duty cycle of 18 %.

From Fig. 2.2, it is clear that the chosen set of parameters results in a non-interfering scenario. Nevertheless, varying any of the parameters may lead to a different outcome in which there is Nadir or transmission interference. Graphically, if the Nadir echoes coincide with the received echoes, it is defined as Nadir interference. In a similar way, if the target echoes overlap with the transmit signal, it is defined as transmission interference.

The analysis above is valid for a single point-target. However, in real acquisitions the target is a wide area composed of a range of incidence angles. The analysis for these scenarios is quite similar, as these areas can be seen as a conjunction of many point-targets. Therefore, one must simply ensure that there is no interference for the whole incidence angle range being imaged.

As a method of summarizing these interferences and facilitating the analysis for extended targets, this interference checking simulation is run for a range of interest of PRFs and incidence angles. The outcome of this simulation is the timing diagram. Using the same duty cycle and satellite height as before, but varying the PRF from 2000 Hz to 6000 Hz and the incidence angle from 20° to 60° , Fig. 2.3 is obtained.

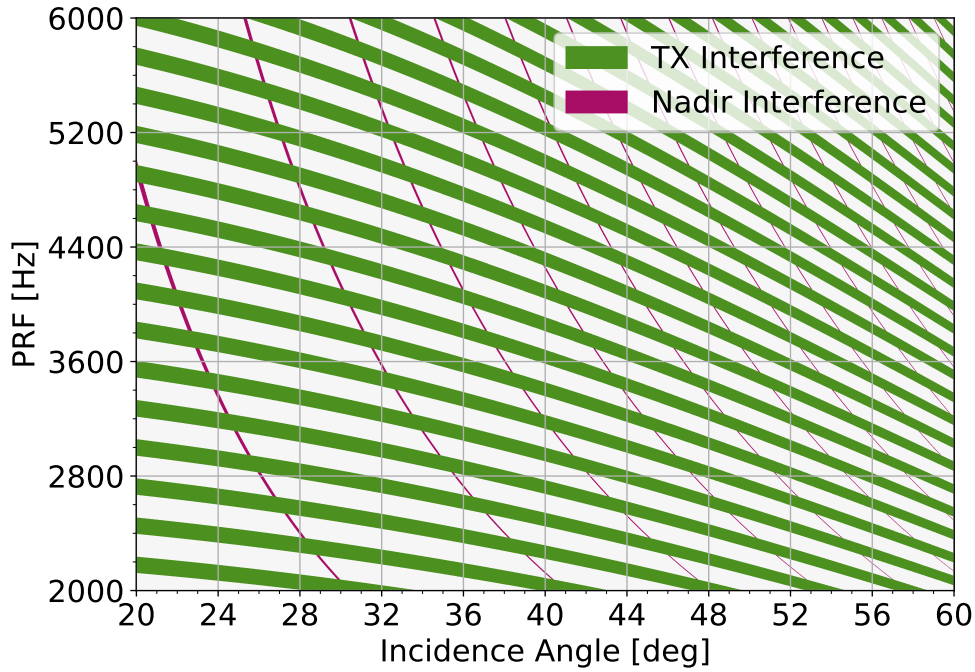


FIGURE 2.3 – Timing diagram as a function of the incidence angle for a satellite height of 519 km and duty cycle of 18 %.

In Fig. 2.3, the green stripes represent transmission interference, while the purple ones represent Nadir interference. The white regions are the good PRF and incidence angle combinations which lead to a non-interfering scenario. Due to the shape of these white regions, the timing diagram is also commonly called diamond diagram.

Concerning the Nadir interference, additional comments are required as different definitions can be used. Figure 2.2 schematically represents the received signals in the time domain. However, in the final image both the Nadir as well as any point-target are seen as only a few pixels due to the pulse compression applied, and not as extended as in the aforementioned figure. Interference, therefore, can have two interpretations: either signals being received simultaneously at the antenna, or targets overlapping in the final focused image. Both considerations have to be well understood so as to apply the proper definition in the analysis. For instance, for transmit interference, if any part of the echo overlaps with the transmit signal at the antenna, information is lost, and the PRF is considered as unsuitable.

Nadir echoes, on the other hand, typically do not saturate the receiver and may very well overlap with the target echoes at the antenna. In this case, it is important to consider the processing and check for interference in the focused domain. Moreover, consider the Nadir to be only a point target on ground is fairly optimistic. To be more precise, one can consider the focused Nadir to have a certain duration. For instance, studies have been carried out for TerraSAR-X showing that a duration of roughly $3.2 \mu s$ – or 2.5° in look

angle – models the Nadir more realistically (WOLLSTADT; MITTERMAYER, 2008). This value is not fixed for every scenario, as it strongly depends on the terrain being imaged and on how sensitive to Nadir the SAR system itself is. In this thesis, a more conservative Nadir angular size of 3° will be considered, representing a duration of $4.7 \mu s$.

In Fig. 2.3, the width of the purple stripes are given exactly by this arbitrary duration. If one considered the Nadir to be a point-like effect, the purple areas would be lines with the size of a single resolution cell. The width of the green areas, on the other hand, are given mainly by the duty cycle. Lower duty cycles means shorter transmit pulses and longer receive echo windows. Consequently, the green areas in the timing diagram become narrower, allowing for greater PRF availability.

The PRF selection through the timing diagram is then straight forward. Given the desired target area, it is enough, from a timing point of view, to select any PRF that leads to only white areas for the whole incidence angle range. However, it is also important to notice that the incidence angle range can be transformed into other domains of interest, such as ground range, fast time, look angle and slant range. The transformations depend on the height of the platform and on the curvature of Earth, and are interchangeable. Depending on the application, it might be useful to visualize the timing diagram in one of these alternative domains.

It is clear that the outcome of the timing diagram is of great importance, as it determines the possible PRFs for each target region. However, some PRFs lead to a better image quality than others. Therefore, it is also important to investigate the effect of the PRF on the ambiguities in range and azimuth.

2.3 Ambiguities

Other decisive factors in choosing the most adequate PRF are the ambiguities. Ambiguities happen when signals from areas outside the desired scene on Earth are mistakenly and, to some degree, unavoidably mixed with the target echoes. The results are images stained with undesired blurs (or ghost targets) that can occur both in range and in azimuth. The useful parameters of analysis – Range Ambiguity-to-Signal Ratio (RASR) and Azimuth Ambiguity-to-Signal Ratio (AASR) – are given by the ratios of the ambiguities power and the signal power. It is important to notice that in each direction the ambiguities have different causes and a contradicting behavior and, therefore, must be analyzed independently. Ultimately, the main objective of analyzing ambiguities is to obtain the PRF for which the ambiguities are minimized to improve the overall image quality.

2.3.1 Range Ambiguity-to-Signal Ratio (RASR)

Ambiguities in range occur when echoes from undesired areas reach the antenna at the same time as the target echoes. For a given PRF, the antenna transmits and receives every PRI in the time domain. Then, if a certain point on Earth is at an integer multiple of the PRI away from the target in fast time (τ), its echoes will reach the antenna at the same time as the next or previous echoes from the target area. This overlap between desired and undesired signals are named as range ambiguities.

It is worth noting that the PRIs typically used in spaceborne SAR missions are much shorter than the round trip delay (satellite - Earth - satellite). The radar, therefore, does not wait for the pulse to return before sending the next one, meaning that there are many pulses in the air (the so-called traveling pulses). If the radar waited for the echo to return, there would be no range ambiguity.

Figure 2.4 depicts schematically a range ambiguity scenario. The platform is represented by the hexagon and is flying into the page. The targets are represented by the green (desired target) and red (undesired target) symbols and are separated in ground range on Earth's surface. The satellite in this situation is imaging the green target, which has a slant range of R_1 and an echo delay of $\tau_1 = 2R_1/c_0$. The undesired red target, which is at a distance of R_2 from the satellite, is one PRI away in the time domain ($\tau_1 = \tau_2 + \text{PRI}$). In other words, the echoes from the red target arrive one PRI sooner than those from the green target. This leads to an overlapping between the echoes, as shown on the right-hand side of the figure. Using traditional chirp signals, the range ambiguities cannot be separated from the target echoes, leading therefore to interference and, in the end, to degradation in the focused image quality.

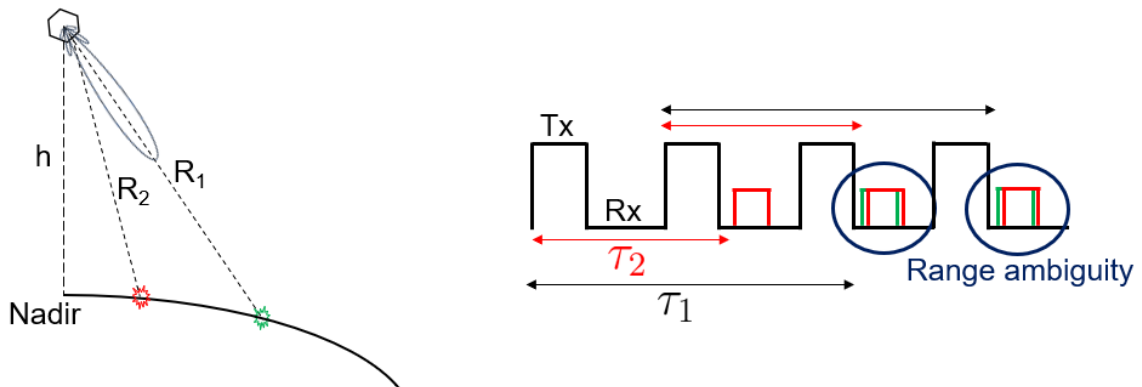


FIGURE 2.4 – Visualization of a scenario with range ambiguities.

It is important to notice that changing the PRF influences the ambiguity position. For instance, a lower PRF (larger PRI) pushes the ambiguity further away from the

target. Combining this different position with the transmit and receive antenna pattern, a different RASR is obtained. Therefore, the PRF can be adjusted so as to achieve a better performance.

To calculate the RASR value it is necessary to know not only which points on Earth cause the ambiguities, but also the target region and a model of the reflectivity of Earth. Therefore, to predict RASR performance by means of simulation, it is also mandatory to know the antenna pattern, the satellite positioning, and to select a target.

First, a backscatter model (σ_0) for the terrain must be considered to get more accurate RASR predictions. This model can be defined based on the incidence angle, and provides information about the reflectivity of the scene. Generally, the further away from the Nadir track, the weaker the scene reflects back to the satellite antenna. In this thesis the soil and rocks Ulaby model for X-Band and HH polarization is considered (ULABY; DOBSON, 1988).

Second, the position of the ambiguities are given by those areas that are multiple PRIs away from the target. These ranges are then calculated by

$$R_{ambiguities} = R_{target} + m \cdot \frac{c_0 \cdot \text{PRI}}{2} \quad \forall m \in \mathbb{Z}. \quad (2.4)$$

Important to observe in (2.4) that m has upper and lower limits, so that the number ambiguity points is limited. These restrictions are given by Earth's limits itself. The lower limit is given by the platform height, as, naturally, an ambiguity with a calculated range lower than the platform height does not exist. Similarly, the upper limit is given by the maximum line-of-sight distance between the platform and Earth's surface. Moreover, the case in which $m = 0$ represents the symmetrical target position in the negative look angles region.

Third, the platform positioning (position, velocity, and attitude) and the antenna pattern are strongly dependent on the system that is being analyzed. In this thesis, the sun-synchronous orbit of TerraSAR-X is considered, and the antenna pattern is derived from a phased-array antenna with rectangular shape.

Finally, the RASR is calculated simply by dividing the total power coming from the ambiguities by the power coming from the target. Considering the two-way antenna gain (G), the backscatter model (σ_0) and the ranges (R), the RASR is calculated by

$$\text{RASR} = \frac{\sum_{k=1}^N P_{amb,k}}{P_{target}} = \frac{\sum_{k=1}^N \frac{G_{two-way,k} \cdot \sigma_{0,k}}{\sin \theta_{i,k} \cdot R_k^3}}{\frac{G_{two-way,0} \cdot \sigma_{0,0}}{\sin \theta_{i,0} \cdot R_0^3}}, \quad (2.5)$$

in which k and 0 represent the k -th ambiguity and the target, respectively (CURLANDER; MCDONOUGH, 1991).

The visualization of the ambiguities with respect to the target position and their respective gains is useful to better understand the effect of the PRF on the RASR. Figures 2.5 and 2.6 depict the range ambiguities look angles and powers in an exemplary acquisition of a target at an incidence angle of 39° for two different PRFs. The y-axis adjusted gain represents the antenna two-way gain multiplied by the backscatter, the slant range, and the incidence angle factors, as in (2.5). It is clear that with the increase of the PRF the ambiguities get closer to the target itself, leading to higher gains and worse RASR.

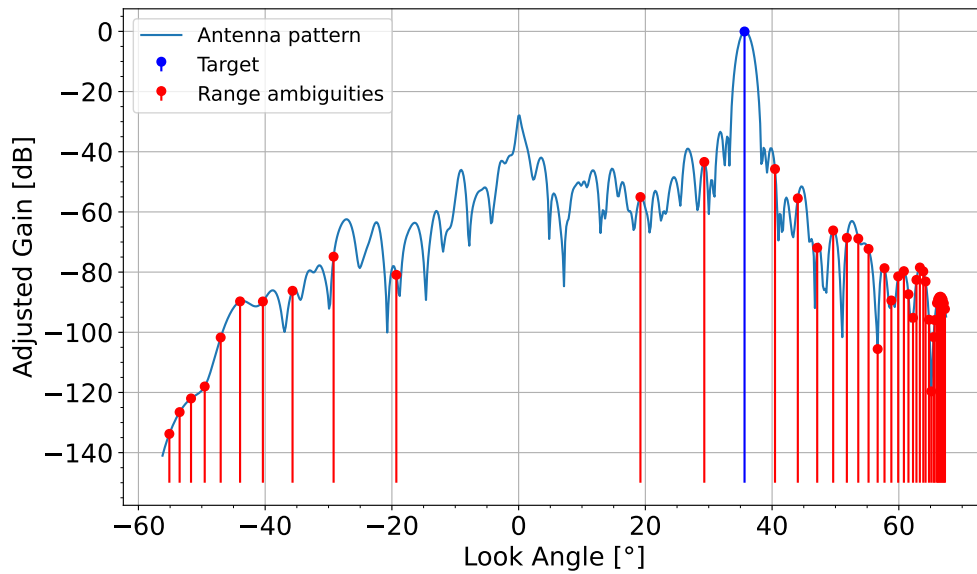


FIGURE 2.5 – Visualization of the target position and the range ambiguities on the normalized adjusted antenna pattern in elevation for an exemplary acquisition of a target at an incidence angle of 39° with a PRF of 3000 Hz.

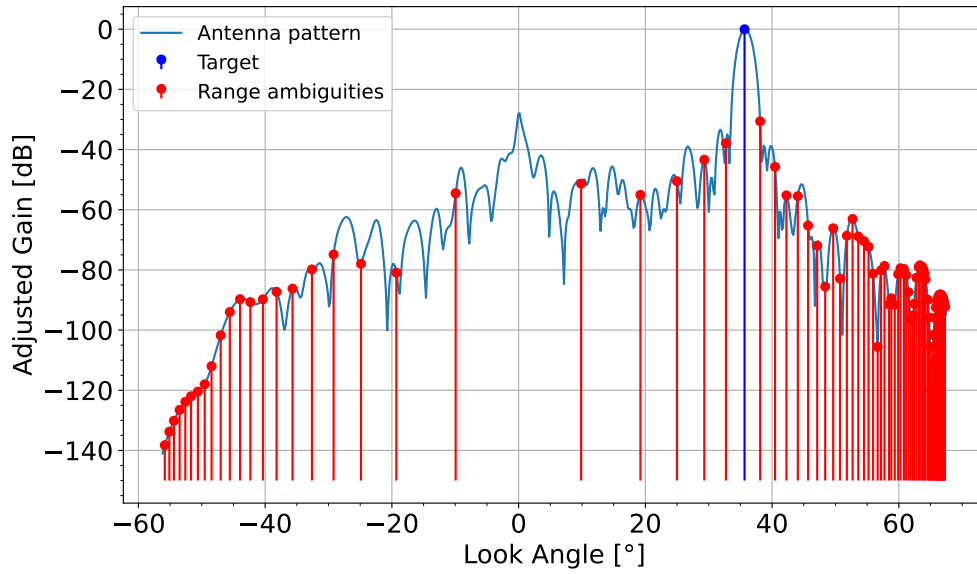


FIGURE 2.6 – Visualization of the target position and the range ambiguities on the normalized adjusted antenna pattern in elevation for an exemplary acquisition of a target at an incidence angle of 39° with a PRF of 6000 Hz.

The plots makes it clear that range ambiguities become a concern either when they are sufficiently close to the main lobe or near the Nadir, because the power of the signal received from these directions is strong. It can be seen, for instance in Fig. 2.6, that the first far-range ambiguity is already on the main lobe. On the one hand, PRFs leading to ambiguities falling near or over the Nadir are eliminated in the timing analysis. On the other hand, PRFs leading to ambiguities on the main lobe, must then be eliminated by the range ambiguity analysis.

The figures aforementioned are only depicting the scenario where the target is at the peak of the main lobe, i.e., in the scene center. Stripmap images, however, usually have a swath width of more than 30 km. Therefore, it is also important to check RASR performance for the whole scene, and not only the scene center. This worst case analysis may become critical, not only because targets at near and far range are imaged by a lower antenna gain, but also because the first ambiguities (those closest to the target) starts to climb the main lobe for high PRFs, achieving quickly a very high power. This situation is depicted for a target 12 km apart from the scene center in Fig. 2.7.

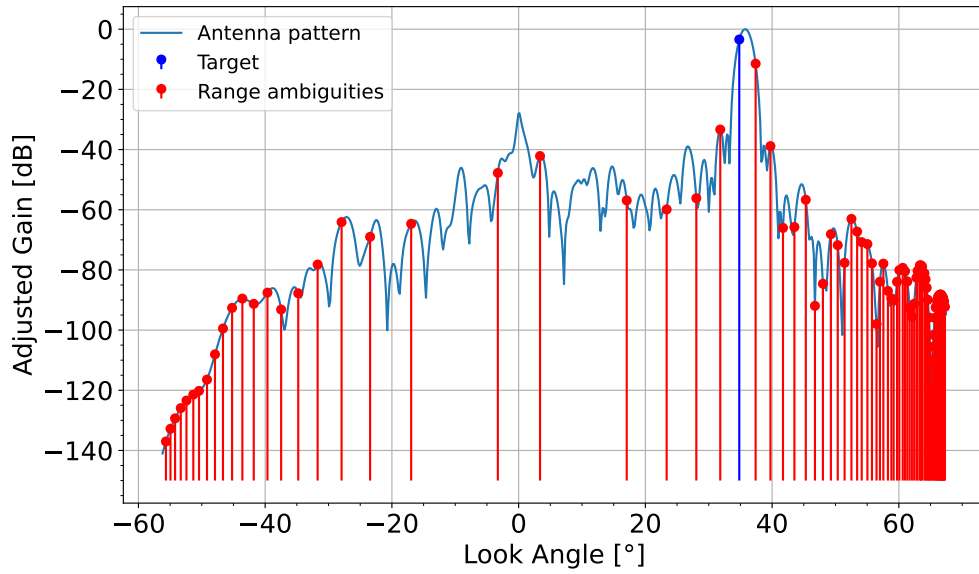


FIGURE 2.7 – Visualization of the target position and the range ambiguities on the normalized adjusted antenna pattern in elevation for an exemplary acquisition of a target at an incidence angle of 39° with a PRF of 6000 Hz. The target is 12 km away from the scene center towards near range.

This RASR analysis can be summarized in one plot of the RASR performance by the PRF, for multiple targets within the scene, as shown in Fig. 2.8. The figure depicts a RASR simulation for an acquisition considering the TerraSAR-X system. The real antenna pattern, and satellite position, velocity and attitude were considered. In this situation it becomes clear that if a very high PRF is desirable, one must take special care not to degrade the image quality beyond acceptable levels.

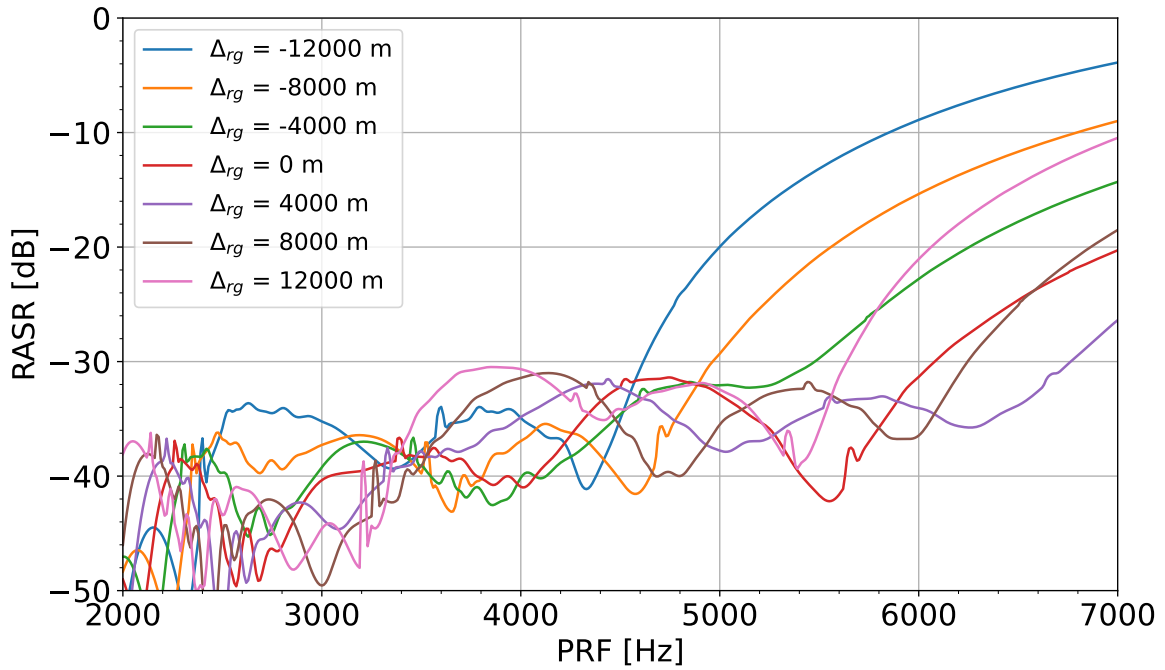


FIGURE 2.8 – Simulated RASR for the TerraSAR-X Stripmap mode at different range target positions with an incidence angle of 39° . The distance of the simulated target with respect to the scene center (Δ_{rg}) is provided in the legend.

Range ambiguities are of special concern in the concurrent imaging mode as a very high PRF has to be used to achieve enough sampling rate (azimuth bandwidth) in each mode. As a consequence of using low PRIs, the ambiguous targets get closer to the scene center and, therefore, are received by the antenna with a higher power due to the sinc-like antenna pattern.

Interestingly enough, in concurrent imaging acquisitions, the very first ambiguity of each mode – which is the one with highest power – does not come from the same mode itself, but from the other alternating one. For example, assuming a concurrent acquisition using up and down chirps, the strongest and most apparent range ambiguities are not focused (KRAUS *et al.*, 2022). It is worth noting that, even though the ambiguities are not properly focused, their energy is still present and the image is also degraded. Once the main source of range ambiguities is not the same mode, one can think of time, space, and frequency diversity techniques to differentiate the signals from each mode so as to reduce ambiguities.

On the scenario above, in which up and down chirps are considered, Fig. 2.9 shows a real acquisition with very strong range ambiguities. The image originates from a concurrent acquisition with the antenna pattern purposely misaligned to increase the range ambiguities, and make them more visible. It becomes clear that range ambiguities can become a significant problem for the interpretation of SAR images, especially near water

to land transitions.

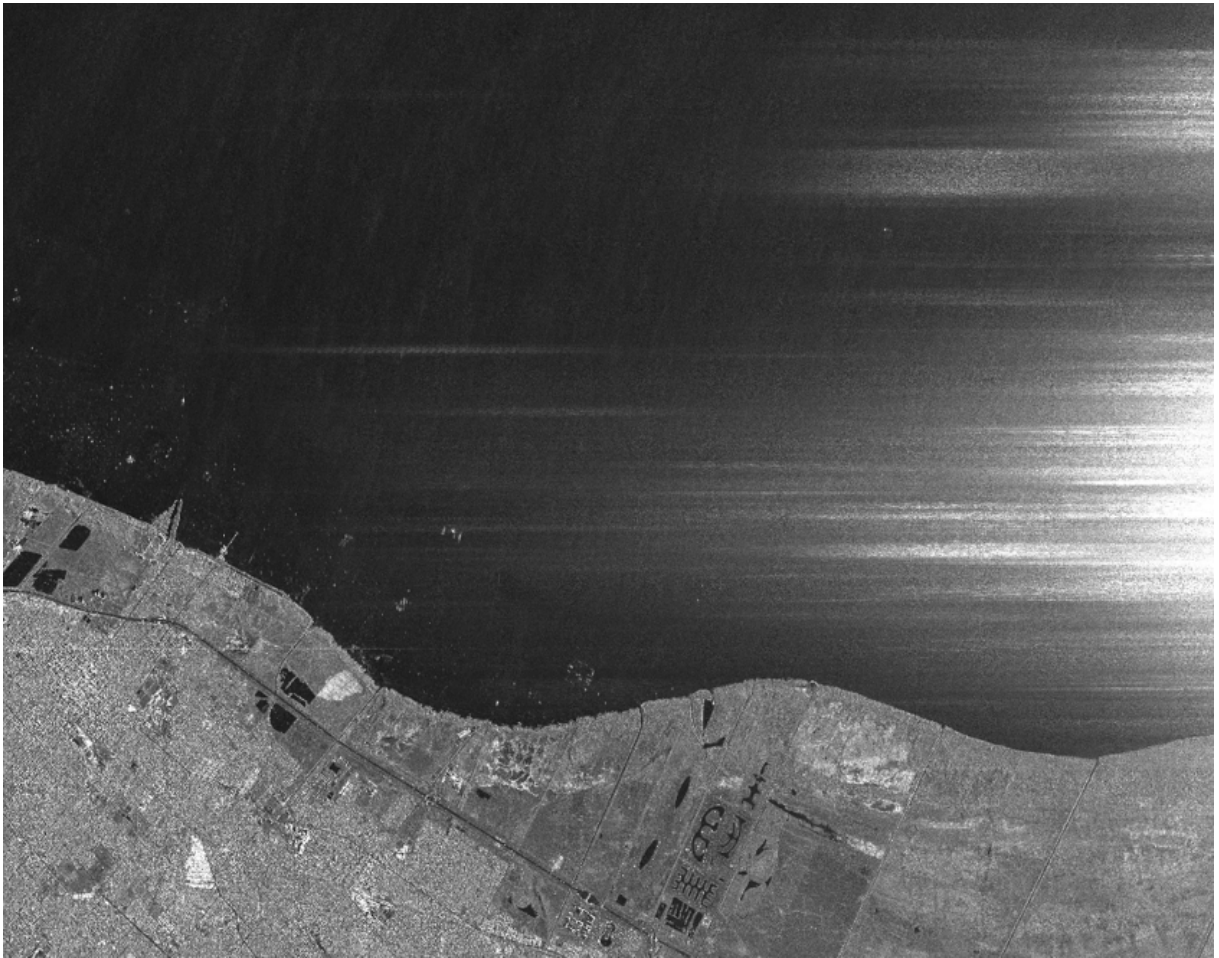


FIGURE 2.9 – Visualization of strong range ambiguities on the River Plate near the city of Buenos Aires, Argentina. The ambiguities do not appear focused due to the alternation of up and down chirps on transmit.

In this subsection it was shown that range ambiguities play a significant role in determining the PRF. More specifically, it became clear that increasing the PRF, the RASR performance is directly negatively affected. In azimuth, however, increasing the PRF is actually beneficial, while a low PRF leads to degradation in the image quality. Consequently, a careful investigation must be conducted to further complement the ambiguities analysis.

2.3.2 Azimuth Ambiguity-to-Signal Ratio (AASR)

The ambiguities in azimuth are caused by an effect similar to those in range. However, instead of signals being mixed because they arrive at the receiver at the same time, they are mixed for arriving with an equivalent Doppler frequency shift. Due to the finite sampling frequency in azimuth (PRF), the not band-limited receive signals (echoes) lead to aliasing

effects, i.e., ghost targets appear on the final focused image. To better understand this effect, it is important to first discuss how signals behave in the azimuth direction.

For a given point on Earth, it is intuitive that the platform first gets closer then goes away during an acquisition. In the slant range plane, as represented schematically in Fig. 2.10 where R_s and R_e represent the slant range of start and end of the illumination time of the target, the variation of distance in time can be written as

$$R(t) = \sqrt{R_0^2 + v_s^2(t - t_0)^2}. \quad (2.6)$$

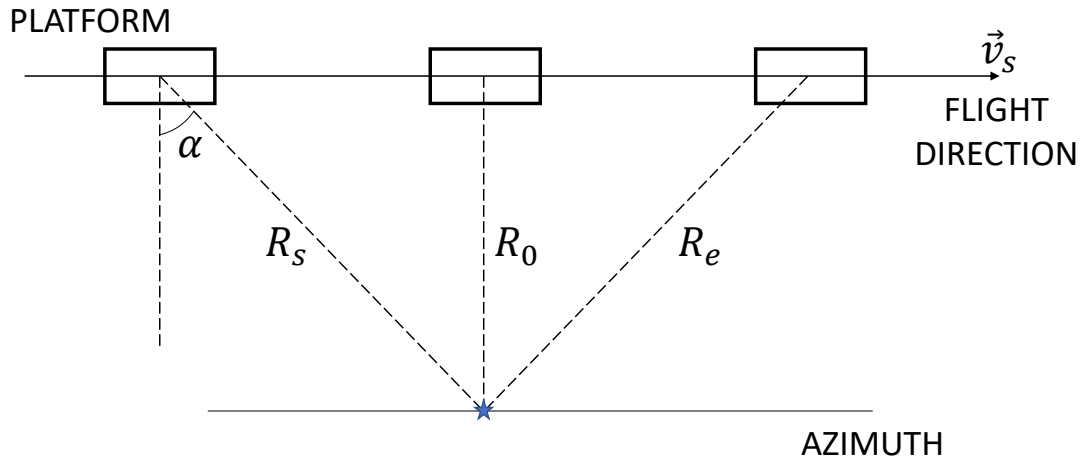


FIGURE 2.10 – Acquisition geometry in the slant range plane.

Therefore, from the Doppler effect, the signal frequency is shifted based on the relative velocity between the antenna and the target. The Doppler frequency shift f_d can be written as

$$2\pi f_d = \frac{\partial}{\partial t} \left(-\frac{4\pi}{\lambda} R(t) \right), \quad (2.7)$$

which results in

$$f_d = -\frac{2}{\lambda} \frac{v_s^2 t}{\sqrt{R_0^2 + v_s^2 t^2}} \approx -\frac{2}{\lambda} \frac{v_s^2 t}{R_0}, \quad (2.8)$$

given v_s the satellite speed, λ the signal wavelength, R_0 the minimum distance between the satellite and the target and t the slow time.

From a signal processing point of view, it is important to pay attention to whether these received frequencies will be respected by the sampling rate. In the azimuth direction, the sampling rate is given exactly by the PRF. Typically, the PRF does not go much higher than 7 kHz, while the Doppler shift may vary from -70 kHz to +70 kHz. It is

important to observe that the echoes are not strictly band limited, but the power of high Doppler frequencies is attenuated by the azimuth antenna pattern. Thus, it is clear that the azimuth sampling rate is not high enough to differentiate every incoming Doppler frequency.

Once a low sampling rate that does not respect the minimum requirement of the Nyquist theorem is used, it can be concluded that every f_d above $\frac{\text{PRF}}{2}$ and below $-\frac{\text{PRF}}{2}$ are treated as frequencies between these two values in the receiver. This effect of folding back high frequencies is the cause of azimuth ambiguities.

The AASR for Stripmap acquisitions is then estimated by (CURLANDER; MC-DONOUGH, 1991; MITTERMAYER *et al.*, 2014)

$$\text{AASR} \approx \frac{\sum_{\substack{m=-\infty \\ m \neq 0}}^{\infty} \int_{-\Delta f_d/2}^{\Delta f_d/2} G^2(f + m \cdot \text{PRF}) \cdot W^2(f, \Delta f_d) df}{\int_{-\Delta f_d/2}^{\Delta f_d/2} G^2(f) \cdot W^2(f, \Delta f_d) df}, \quad (2.9)$$

where G is the antenna one-way gain in azimuth, and W is the Hamming window with $\alpha = 0.6$ given by (HARRIS, 1978)

$$W(f, \Delta f_d) = \alpha + (1 - \alpha) \cdot \cos\left(\frac{2\pi f}{\Delta f_d}\right), \quad -\frac{\Delta f_d}{2} \leq f \leq \frac{\Delta f_d}{2}. \quad (2.10)$$

In (2.9), Δf_d is the processed azimuth (or Doppler) bandwidth, and is related to the PRF by the azimuth oversampling factor $\alpha_{os,a}$ as

$$\alpha_{os,a} = \frac{\text{PRF}}{\Delta f_d} \geq 1. \quad (2.11)$$

As this factor gets closer to the unity, the higher becomes the azimuth processed bandwidth, resulting in better azimuth resolution. As a trade-off, it increases the AASR. The opposite effect happens if this factor is increased. A common approach to find the oversampling factor is defining a maximum allowed AASR and consequently determining the minimum factor that satisfies it. This method maximizes the azimuth resolution without sacrificing the AASR beyond the requirements.

To better understand how the AASR is obtained, the antenna gain in azimuth and the received Doppler frequency can be visualized in conjunction. In Figs. 2.11 and 2.12, the blue areas represent the two-way antenna gain of the target bandwidth, while the red ones represent the gain of the ambiguous areas. The AASR is calculated as the ratio of the sum of the red areas to the blue one, as stated in (2.9). In these simulations, an antenna size of 4.8 m, zero squint angle, a satellite speed of approximately 7600 m/s and

a signal carrier frequency of 9.65 GHz are being considered.

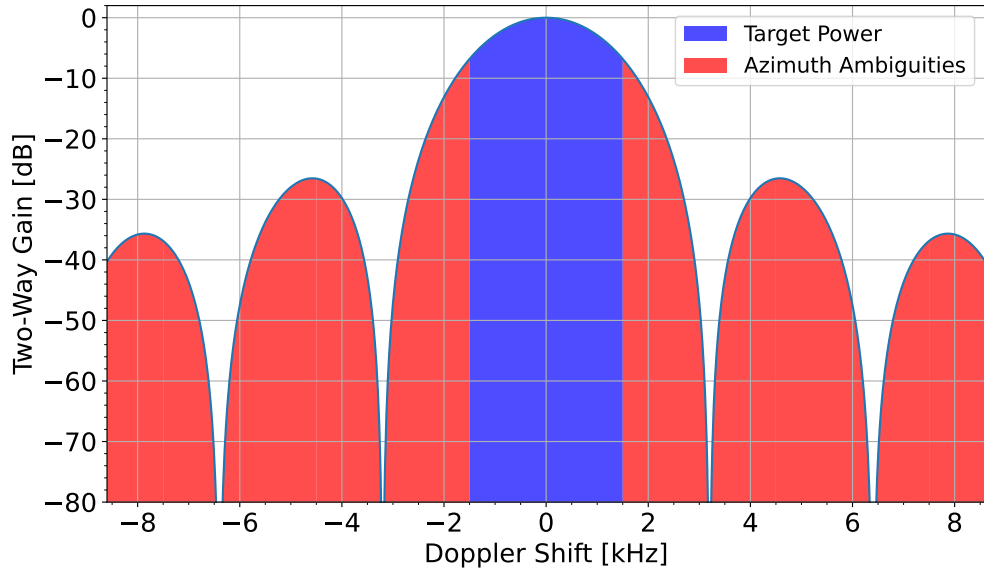


FIGURE 2.11 – Visualization of the target Doppler bandwidth and the azimuth ambiguities on the azimuth antenna pattern considering a PRF of 3000 Hz and an oversampling factor $\alpha_{os,a}$ of 1.0.

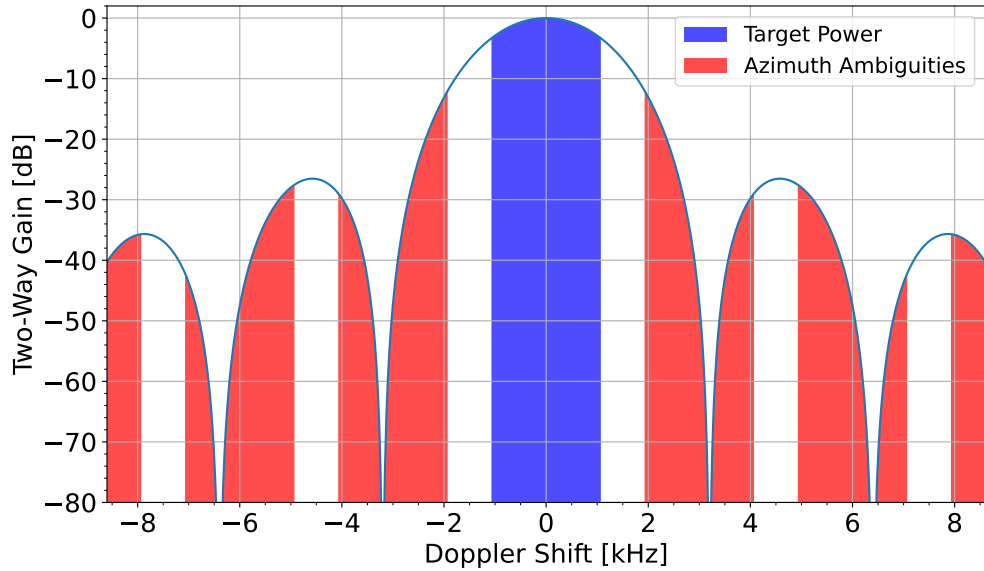


FIGURE 2.12 – Visualization of the target Doppler bandwidth and the azimuth ambiguities on the azimuth antenna pattern considering a PRF of 3000 Hz and an oversampling factor $\alpha_{os,a}$ of 1.4.

The AASR analysis can be summarized in one simple plot of the AASR performance by the PRF, for multiple oversampling factors, as shown in Fig. 2.13. In this situation it

becomes clear that if a wide swath (low PRF) is desirable, one must take special care not to degrade the image quality beyond acceptable levels.

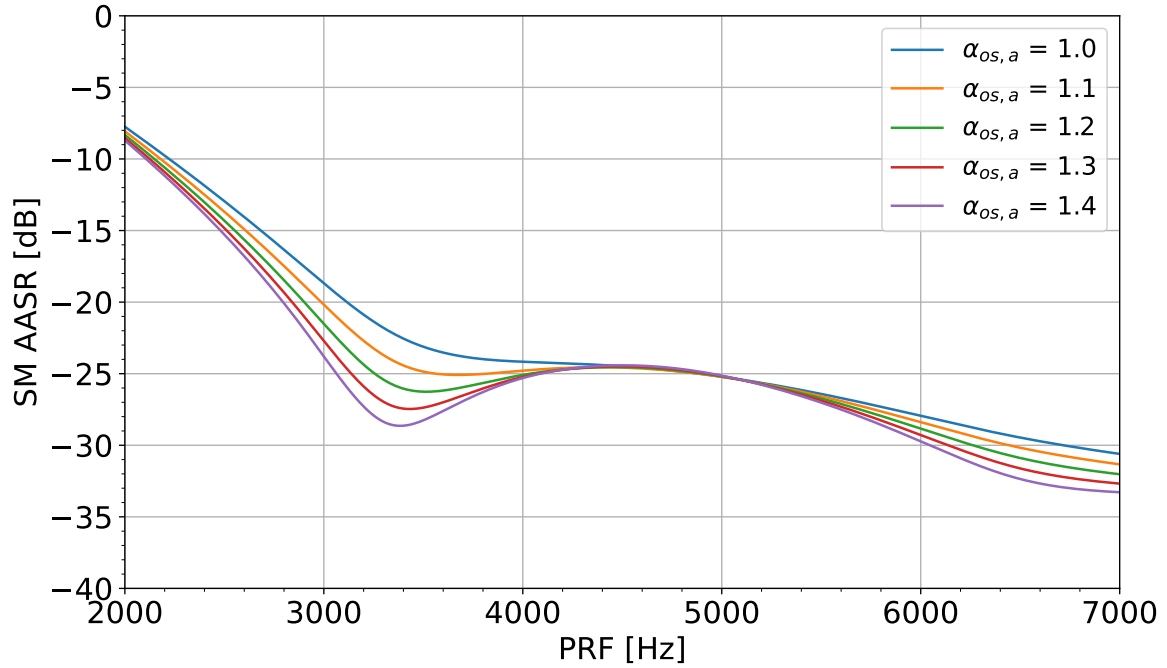


FIGURE 2.13 – AASR behavior for different azimuth oversampling factors and an antenna size of 4.8 m.

As expected, lower PRFs result in higher AASR due to those frequencies obtained by high antenna gains being folded back as ambiguities. Besides, it is also clear that lower oversampling factors also result in worse AASR, due to more high power frequencies being considered as ambiguous.

As a matter of visualization of the ambiguities on real SAR acquisitions, Fig. 2.14 depict a concurrent acquisition of the city of Piúma in Brazil. This is a region of calm water to city transition, facilitating the visualization of the ambiguities. The trade-off between AASR and azimuth resolution is clear, as by reducing the Doppler processed bandwidth from 3044 Hz to 2174 Hz, the azimuth ambiguities gradually vanish. It becomes clear that better AASR values lead to images with improved visualization.

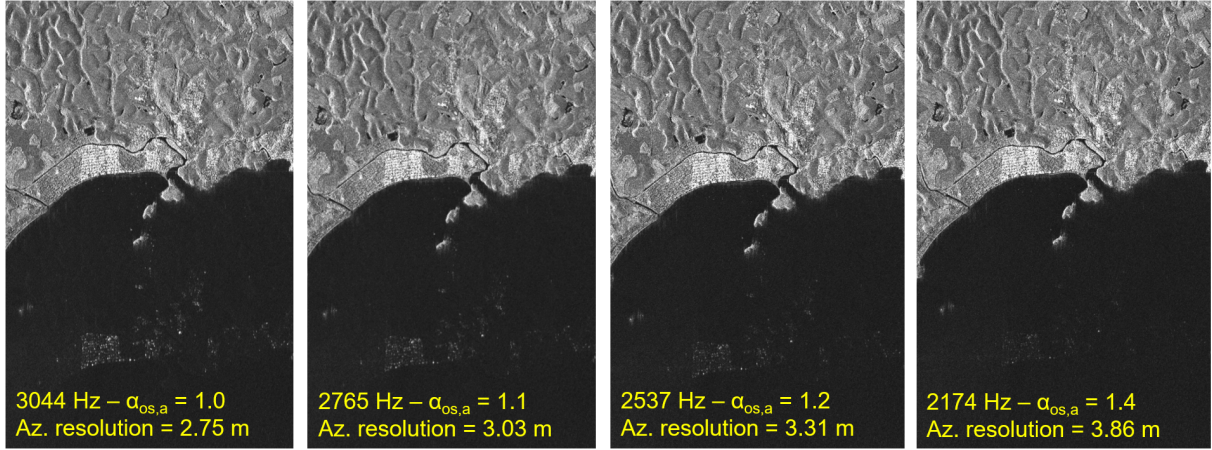


FIGURE 2.14 – Visualization of azimuth ambiguities on the Atlantic Ocean near the city of Piúma, Brazil. From left to right, the trade-off between azimuth resolution and AASR is depicted. The lower the Doppler processed bandwidth is, the better and less visible are the azimuth ambiguities.

In the concurrent imaging context, because two images are being generated simultaneously by interleaving the modes, the effective PRF is only half of the total PRF used in the acquisition. Therefore, the AASR analysis must consider the effective PRF as it is the one representing the sampling of each image. For instance, if a PRF of 4000 Hz is used in the acquisition, then each mode has an effective sampling of only 2000 Hz, leading to degraded azimuth ambiguity performance. This sharing of sampling between the modes increases the AASR from about -24 dB (good) up to -8 dB (degraded).

Once the ambiguities both in range and azimuth are obtained, the next step is obtaining the PRF leading to a good trade-off between the ambiguities. One possibility is by defining the Ambiguity-to-Signal Ratio (ASR) as

$$\text{ASR} = \text{RASR} + \text{AASR}. \quad (2.12)$$

Equation (2.12) results in a curve representing the total amount of ambiguities in the scene. From this curve, the point of minimum is of interest as it can be understood as the point of best image performance in terms of ambiguities. Then, given a maximum ASR allowed, it is possible to obtain a PRF range with which the final image can be generated with an acceptable level of ambiguities.

This analysis can be made for every intended acquisition so as to avoid getting images strongly blurred by ambiguities. Even though this metric may be of great value, a more careful analysis is usually required. For instance, the point of minimum ASR may lead to unacceptable performance in either range or azimuth. So, defining a minimum acceptable level for each one of them is also needed. Furthermore, the scene size and azimuth resolution must also be considered in the analysis, as a higher PRF reduces the scene

size but improves the azimuth resolution. In summary, when designing an acquisition many parameters must be simultaneously considered and refined according to the specific application.

This chapter showed some of the crucial steps required to select the PRF for a traditional SAR acquisition. This conventional imaging is, however, quite limited as many trade-offs take place related to the final image quality. For instance, achieving wide swaths in conjunction with high resolution both in range and in azimuth is contradicting, and not achievable with traditional techniques. The following chapter has as objective doing a literature review of some techniques proposed in the scientific community aiming at getting rid of these image quality trade-offs. It will be shown that these techniques in the end only relocate the trade-offs to a different dimension, such as by increasing costs, system complexity, data rate, etc.

3 High-Resolution Wide-Swath Imaging

The current generation of SAR systems is capable of achieving very high resolution through Spotlight modes (CARRARA; GOODMAN; MAJEWSKI, 1995; MITTERMAYER *et al.*, 2014) and also very wide-swaths with the ScanSAR mode (CUMMING; WONG, 2005). Aiming at high resolutions typically leads to narrow scenes, whilst wide scenes come with coarse resolutions. So as to achieve a frequent observation of the whole Earth with excellent resolution, many new techniques are currently being proposed in the scientific community. The current generation of deployed spaceborne systems, for instance the duo Sentinel-1A and 1B, is capable of interferometrically imaging the whole globe with a resolution of 5 m in range by 20 m in azimuth every 6 days (ESA COMMUNICATION DEPARTMENT, 2014).

The applications of performing high-resolution wide-swaths (HRWS) imaging with SAR are vast. As an example, the continuous observation of dynamic processes on Earth's surface, monitoring the environment and the climate in terms of biosphere (biomass and forest structure), geosphere (Earth surface deformation), cryosphere (ice melting processes) and hydrosphere (soil moisture) would be vital to the understanding of the climate change, carbon cycle, sea level rise, earthquake risk and forecast, etc (MOREIRA *et al.*, 2015). Other possibilities, such as urban traffic monitoring, surveillance of areas of interest, agricultural monitoring and wildfire detection, are also made possible by the extensive use of SAR (MOREIRA *et al.*, 2013).

The objective of this chapter is to describe and discuss some of the most recently developed techniques that allow, to some extent, large-scale SAR imaging. It will be shown that the well-known MIMO systems in communications are gradually being integrated into SAR through several distinctive methods. More specifically, those techniques which can be nicely integrated into the concurrent mode are the ones of most interest.

3.1 SAR Trade-offs

The design of a SAR acquisition is intrinsically dependent on the requirements of a specific application. Usually many performance parameters are defined as prerequisites of the final image, such as noise equivalent sigma zero (NESZ), range and azimuth resolution, ambiguities and scene sizes. So as to achieve these requirements, several system parameters must be carefully chosen during the system design, such as the peak power, the antenna size, the amount of transmit and receive channels, and the PRF (YOUNIS; LOPEZ-DEKKER; KRIEGER, 2014). Current state-of-the-art SAR systems, e.g. TerraSAR-X and TanDEM-X, were built flexible enough such that many different acquisition modes can be performed even with a fixed set of system parameters.

Typical acquisition modes inherently depict the trade-off between these multiple parameters. The most standard SAR mode, Stripmap, is capable of acquiring medium resolution images of a fixed swath width for an unlimited azimuth length (CUMMING; WONG, 2005). To achieve a higher azimuth resolution, a common technique is to steer the antenna beam in azimuth towards a fixed area during the imaging. This technique is known as Spotlight mode (CARRARA; GOODMAN; MAJEWSKI, 1995; MITTERMAYER *et al.*, 2014; KRAUS *et al.*, 2016). The drawback of this mode arises from the steering, meaning that only a small spot on the ground is imaged, losing therefore scene extent in azimuth.

Conversely, the ScanSAR mode is a technique capable of imaging a much larger swath, but at the expense of azimuth resolution (CUMMING; WONG, 2005). This is achieved by sharing the illumination time between multiple sub-swaths. One issue that arises from ScanSAR is the scalloping effect. It consists of a periodical amplitude modulation caused by the lower gain parts of the main lobe of the azimuth antenna pattern. So as to get rid of the scalloping effect, and improve the ambiguity ratios, the terrain observation by progressive scans (TOPSAR) technique was proposed (ZAN; GUARNIERI, 2006; META *et al.*, 2010).

These trade-offs between resolution and coverage of the multiple imaging modes are summarized in Fig. 3.1.

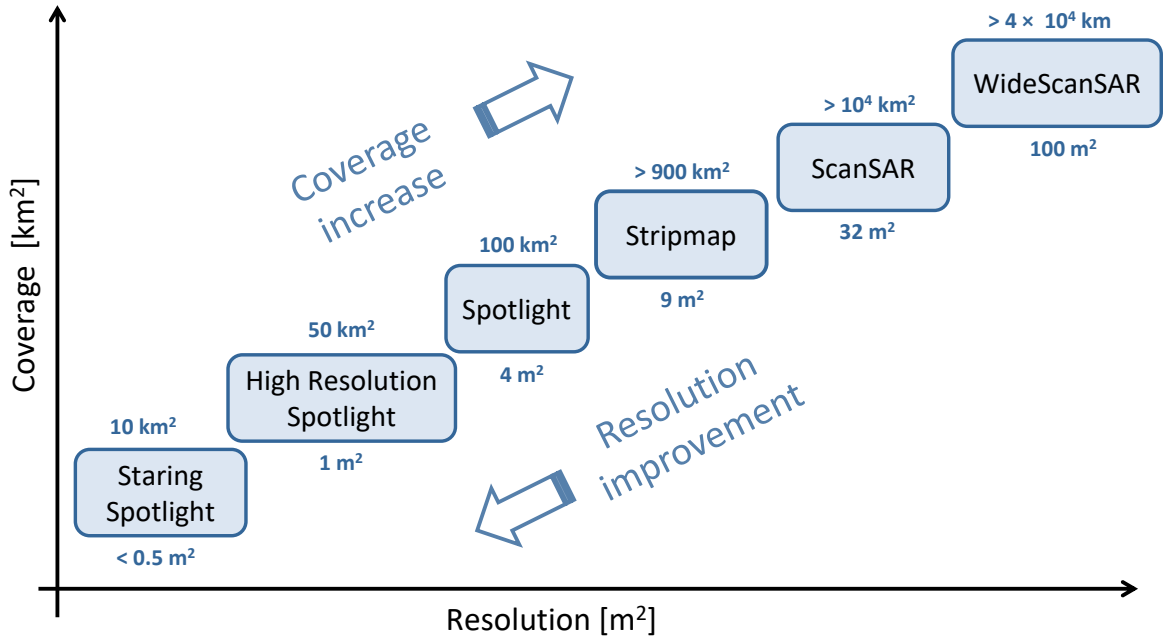


FIGURE 3.1 – Summary of the trade-off between resolution and coverage of the current most typical SAR imaging modes.

Combinations of these modes to simultaneously acquire more than one image in one fly-over are also possible (CALABRESE *et al.*, 2015; KRAUS *et al.*, 2022; RIBEIRO *et al.*, 2022). In these proposals, for instance, the interleaving of the modes from pulse to pulse allows the imaging of different targets with both the Stripmap and the Staring Spotlight modes simultaneously. The trade-offs in these sort of acquisitions are mainly degraded ambiguity ratios and Stripmap swath width, caused by the use of higher PRFs.

The aforementioned single-channel monostatic modes are limited in performance by physical factors. For instance, to achieve a high azimuth resolution, a high PRF is required, leading therefore to a narrow swath and range ambiguities concerns. From an antenna size point of view, given that the achievable azimuth resolution is half the antenna length (CURLANDER; MCDONOUGH, 1991), an ever shorter antenna would be required to improve the azimuth resolution, leading to degradation in the noise performance of the SAR system due to the lower antenna gain. Similarly, in elevation a shorter antenna would be required to image a wider swath, conflicting with a high bandwidth and range resolution system, which requires a higher gain to maintain acceptable signal-to-noise levels. It is important to recall that the gain of a phased-array antenna is proportional to its area – so that smaller antennas have lower gains – and is equal to

$$G_0 = \frac{4\pi\epsilon_{ap}}{\lambda^2} A_p, \quad (3.1)$$

where G_0 represents the maximum gain of the antenna, λ the wavelength, ϵ_{ap} the aperture

efficiency and A_p the antenna physical size. For constant distribution apertures, the physical and the maximum effective areas are equal ($\epsilon_{ap} = 1$) (BALANIS, 2016).

The trade-offs described are inherent of single-channel monostatic SAR systems. For each of the imaging modes, one can always tailor the multitude of adjustable parameters to obtain a better performance for specific applications, but always limited to strong intrinsic restrictions as previously described. Therefore, future generation systems desiring to achieve good HRWS performance are required to employ more advanced techniques to overcome these limitations. Most of the proposed methods lean towards MIMO systems, employing multiple channels to improve the imaging performance. New innovative techniques such as antenna sweeping, multiple phase centers, staggered SAR, space-time coding and novel waveforms are being constantly proposed and shown to bring significant improvements towards high-resolution wide-swath systems.

3.2 State-of-the-Art Systems and HRWS Imaging Requirements

At the current stage of development, many approaches for HRWS systems have already been proposed in the literature. However, these novel techniques still have not been fully deployed to real operational systems. Therefore, it is of great value to analyze the scenario of state-of-the-art SAR systems to derive and understand the requirements for the future generation systems.

There are currently many operational satellites from private and public companies operating at different frequency bands. In the X-band, for instance, the German satellites TerraSAR-X and TanDEM-X launched in 2007 and 2010, the Spanish PAZ launched in 2018 and the Italian Cosmo-SkyMed Second Generation (CSG) launched in 2019 are the current references in terms of SAR imaging. Among the many performance parameters that can be used to assess their imaging quality, scene extent, resolution, ambiguity-to-signal ratios and noise equivalent sigma zero (NESZ) were chosen in this work to encapsulate the analysis. Tables 3.1, 3.2, and 3.3 summarize these parameters for each of the three X-band state-of-the-art systems for each of the main imaging modes (AGENZIA SPAZIALE ITALIANA, ASI, 2021; EINEDER *et al.*, 2013; HISDESAT, 2021).

TABLE 3.1 – Stripmap performance for X-Band state-of-the-art spaceborne systems.

	CSG	PAZ	TerraSAR-X
Swath Width	40 km	30 km	30 km
Range Resolution	3.0 m	1.1 m	1.2 m
Azimuth Resolution	3.0 m	3.0 m	3.3 m
Ambiguity Ratios	-20 dB	-17 dB	-17 dB
NESZ	-22 dB	-16.8 dB	-19 dB

TABLE 3.2 – ScanSAR performance for X-Band state-of-the-art spaceborne systems.

	CSG	PAZ	TerraSAR-X
Swath Width	100 km	100 km	100 km
Range Resolution	4.0 m	1.2 m	1.2 m
Azimuth Resolution	20.0 m	18.5 m	18.5 m
Ambiguity Ratios	-20 dB	-15 dB	-15 dB
NESZ	-22 dB	-18 dB	-19 dB

TABLE 3.3 – Staring Spotlight performance for X-Band state-of-the-art spaceborne systems.

	CSG	PAZ	TerraSAR-X
Swath Width	7.3 km	4.6 - 9 km	4.6 - 7.5 km
Azimuth Extent	3.2 km	2.7 - 3.6 km	2.5 - 2.8 km
Range Resolution	0.5 m	0.6 m	0.6 m
Azimuth Resolution	0.3 m	0.22 m	0.24 m
Ambiguity Ratios	-20 dB	-16 dB	-17 dB
NESZ	-22.5 dB	-16.2 dB	-18 dB

The performance of the satellites aforementioned can be taken as a baseline for what one would expect from a next generation HRWS SAR system. Being the objective imaging wider scenes and with higher resolution, it is clear what parameters must be improved. For instance, achieving one meter resolution in range and azimuth together with a swath

width of at least 50 km in Stripmap imaging is currently not possible. This kind of performance, however, will very likely be achieved in the near future by making use of proper techniques (BARTUSCH *et al.*, 2021b), such as the ones that will be explained in the next sections.

Another example is for Staring Spotlight acquisitions, which are strongly restricted in azimuth extent by the beam width of the antenna. In this case, a scene size of $10\text{ km} \times 10\text{ km}$ with a 25 cm resolution would also be a great improvement and can be expected in the new systems (BARTUSCH *et al.*, 2021b). An important consideration is that these improvements can be achieved without compromising neither the ambiguities nor the noise performance.

Naturally predicting the performance of still non-existing systems can end up not being very accurate as new possibilities and challenges appear. However, the next section will present a couple of techniques capable of accomplishing a measurable gain in performance. These improvements can then be extrapolated together with the capabilities of current state-of-the-art systems so as to envisage the performance of the next generation systems.

3.3 Review of Technologies / Proposals for HRWS Imaging

The constraints and trade-offs previously presented are mostly due to single-channel and monostatic restrictions. To improve the capabilities of SAR acquisitions, the techniques proposed deal mainly with the number of antennas, the antenna size and the waveforms design.

3.3.1 Displaced Phase Center Antenna (DPCA)

The displaced phase center antenna (DPCA) technique (CURRIE; BROWN, 1992), also known as multiple azimuth phase centers (MAPS), main objective is to improve the azimuth resolution while maintaining the same PRF. From a different perspective, the technique can also be used to reduce the PRF while maintaining the same azimuth resolution, thus increasing the swath width. The idea is to employ a large receive antenna in azimuth, and split it in N individual RF chains while a single transmit phase center is maintained. As a consequence, the beamwidth of the main lobe of each of these sub-antennas is broader, managing therefore to receive a higher Doppler bandwidth within the -3 dB points. An illustration of this beam broadening and the multiple receive channels is depicted in Fig. 3.2 for a four channels system.

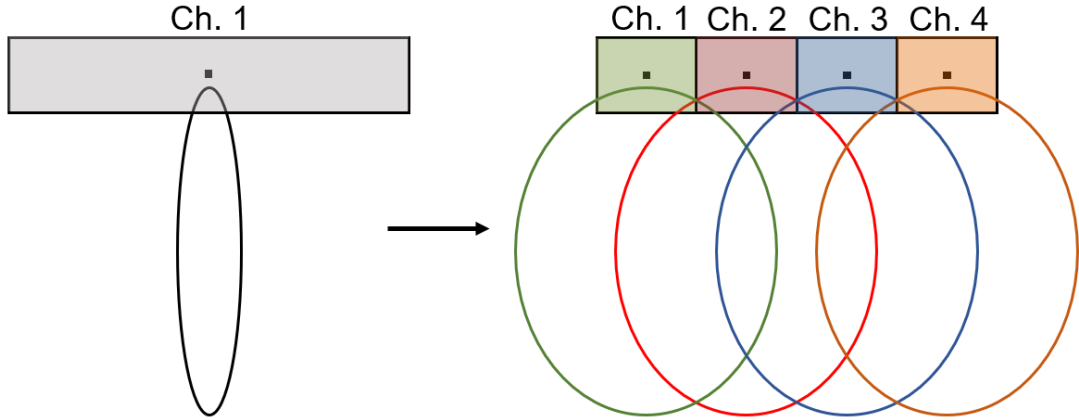


FIGURE 3.2 – Illustration of the four channels split beam broadening of the DPCA technique.

Once each sub-antenna is an independent receive channel, the effective imaging PRF will be N times the actual transmit PRF. Additionally, the effective sampling, which is given by the combination of the samplings of each sub-channel, must be uniform. This restriction is respected by guaranteeing a transmit PRI such that the platform flies exactly half the antenna length between consecutive pulses, leading to

$$\text{PRF}_{\text{DPCA}} = \frac{2 \cdot v_s}{L_a}, \quad (3.2)$$

where v_s is the platform velocity and L_a the antenna length in azimuth. Figure 3.3 depicts schematically how the uniform sampling is achieved with the aforementioned PRF. The yellow dots represent the effective phase center, which is given by the halfway position between the transmit antenna and the receive sub-antenna. The constant distance between the blue dashed lines highlights the uniformity of the sampling.

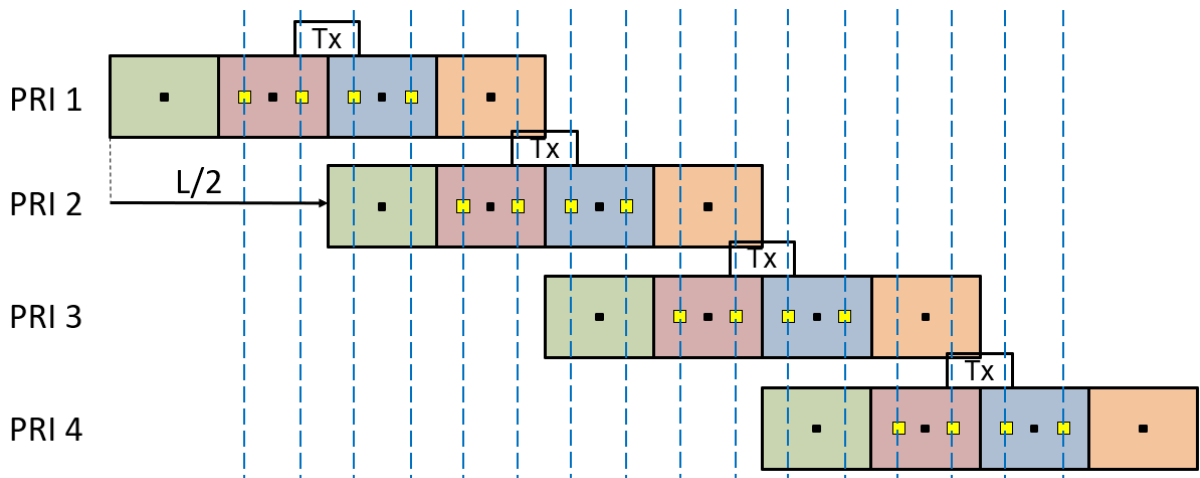


FIGURE 3.3 – Illustration of the uniform sampling achieved by the half antenna displacement of the platform from PRI to PRI.

In practical application, however, this very specific PRF may not always be suitable, i.e., it may lead to Nadir or transmit interference. Once any slight variation in this PRF leads to a non-uniform sampling, an unambiguous signal reconstruction technique must be employed (KRIEGER; GEBERT; MOREIRA, 2004). Finally, the usage of broad beams – leading to lower gains – give rise to concerns on the noise performance of the radar, which are discussed in the next subsections. Azimuth ambiguities, nonetheless, are kept nearly constant after proper reconstruction.

3.3.2 Space-time Coding (STC)

Space-time coding is a technique commonly used in mobile communications, but whose application has only recently been introduced to SAR imaging. In communications, the technique provides a more reliable and stable transmission of data by making use of multiple transmit antennas. The Alamouti code is one of the first space-time block codes and was introduced in 1998 (ALAMOUTI, 1998). In the following years, it was further improved by means of partial feedback and hybrid schemes (AKHTAR; GESBERT, 2004; MACHADO; UCHOA-FILHO, 2004). However, it was only in 2008 by Kim and Wiesbeck that the Alamouti code was first investigated to MIMO SAR applications (KIM; WIESBECK, 2008).

The technique consists of transmitting two orthogonal waveforms simultaneously, in two consecutive periods. Initially, each of the two antennas transmit the orthogonal signals s_1 and s_2 . Then, in the second period, they transmit s_2^* and $-s_1^*$, respectively. Disregarding the time variant characteristic of the channels, the received signals r_1 and r_2 are given by

$$\begin{bmatrix} r_1 \\ r_2 \end{bmatrix} = \begin{bmatrix} s_1 & s_2 \\ s_2^* & -s_1^* \end{bmatrix} \cdot \begin{bmatrix} h_1 \\ h_2 \end{bmatrix} + \begin{bmatrix} n_1 \\ n_2 \end{bmatrix}, \quad (3.3)$$

where h_1 and h_2 represent the uncorrelated channels for each of the transmit antennas.

In SAR applications, contrarily to communications, the signals are well known, and the aim is to acquire the channel state information. Therefore, multiplying Eq. 3.3 by the hermitian of the matrix of the transmit signals (Alamouti decoding matrix S^H), one obtains

$$\begin{bmatrix} z_1 \\ z_2 \end{bmatrix} = \begin{bmatrix} |s_1|^2 + |s_2|^2 & 0 \\ 0 & |s_1|^2 + |s_2|^2 \end{bmatrix} \cdot \begin{bmatrix} h_1 \\ h_2 \end{bmatrix} + \begin{bmatrix} n'_1 \\ n'_2 \end{bmatrix}. \quad (3.4)$$

It is worth noting that after the Alamouti decoding matrix is applied, the range focusing is already done. Therefore, only the azimuth compression needs to be performed to

obtain the focused image. Finally, one could also compensate the time variant characteristic of the channels by introducing a compensation matrix in the decoding procedure. This first Alamouti code applied to SAR imaging obtains a diversity gain of 3 dB. Moreover, by employing multiple receive antennas, not only the total gain increases, but a NESZ improvement is also achieved.

An important and restrictive requirement for this technique is the need to double the PRF to achieve the same azimuth resolution and ambiguity ratio. This is due to the fact that from each of the channels, a different image is formed, leading to two coherent SAR images. To overcome this limitation, DPCA as presented in the previous subsection was suggested. Ultimately, due to the coherence between the two images, interferometry applications are also feasible.

In the following years after the publication by Kim and Wiesback, many improvements and extensions of the Alamouti code applied to SAR image formation have been published (WANG, 2011; HE; DONG; LIANG, 2015; LIU; ZHANG; YU, 2017). Initially, in 2011, Wang proposed to use the orthogonality provided by OFDM into STC, achieving good separability for point targets (WANG, 2011). In 2015, He (HE; DONG; LIANG, 2015) presented an extended STC together with short-term shift-orthogonal waveforms (STSO) (KRIEGER, 2014) capable of eliminating the requirement of doubling the PRF, while also minimizing the time variant channel effects. These improvements were obtained by simultaneous transmission via the orthogonal transmit channels. Later in 2017, Liu (LIU; ZHANG; YU, 2017) proposed the use of frequency comb-like chirp waveforms to achieve better SNR, but the PRF had once again to be doubled.

3.3.3 Orthogonal Frequency Division Multiplexing (OFDM)

Another technique that has long been introduced in mobile communications is OFDM. In SAR applications, however, it was only in 2006 that it made its first appearance for ultra-wideband (UWB) systems (GARMATYUK, 2006). Later in 2010, Kim (KIM *et al.*, 2010) proposed a novel OFDM waveform based on the chirp to achieve a lower peak-to-average power ratio (PAPR), and investigated its coherence for applications in SAR polarimetry. The proposed waveform by itself, however, was not enough to image large swaths, as it was demonstrated by Krieger (KRIEGER *et al.*, 2012). Due to strong cross-correlation between the OFDM waveforms, additionally beamforming was required to suppress these range ambiguities. This led to a further paper from Kim (KIM *et al.*, 2013), in which he described the modulation and demodulation requirements for SAR acquisitions employing OFDM with DBF and multiple transmitters.

The waveforms proposed by Kim in 2013 are designed in the frequency domain by interleaving the original chirp spectra with zeros. Then, a shift is applied to one of the

waveforms to overlap the zeros with the spectrum discrete values. After interpolation through zero padding in the time domain, the OFDM waveforms in the frequency domain can be seen in Fig. 3.4. The demodulation is finally achieved with spatial filtering (typically done through digital beamforming), circular-shift addition, polyphase decomposition and matched filter in the frequency domain (KIM *et al.*, 2013).

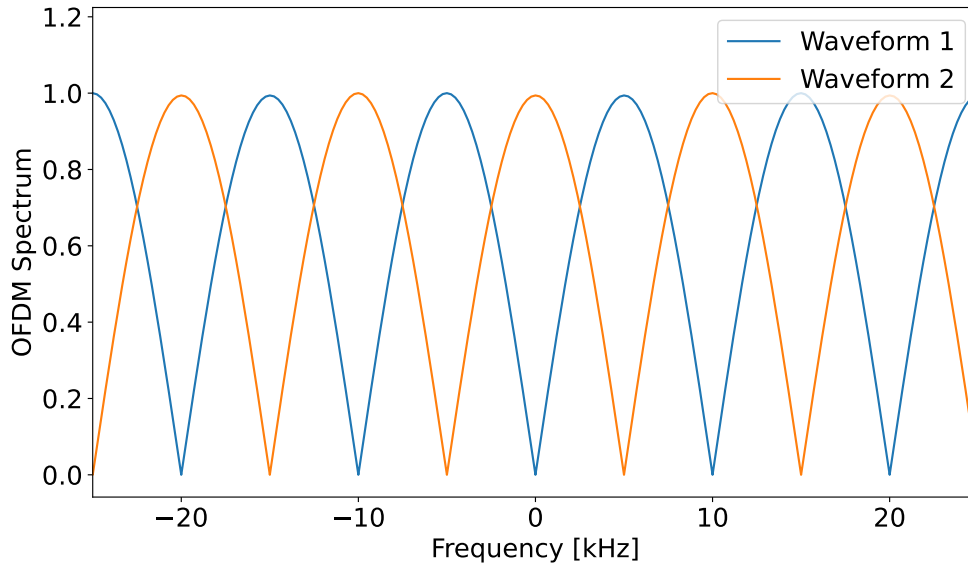


FIGURE 3.4 – Interpolated spectra of the waveforms proposed by Kim for a pulse duration of $100 \mu\text{s}$.

In 2014, Krieger published a comprehensive review of the opportunities and pitfalls for MIMO-SAR acquisitions (KRIEGER, 2014). Once again, the focus was mainly on the unambiguous separability of the innumerable waveforms that were being proposed for MIMO acquisitions at that time. The great confusion arose from the definition of orthogonality, which is, by itself, not enough for extended targets. A more generic definition considering arbitrary shifts in time between the waveforms has to be considered. The shift orthogonality is guaranteed by ensuring

$$\int s_i^*(t) \cdot s_j(t + \tau) dt = 0 \quad \forall \tau \in \mathbb{R}, i \neq j. \quad (\text{KRIEGER, 2014}) \quad (3.5)$$

Apart from PAPR and DBF concerns, Doppler leakage is another restriction that has to be carefully analyzed when using OFDM in SAR acquisitions. It becomes a special concern for high resolution spaceborne imaging. In order to achieve sub-meter azimuth resolution, the Doppler bandwidth must be in the order of 10 kHz. The problem arises from the corresponding maximum processed Doppler frequency being already relevant comparing to the sub-carrier spacing, leading therefore to strong inter-carrier interference (ICI). For instance, a PRF of 3000 Hz with a duty cycle of 30 % already leads to a sub-

carrier spacing of 10 kHz. An estimate of the ICI power was presented in (KIM *et al.*, 2015). Kim showed that if a maximum allowed ICI of -20 dB is desired, then the product between the maximum Doppler shift and the transmit pulse length has to be kept lower than 0.14. This becomes a strong limitation when striving for wide-swaths using lower PRFs.

Due to these restrictive constraints in the use of OFDM, short-term shift-orthogonal waveforms (STSO) together with DBF were introduced by Krieger (KRIEGER, 2014) in 2014. The STSO waveforms are defined, as the name suggests, by the vanishing of their cross-correlation for small time shifts, allowing for an unambiguous reconstruction of extended targets when used in combination with DBF. These waveforms can be very simply constructed by using two traditional linear frequency-modulated chirps with an offset in frequency given by half the bandwidth. These characteristics, therefore, make STSO waveforms a good alternative to OFDM.

3.3.4 Scan-on-Receive (SCORE)

On the one hand, the goal of DPCA is to improve the azimuth resolution. The scan-on-receive technique (SCORE), on the other hand, aims chiefly at extending the swath width. The technique consists of transmitting a broad beam in elevation, covering the whole desired swath. In reception, a long and high gain antenna forming a narrow receive beam sweeps over the target area following the echoes coming from different ground positions. This beamforming on receive is made possible by employing a large number of independent elements in elevation (SUESS; GRAFMUELLER; ZAHN, 2001; SUESS; WIESBACK, 2002; GEBERT; KRIEGER; MOREIRA, 2009).

SCORE takes advantage of the pulses being transmitted simultaneously towards the whole scene, so that in reception, due to the acquisition geometry, there is a time distinction between the ground targets. This allows for the antenna beam to look only at smaller areas on ground at each instant of time with a high gain pencil beam. Ultimately, this high gain in reception further improves the SNR and suppresses the range ambiguities.

An interesting application for SCORE is to image a swath wide enough so that the echoes do not fit completely within one receive echo window. In traditional modes, the echoes arriving at the receive antenna during the wrong echo window are named range ambiguities. However, by combining the pencil beam antenna with DBF techniques in SCORE, it is possible to simultaneously image both the first ambiguities (which are now part of the image) and the scene center. In this situation, one must ensure sufficient beamwidth in transmit to guarantee the imaging of the whole target area, which can be in the order of hundreds of kilometers.

One issue that arises from this technique are the blind ranges caused by the transmit pulses in-between the echo windows. A PRI variation technique named staggered SAR was proposed to overcome this limitation (VILLANO; KRIEGER; MOREIRA, 2014). It consists mainly of varying the PRI from pulse to pulse so that the blind ranges appear at different positions during imaging. Interpolation can then be used to recover the missing samples. SCORE together with staggered SAR is the main imaging mode foreseen to be used in the future Tandem-L mission (HUBER *et al.*, 2018).

3.3.5 Frequency Scanning (F-Scan)

The main drawback of SCORE is the requirement of DBF implemented on board of the satellite to sweep on receive, leading to a high complexity and costly system. An interesting alternative known as frequency scanning (F-Scan) has been recently introduced by Römer (ROEMER, 2017; ROEMER, 2019). The F-Scan technique consists of not only receiving, but also transmitting with a high gain pencil beam, achieving strong improvements in SNR and range performance in terms of sidelobes and ambiguities.

The sweeping occurs over the target area from far to near range accompanied by the chirp linear frequency variation. The scan is achieved via analog beamforming. By making use of true time delay lines (TTDL) and phase shifters, each frequency is associated to one elevation angle. The antenna system is designed so that a linear frequency variation leads to a roughly linear angle scanning. For instance, using an up-chirp, the lowest frequency of the chirp is transmitted to the far edge of the scene, while the highest frequency is transmitted towards the near edge. This mechanism and its comparison with conventional Stripmap mode are schematically represented in Fig. 3.5.

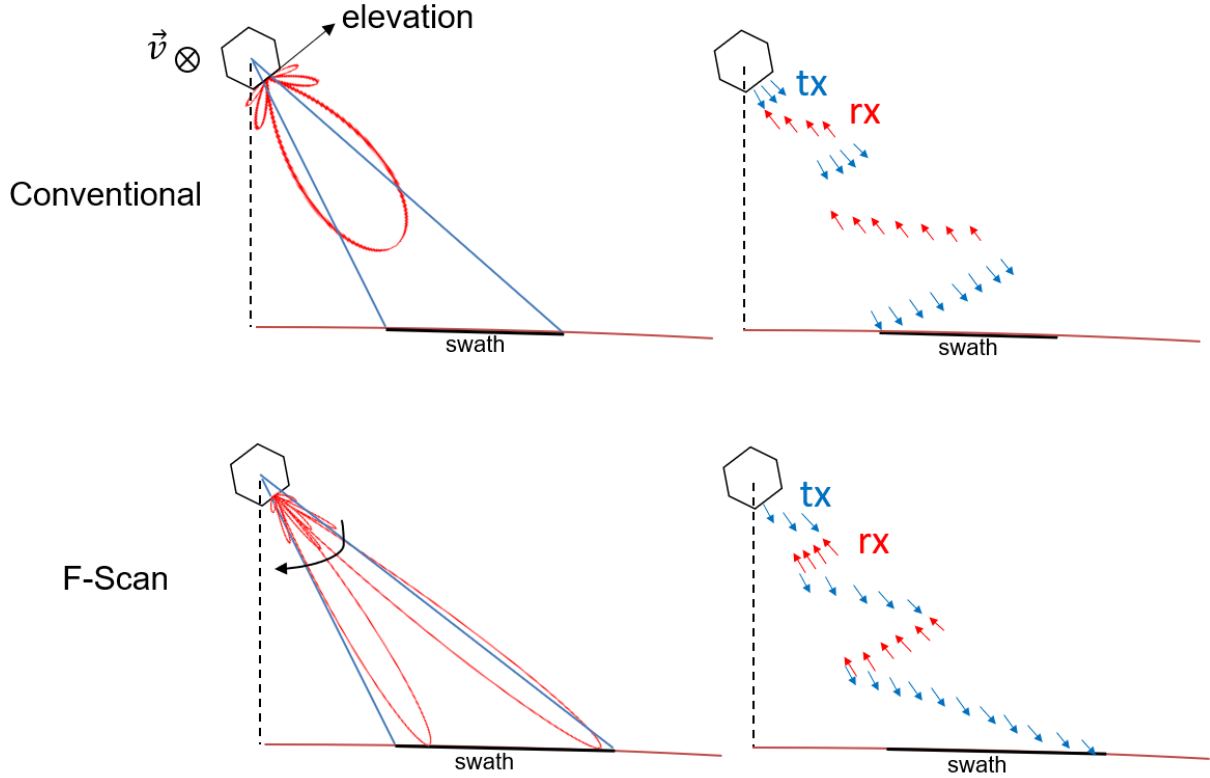


FIGURE 3.5 – Schematic comparing the acquisitions for conventional Stripmap SAR mode with the F-Scan. Conventional Stripmap employs a broad beam and receives first from near range. F-Scan, conversely, sweeps across ground range with a pencil beam by linearly increasing the chirp frequency. As a result, the echoes overlap on receive.

As a consequence of this scanning design, each point target on ground is imaged by an effective bandwidth much lower than the total transmit bandwidth. Thus, the system bandwidth needs to be increased to achieve similar resolution as with conventional SAR systems. Nevertheless, this will not lead to a lack of range resolution compared to current SAR systems. According to the new ITU allocation, the available bandwidth for active radars has been extended to 1.2 GHz (ROEMER *et al.*, 2018). This wide band guarantees an approximately minimum effective bandwidth of 150 MHz for swaths wider than 50 km and an antenna of 1.4 m in elevation, enough to achieve the sub-meter range resolution (MITTERMAYER *et al.*, 2022).

Another advantage of F-Scan is the echo compression on receive caused by the scanning on transmit. Traditional SAR systems transmit towards the whole scene simultaneously. F-Scan, conversely, starts the transmission towards far range, in such a way that the echoes from far and near range may arrive simultaneously at the receive antenna. This compression of the echoes leads to a much shorter required echo window length. The limitation is that the wider the swath width, the longer the transmit pulses need to be to achieve this overlapping characteristic. Nonetheless, still a more efficient use of the time domain is obtained, leading to wider scenes for a given PRF, when compared to

conventional imaging. Additionally, the longer transmit pulse is beneficial as it allows for a lower peak transmit power or SNR improvements due to the higher average power.

In summary, the F-Scan can achieve high range resolution, wide swaths, and improved SNR, range ambiguity and sidelobe ratios. This is realized by a much lower complexity and affordable system design when compared to digital beamforming techniques. The drawback is mainly the loss between the total and the effective bandwidth. Due to these characteristics, F-Scan has been considered as the reference technique in elevation for the future HRWS X-band German spaceborne SAR mission (BARTUSCH *et al.*, 2021a).

3.4 Concluding Remarks

The limitations of the current generation of spaceborne SAR systems were described in Sections 3.1 and 3.2. It was shown that the monostatic and single-channel aspects of these systems impose strong constraints, impeding the further improvement of their capabilities. Therefore, most of the current techniques focus on features related to MIMO systems, i.e., multiple antennas and multiple channels.

At the current stage of development, several techniques have already been presented in the literature, such as the ones described in Section 3.3. However, it is clear that there can be interactions between the various approaches. Currently, the main line of research is not only on the development of novel techniques making use of the multi-channel features, but also on how to put them together in constructive fashions.

In the literature, many strategies of merging previously proposed techniques can be found (HUBER *et al.*, 2018; BARTUSCH *et al.*, 2021a; WANG, 2011; LIU; ZHANG; YU, 2017). However, due to their innovative and cutting-edge aspects, they are not always directly suitable for real applications as they unintentionally overlook hidden constraints (KRIEGER, 2014). From the future research, therefore, novel ideas and better integration of the many available techniques are demanded.

Ultimately, even though an idea may seem highly promising, the costs of implementation have to be carefully analyzed. For instance, DBF has been widely considered and investigated in the literature. However, the amount of complexity and costs involved, such as the huge amount of data, large number of T/R modules and independent receive channels, and the new processing techniques required, make its real implementation a big challenge and strongly dependent on the frequency band considered. Therefore, one can expect the investigation of making all the novel techniques financially feasible to be also a key line of research.

In order to improve the azimuth resolution, DPCA has been initially presented. Its

main drawback was shown to be the much higher amount of data additionally created by each of the azimuth channels. Space-time coding techniques were subsequently introduced and shown to provide diversity gains at the cost of a higher PRF, leading to narrower scenes, and the need of having two transmitters. Then, OFDM waveforms, which provide orthogonality, and, therefore, separation between the signals in MIMO applications, were introduced. The requirement of using DBF, the concern on Doppler leakage (ICI) and PAPR issues were shown to be the main restrictions of this technique. STSO was shown to be a good alternative to OFDM, as it does not lead neither to ICI nor to PAPR issues, but still requires DBF. Finally, so as to achieve wide-swath capabilities, SCORE with staggered SAR and F-Scan were described. The former making use of DBF, while the latter of analog beamforming. The main trade-off between these scanning modes are costs and complexity for performance.

Due to its wide-swath and cost-effective characteristics, it is understandable and clear why F-Scan was chosen to be in the next HRWS German mission (BARTUSCH *et al.*, 2021b). Concerning the concurrent mode, the technique is also quite fitting, as it relaxes some constraints on range performance and achieves wider scenes. Therefore, the investigation of the concurrent imaging mode paired with the F-Scan is of great interest in this thesis. The next chapter is responsible for designing and describing such a mode.

4 Concurrent Imaging with F-Scan

4.1 HRWS System Parameters

Naturally, different systems lead to different trade-offs between cost, complexity, performance and many other factors. So, to conduct a comprehensive and meaningful investigation of the performance that is achieved when combining the F-Scan with the concurrent imaging technique, it is essential that the system is well determined from the beginning of the analysis. This section will explicit the system parameters considered in this thesis, serving as a foundation for the following sections.

4.1.1 Orbital Parameters

The system considered in this thesis is a spaceborne platform in a LEO orbit. For the numerical values of the orbit position, velocity and attitude, the sun-synchronous TerraSAR-X satellite data is used. More details of the orbit can be found in (KAHLE; D'AMICO, 2014).

The coordinate system and Earth model are based on the Earth-centered, Earth-fixed (ECEF) WGS-84 reference frame. This world geodetic system uses the International Earth Rotation and Reference Systems Service (IERS) Reference Pole (IRP) as the z-axis, and the intersection of the IERS Reference Meridian (IRM) – 0° longitude – and the plane passing through the origin (Earth's center of mass) and normal to the z-axis as the x-axis. The coordinate system is graphically depicted in Fig. 4.1.

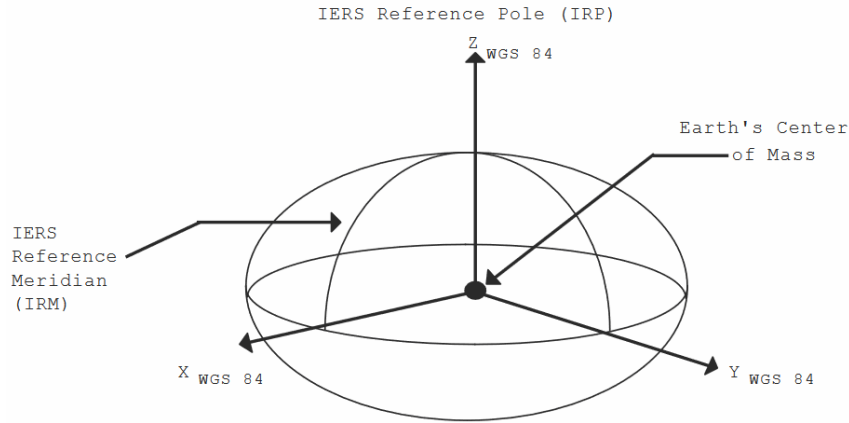


FIGURE 4.1 – WGS-84 Coordinate System Definition (NATIONAL IMAGERY AND MAPPING AGENCY, 2000).

Moreover, WGS-84 approximates Earth's surface to an ellipsoid. The primary ellipsoid parameters can be found in Table 4.1.

TABLE 4.1 – WGS-84 primary ellipsoid parameters. (NATIONAL IMAGERY AND MAPPING AGENCY, 2000)

Parameter	Notation	Value
Semi-major Axis	a	6378137.0 m
Reciprocal of the Flattening Factor	$1/f$	298.257223563
Angular Velocity of Earth	ω	7292115×10^{-11} rad/s
Earth's Gravitational Constant	GM	$(3986004.418 \pm 0.008) \times 10^8$ m ³ /s ²

The coordinate system used alongside the ellipsoid allows to determine satellite and target positioning in a common and well-defined reference frame. This will be essential in the following discussions to reliably and precisely represent simulated acquisitions. It is important to highlight that in some discussions the spherical model of Earth with a radius of 6371 km will be considered to derive closed-form expressions, and facilitate the understanding. This value represents the average radius of Earth.

4.1.2 Platform Parameters

The platform itself, in this case a satellite, is considered to be endowed with a phased-array antenna that operates in the X-Band with a center frequency of 9.8 GHz. Due to the new ITU allocation, the bandwidth is extended to 1.2 GHz (ROEMER *et al.*, 2018), in comparison to the 300 MHz of TerraSAR-X. The duty cycle is set to a maximum of 30 % (MITTERMAYER *et al.*, 2022).

Moreover, the active phased-array antenna consists of a grid of 12 by 64 elements in azimuth/elevation, with a total size of 6.0 m by 1.4 m. In azimuth, every block of three elements is endowed with its own RF chain, so that up to four channels can be used simultaneously. Each block of 3 by 64 elements (1.5 m by 1.4 m) is named a leaf, and represents the smallest functional entity of the antenna front-end, encompassing all functions necessary to ensure beam steering and beamshaping of the phased array antenna. Electrically, each leaf comprises transverse electromagnetic (TEM) radiators, transmit/receive (T/R) modules, switchable true time delay lines (TTDLs), and a power and control unit (BARTUSCH *et al.*, 2021a; ROEMER *et al.*, 2018). The antenna modeling will be further described in Section 4.3.

Finally, once multiple channels are available in azimuth, applying the DPCA technique is also of great interest. As described in Section 3.3, the radar must use a specific PRF as given in (3.2). For the aforementioned antenna size, the target DPCA PRF is then given by

$$\text{PRF}_{\text{DPCA}} = \frac{2 \cdot v_s}{L_a} \approx \frac{2 \cdot 7605 \text{ m/s}}{6.0 \text{ m}} = 2535 \text{ Hz.} \quad (4.1)$$

4.2 Concurrent F-Scan Timing and Interference Assessment

4.2.1 F-Scan Timing Considerations

The basic idea of the F-Scan technique was described in Section 3.3. The design of such a mode, however, has to pass through timing and ambiguities analyses in a similar way to what was described in Chapter 2. The main difference compared to traditional imaging is related to the scanning of the antenna in elevation, which changes the timings and the range behavior.

First of all, let us define the transmission of a generic F-Scan acquisition so as to introduce the main parameters of interest. Defining f as the instantaneous transmit frequency, f_c as the center frequency (9.8 GHz), B_t as the total bandwidth (1200 MHz), β as the look angle (subscripts n and f for near and far range), HPBW_{el} as the half power beamwidth of the antenna in elevation, τ as the fast time, and, finally, t_p as the transmit pulse duration, Fig. 4.2 depicts the instantaneous transmit frequency of an F-Scan acquisition with an up-chirp in terms of look angle and fast time.

It is worth noting that the antenna is configured (via TTDL and phase shifters) in such a way that to each frequency f its main lobe has its peak pointing to β . So, it is obvious

that to each frequency, actually, every point on Earth's surface that is within the field of view of the antenna is being imaged. Figure 4.2 is only depicting the relation between the instantaneous frequency of the transmit pulse and the look angle of maximum gain. Due to the sinc-like aspect of the antenna pattern that works like a spacial filter, however, only the areas within the main lobe receive significant amounts of energy.

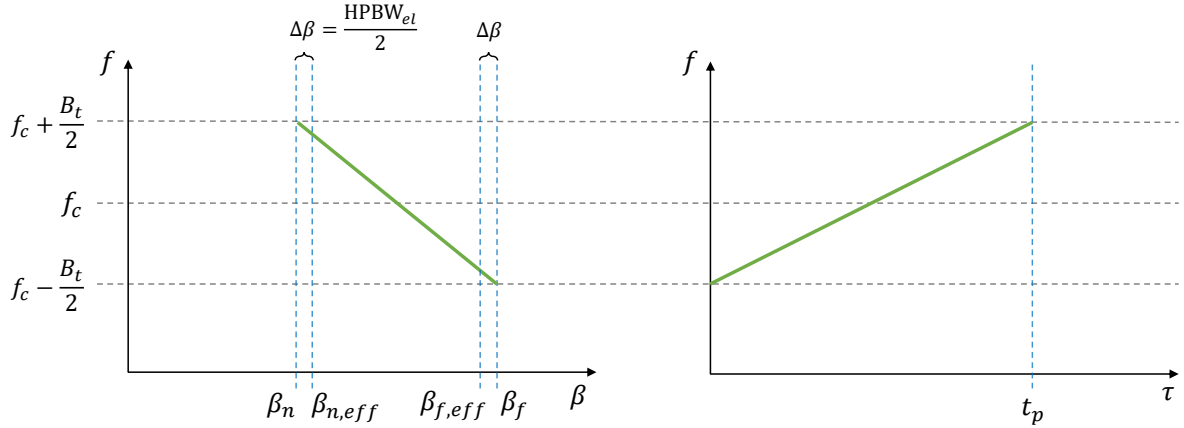


FIGURE 4.2 – F-Scan instantaneous transmit frequency in terms of fast time and look angle of the peak of the main lobe.

In this work only the up-chirp case is analyzed, as the behavior for a down-chirp is very similar.

An important aspect to observe in F-Scan acquisitions is that the effective imaged scene – the look angles between $\beta_{n,eff}$ and $\beta_{f,eff}$ – is lower than the total imaged scene. This effect arises from the definition that a target is only considered as completely imaged if it is swept by the whole main lobe (between the -3 dB points). This becomes clearer with a visual representation, as depicted in Fig. 4.3. For future work, one could also consider processing more than only the HPBW to increase the range resolution. However, this would come at the expense of a lower SNR and a higher sampling rate, leading to a higher amount of data to be downlinked.

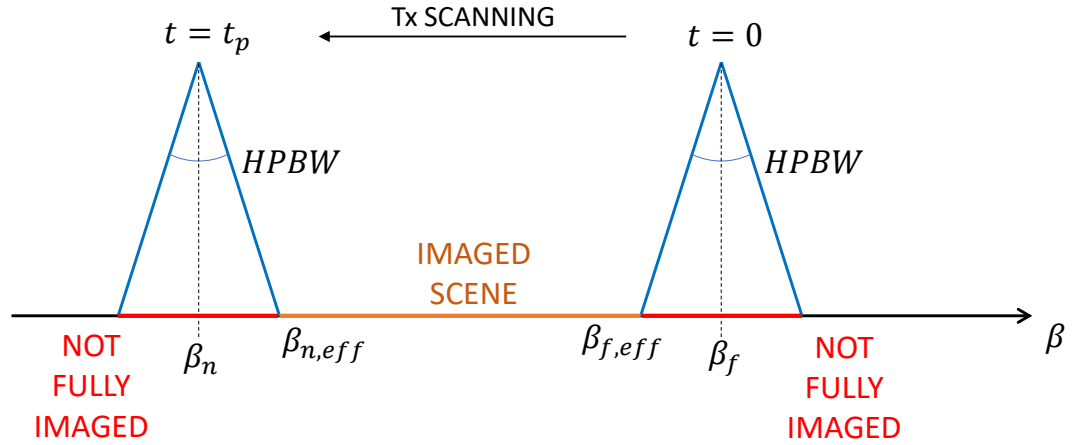


FIGURE 4.3 – Angular scanning of the F-Scan highlighting the effective imaged scene in contrast to the total imaged area.

Given that the antenna starts the transmission pointing with maximum gain to β_f and stops at β_n , the effective near and far look angles of the scene are then given by

$$\begin{cases} \beta_{f,eff} = \beta_f - \frac{HPBW_{el}}{2} \\ \beta_{n,eff} = \beta_n + \frac{HPBW_{el}}{2} \end{cases} \quad (4.2)$$

To assess the timings – determine when the echoes arrive at the antenna – one must know when each point target within the scene starts to be imaged, and how long the imaging takes. The first instant of the acquisition is when the target at $\beta_{f,eff}$ starts to be imaged, while the last instant is when the imaging of $\beta_{n,eff}$ ends. Moreover, the peak of the main lobe of the antenna sweeps from β_f to β_n in a time duration of t_p . Therefore, approximating the angular sweeping of the antenna to be linear in time (this approximation will be further discussed in the next section, see Fig. 4.21), i.e., considering the left plot of Fig. 4.2 to be linear, the time the antenna takes to sweep a half power beamwidth is straightforwardly obtained by

$$t_{dwell} = \frac{HPBW_{el}}{\beta_f - \beta_n} \cdot t_p = \frac{HPBW_{el}}{\beta_{f,eff} - \beta_{n,eff} + HPBW_{el}} \cdot t_p. \quad (4.3)$$

In summary, the dwell time gives the information of the illumination time for any given point within the scene. Consequently, one can derive that the transmission towards near range starts after $t_p - t_{dwell}$. This first instant of transmission with the leading edge of the main lobe is referenced here by the symbol t_l , and is given by

$$t_l(\beta) = \left(\frac{\beta_{f,eff} - \beta}{\beta_{f,eff} - \beta_{n,eff}} \right) \cdot (t_p - t_{dwell}) \quad \forall \beta \in [\beta_{n,eff}, \beta_{f,eff}]. \quad (4.4)$$

Given a model for Earth's surface and the platform position, it is also possible to obtain the duration the transmitted signals take to be received as echoes at the receive antenna (echo delay). As a matter of mathematical description, let us consider Earth to be spherical with radius $R_e = 6371$ km. This model with its respective parameters of interest are schematically depicted in Fig 4.4.

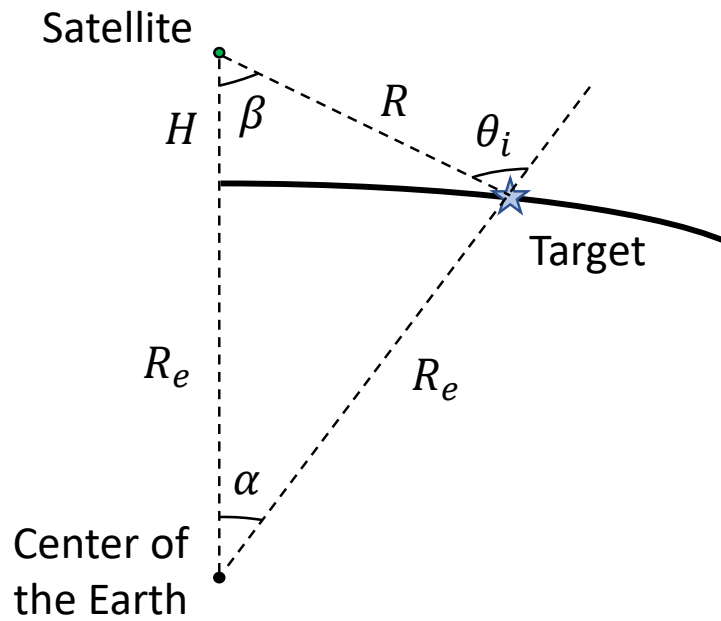


FIGURE 4.4 – Spherical Earth representation of a SAR acquisition.

Once the satellite height, the look angle and Earth's radius are already given as inputs, the slant range has to be calculated to derive the delay of the echoes by $t_{delay} = 2R/c$. First, using the law of sines, the incidence angle is obtained

$$\theta_i = \sin^{-1} \left[\left(1 + \frac{H}{R_e} \right) \cdot \sin \beta \right]. \quad (4.5)$$

Then, α is derived by $\alpha = \theta_i - \beta$. The slant range is calculated by

$$R = \frac{\sin \alpha}{\sin \beta} \cdot R_e. \quad (4.6)$$

Ultimately, the echoes delay as a function of the look angle is a non-linear relation. A numerical simulation for a satellite height of 514 km is depicted in Fig. 4.5.

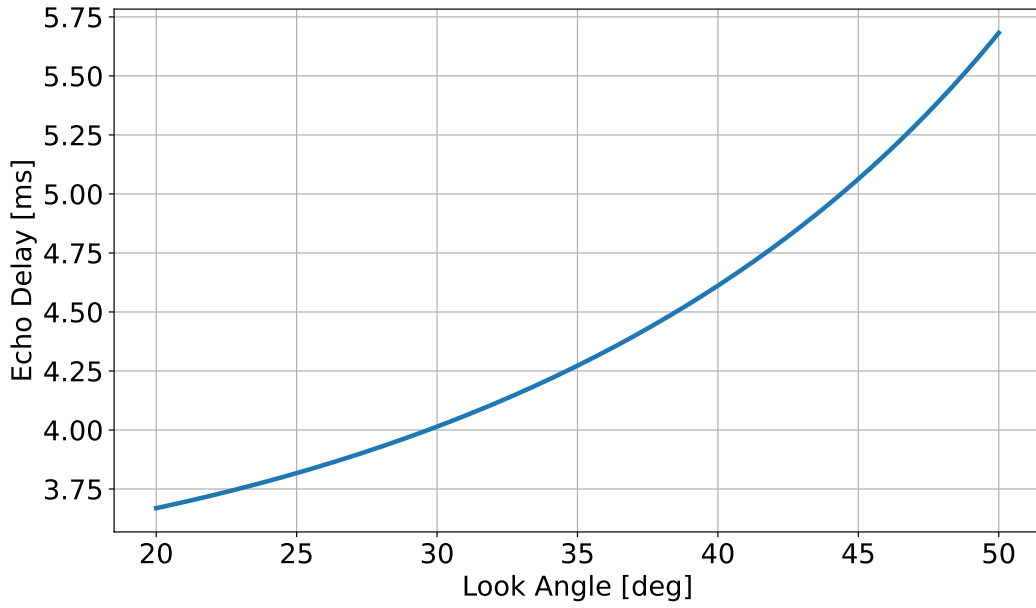


FIGURE 4.5 – Echo delay as a function of the look angle.

The required parameters to derive the timings for an F-Scan acquisitions were already well determined above. Assuming the start of the radar transmission at the instant zero, it transmits towards β at the instant $t_l(\beta)$, the echoes take $t_{delay}(\beta)$ to arrive at the antenna, and the reception for each target takes t_{dwell} . At this point, all these parameters could already be plotted to provide a visualization of the timings. However, an important characteristic intrinsic to the F-Scan must be analyzed first.

The F-Scan starts transmitting towards far range, the region where the echo delay is the largest. Conversely, the last transmission is towards near range, where the echo delay is the shortest. Therefore, it is imaginable that there is a certain pulse duration that compensates the variation of the echo delay from far to near range. Mathematically, the echoes of the near and far range arrive at the antenna after a time $t_{echo} = t_l + t_{delay}$ given by

$$\begin{cases} t_{echo}(\beta_{f,eff}) = 0 + \frac{2R_{f,eff}}{c_0} \\ t_{echo}(\beta_{n,eff}) = t_p - t_{dwell} + \frac{2R_{n,eff}}{c_0}. \end{cases} \quad (4.7)$$

Imposing the condition $t_{echo}(\beta_{f,eff}) = t_{echo}(\beta_{n,eff})$, it results in

$$t_{p,overlap} = \frac{2}{c_0}(R_{f,eff} - R_{n,eff}) + t_{dwell} = \frac{2}{c_0}(R_{f,eff} - R_{n,eff}) \left(1 + \frac{HPBW_{el}}{\beta_{f,eff} - \beta_{n,eff}} \right). \quad (4.8)$$

Equation (4.8) defines the pulse duration that is required to ensure that the echoes from the near and far range will overlap on receive. This scenario is named here as the *fully-overlapped* case. This is a very special characteristic of the F-Scan technique, as it allows for a very short receive echo window. More specifically, the required echo window is given by the dwell time, which is only a fraction of the pulse duration.

Ultimately, the mathematical description above can be summarized in a couple of figures depicting the relation between distance (target range), time and frequency of the received echoes. In order to turn the analysis understandable, the three dimensional behavior can be projected into each of the three planes. Figures 4.6, 4.7 and 4.8 exemplify the reception of the echoes in each of the three planes of interest for a fully-overlapped acquisition. The blue and orange lines represent the beginning and end of receiving the echoes, respectively.

The simulated acquisition consists of a target region between the incidence angles of 33.70° and 38.75° , covering a swath width of 61 km. The pulse duration leading to this fully-overlapped scenario is $300.89 \mu\text{s}$. With a total bandwidth of 1200 MHz and a 1.4 m antenna in elevation, an effective bandwidth of 240 MHz is achieved.

From Fig. 4.6 the overlap between the echoes from near and far range becomes clear. It is interesting to observe that during most of the reception, echoes from the whole scene are being received simultaneously. However, they do not arrive at the antenna at the same time, i.e., it is not a perfect overlap of the whole scene. This is due to Earth having a curvature that does not match the linear scanning of the F-Scan. If desirable, one could think of adjusting the linear FM chirp into a non-linear chirp to compensate Earth's curvature, so that the reception of the whole scene would perfectly overlap. This is, however, outside the scope of this thesis.

Apart from the fully-overlapped aspect, some other features of the imaging can be seen in Fig. 4.6. For instance, the vertical height of the gray area depicts the swath width of the scene in the slant range domain. Besides, the horizontal width is exactly the dwell time.

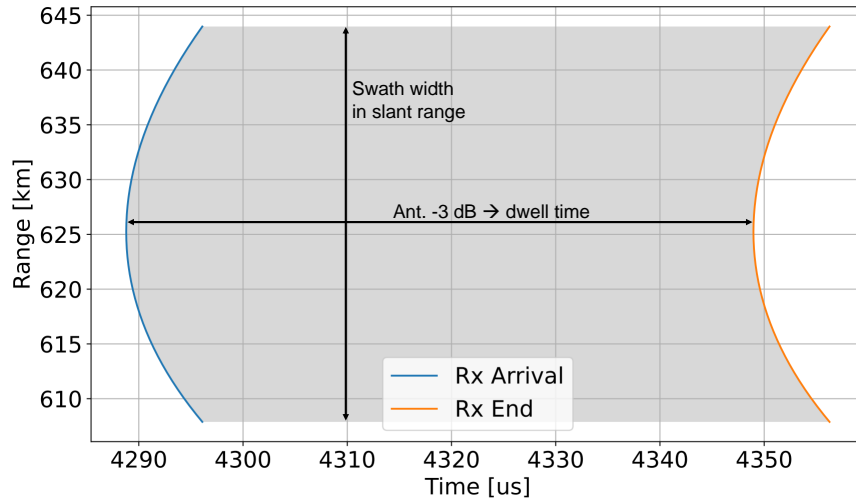


FIGURE 4.6 – Reception of the echoes in the time by slant range domain for a fully-overlapped acquisition.

On a first glance, the instantaneous frequency of the echoes would not influence the timing analysis. Nevertheless, investigating and understanding this extra dimension enables further possibilities that will be shown to be very useful in F-Scan acquisitions. From a frequency perspective, at this point of the analysis it is probably already clear that only a fraction of the total transmit bandwidth is effectively present in the echoes from each target within the scene. Once each target is only imaged during the dwell time, and the total transmit bandwidth is sent linearly during the pulse duration, then the effective bandwidth is given by

$$B_{eff} = \frac{t_{dwell}}{t_p} \cdot B_t = \frac{HPBW_{el}}{\beta_f - \beta_n} \cdot B_t. \quad (4.9)$$

Figure 4.7 shows with which frequencies each target is imaged. The vertical distance between the two lines depicts exactly the effective bandwidth. Ultimately, this is the value that determines the range resolution of the F-Scan imaging. The slant range resolution can be calculated by

$$\delta_{rg} = \frac{0.886 \cdot c_0}{2 \cdot B_{eff}} \cdot \gamma_{w,r}, \quad (4.10)$$

where $\gamma_{w,r} \approx 1.32$ is the broadening factor in range due to the Hamming window (CUMMING; WONG, 2005).

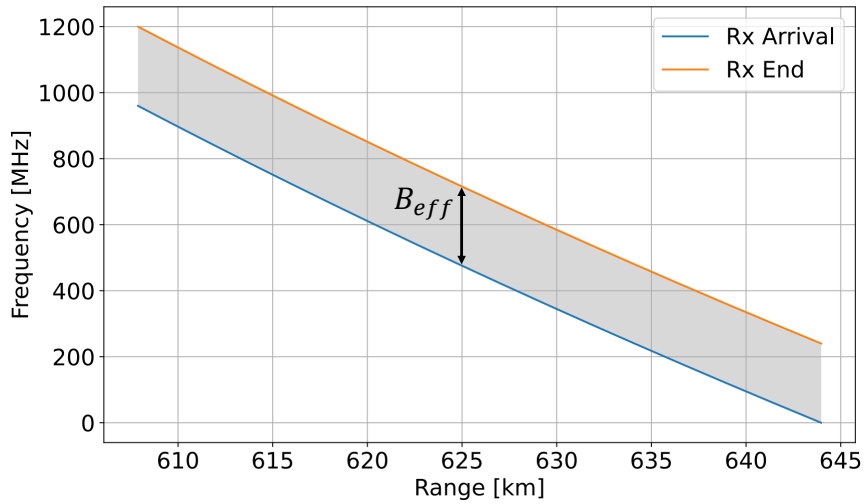


FIGURE 4.7 – Reception of the echoes in the slant range by frequency domain for a fully-overlapped acquisition.

Finally, the richest visualization from the timing analysis point of view is Fig. 4.8. This visualization allows the receiver to know not only when the echo window must be opened and closed, but also shows the required band-pass filters and minimum sampling. Moreover, the dwell time, effective bandwidth and FM rate are also present in the plot.

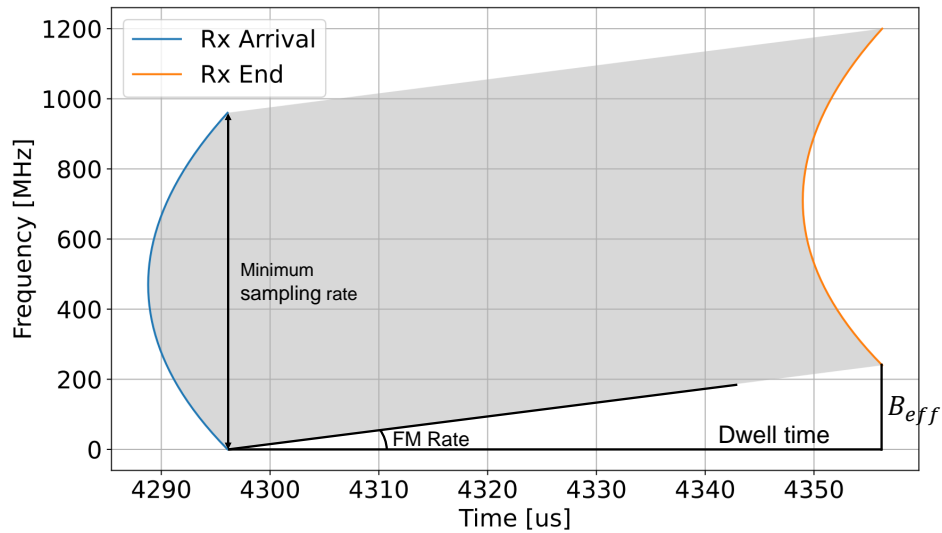


FIGURE 4.8 – Reception of the echoes in the time by frequency domain for a fully-overlapped acquisition.

At first sight, one could expect a huge improvement in swath width, as for whatever scene size the fully-overlapped F-Scan requires only a very short echo window. However, according to (4.8), the trade-off here is a much larger transmit pulse as the scene increases. On the bright side, this allows higher duty cycles, which can mean either higher SNR or relaxing the peak transmit power. Realistically speaking, a very high duty cycle in the

order of 80 % is not feasible for such a system due to hardware constraints. In this thesis the allowed duty cycle was set to a maximum of 30 % to comply with this real-world constraint, as proposed by Mittermayer (MITTERMAYER *et al.*, 2022).

The F-Scan is not limited to only the fully-overlapped case. Actually, any pulse duration deviation from (4.8) will lead to the *partially overlapped* case. In these situations, there will still be some overlap between the echoes, but far and near range are no longer simultaneously received. The use of shorter pulses leads to a more familiar situation, in which near range echoes arrive first. On the other hand, longer pulses generate an opposite and uncommon effect, where the far range echoes arrive first. Due to the duty cycle limitation of 30 %, these echo reversal scenarios are not further investigated here.

For instance, imaging the same area as previously described but with lower pulse durations, the time by frequency behavior of the echoes is depicted in Figs. 4.9a and 4.9b. It becomes clear that by reducing the pulse duration the overlap also reduces. As an effect, the required receive echo window is also visibly longer.

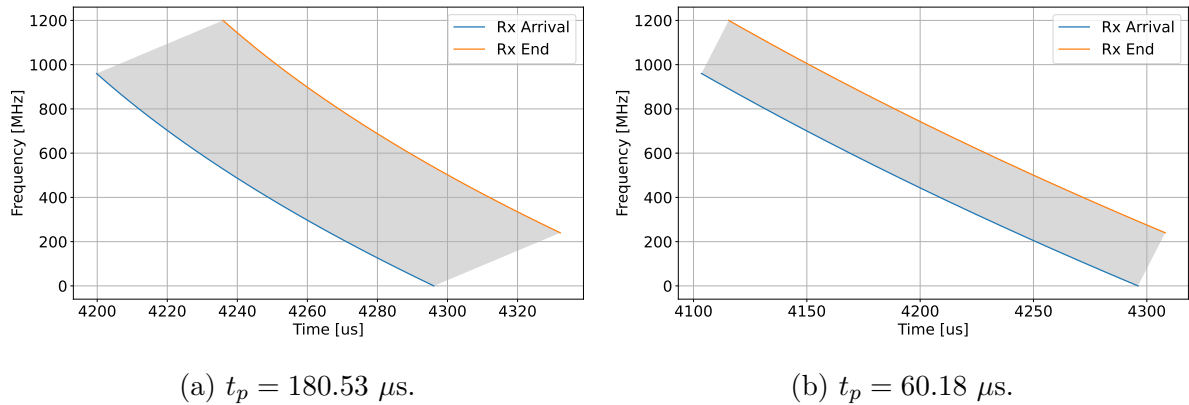


FIGURE 4.9 – Reception of the echoes in the time by frequency domain for partially-overlapped acquisitions.

A useful definition to compare an arbitrary pulse duration t_p to the one leading to the fully-overlapped scenario – $t_{p,overlap}$ previously introduced in (4.8) – is the operation point, defined by

$$O_p = \frac{t_p}{t_{p,overlap}} \geq 0 \quad (\text{YOUNIS } et al., \text{ In review}). \quad (4.11)$$

The previous analysis showed that when $O_p = 1.0$ (fully-overlapped scenario) the receive echo window is the shortest, but the pulse duration is long, and proportional to the scene size. For $O_p < 1.0$, the echo window gets longer, but the transmit pulse becomes shorter. Therefore, it is of interest to investigate the behavior of the minimum required time (PRI_{min}) for transmission and reception, i.e., how efficient the use of the time domain

is. Considering a guard time of t_{guard} and a required echo window t_{rx} , the minimum pulse repetition interval is obtained by

$$\text{PRI}_{min, \text{F-Scan}} = t_p + t_{rx} + t_{guard}. \quad (4.12)$$

Consequently, the maximum PRF that would enable such acquisition is

$$\text{PRF}_{max, \text{F-Scan}} = \frac{1}{\text{PRI}_{min}} = \frac{1}{t_p + t_{rx} + t_{guard}}. \quad (4.13)$$

The required echo window t_{rx} is simply the duration in which the echoes arrive. It can be assessed visually in Figs. 4.6, 4.8 and 4.9, and is derived by simulation in this work. To achieve more efficient use of the time domain, higher values of PRF_{max} are desirable. Moreover, one can compare the F-Scan PRF_{max} with this same value for a typical Stripmap SAR acquisition. The maximum PRF for a Stripmap acquisition not using F-Scan is simply given by

$$\text{PRF}_{max, \text{SM}} = \frac{1}{2 \cdot \text{DC} \cdot \text{PRI}_{min} + t_{swath} + t_{guard}} \rightarrow \text{PRF}_{max, \text{SM}} = \frac{1 - 2 \cdot \text{DC}}{t_{swath} + t_{guard}}, \quad (4.14)$$

where $t_{swath} = \frac{2}{c_0} \cdot (R_{f,eff} - R_{n,eff})$ and $\text{DC} < 50\%$.

For instance, considering a guard interval of $8 \mu\text{s}$ and a duty cycle of 18% , Fig. 4.10 depicts the maximum PRF of the Stripmap F-Scan as a function of the operation point in comparison with a typical Stripmap (YOUNIS *et al.*, 2021).

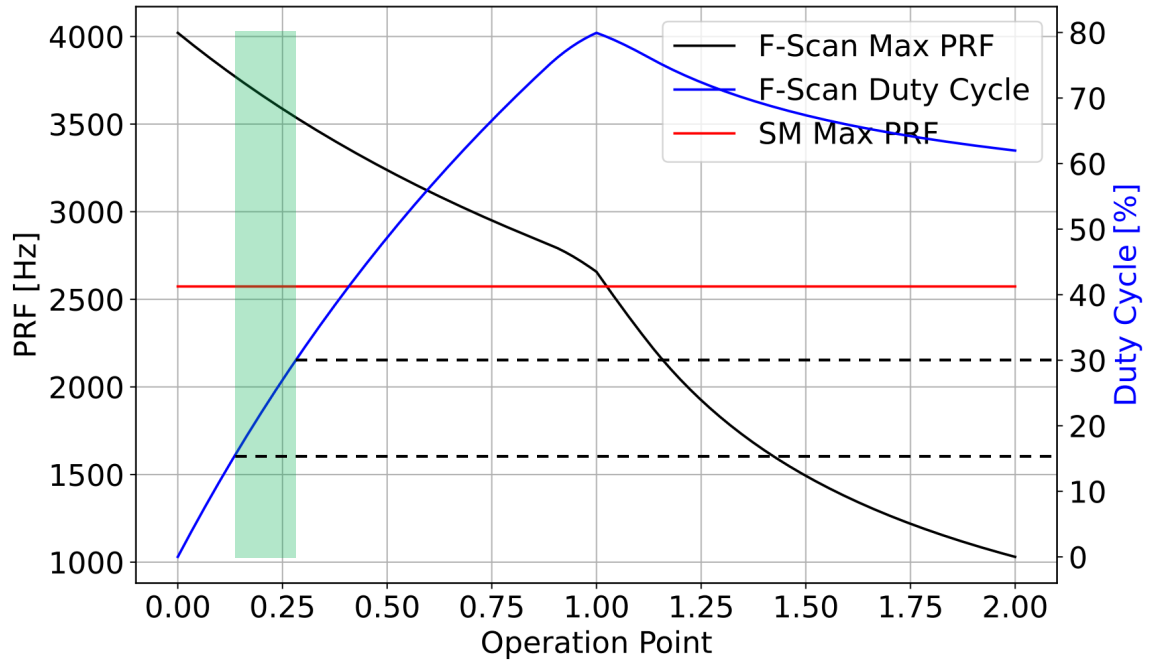


FIGURE 4.10 – Maximum PRF from a timing point of view of an F-Scan acquisition in comparison with a traditional Stripmap as a function of the pulse duration. The region of interest due to duty cycle and SNR limitation is in green.

Conversely to what one would initially expect, the fully-overlapped case is not the most efficient from a timing perspective. Actually, shorter pulses are preferable. Naturally, there is a limit in reducing the pulse duration, as the reduction of the duty cycle deteriorates the SNR of the final image. According to (CUMMING; WONG, 2005), the SNR of a SAR acquisition is directly proportional to the duty cycle and to the two-way gain. Assuming the HRWS F-Scan system described in Section 4.1 with similar losses, noise figure, temperature, platform velocity, wavelength and peak transmit power as TerraSAR-X imaging the same target. In order to achieve the same SNR performance it must be assured

$$\begin{aligned}
 \text{SNR}_{\text{TSX}} &= \text{SNR}_{\text{HRWS}} \\
 (\text{DC})_{\text{TSX}} \cdot A_{\text{TSX}}^2 &= (\text{DC})_{\text{HRWS}} \cdot A_{\text{HRWS}}^2 \cdot \frac{t_{\text{dwell}}}{t_p} \\
 (\text{DC})_{\text{TSX}} \cdot A_{\text{TSX}}^2 &= (\text{DC})_{\text{HRWS}} \cdot A_{\text{HRWS}}^2 \cdot \frac{B_{\text{eff}}}{B_t}.
 \end{aligned} \tag{4.15}$$

Replacing the respective antenna sizes, TerraSAR-X typical Stripmap duty cycle and aiming at an F-Scan bandwidth of 300 MHz, which is the maximum achieved by TerraSAR-X, the F-Scan equivalent duty cycle is

$$\begin{aligned}
(\text{DC})_{\text{HRWS}} &= (\text{DC})_{\text{TSX}} \cdot \left(\frac{A_{\text{TSX}}}{A_{\text{HRWS}}} \right)^2 \cdot \frac{B_t}{B_{\text{eff}}} = 0.18 \cdot \left(\frac{0.7 \cdot 4.8}{1.4 \cdot 6.0} \right)^2 \cdot \frac{1200}{300} \\
(\text{DC})_{\text{HRWS}} &= 11.52\%.
\end{aligned} \tag{4.16}$$

Even though this duty cycle of 11.52 % leads to the same SNR as TerraSAR-X given the constraints explained, a quantitative SNR analysis is hard and usually uncertain once a real system still does not exist. For instance, parameters such as the system losses, the temperature of the receiver, the receiver noise figure and the peak transmit power influence directly on the final numerical SNR. In view of this difficulty in obtaining a quantitative value for the SNR, the duty cycle will be simply restricted from 15 % to 30 % in this thesis, and no further investigation on it will be done.

4.2.2 Concurrent Imaging Timing Aspects with F-Scan

Compared to typical Stripmap acquisitions, the concurrent mode differs in most aspects by a factor of two. Typical Stripmap acquisitions image one target, with one pulse duration, one PRF and one Nadir delay. In concurrent Stripmap acquisitions, conversely, there are two target scenes usually far apart, in the order of hundreds of kilometers. Moreover, independent transmit pulses are employed to each of the targets. Therefore, the concurrent imaging is characterized by two PRFs, duty cycles, incidence angles and Nadir delays, one for each target area.

The idea of using different PRIs to each scene was named as the Multiple PRI technique (RIBEIRO *et al.*, 2022). In these situations, each mode has its own PRF, so that the effective PRF can be calculated by

$$\text{PRF}_{\text{eff}} = \frac{1}{\frac{1}{\text{PRF}_{SM}} + \frac{1}{\text{PRF}_{ST}}}. \tag{4.17}$$

This idea introduces flexibility in the use of the time domain by the acquisition, leading to greater availability and performance for the concurrent mode globally. Even for concurrent Stripmap acquisitions with the same swath width, the different incidence angles lead to different required echo windows. Therefore, tailoring the PRI of each imaging mode brings a more efficient use of the time domain.

Once the F-Scan is a technique that only introduces scanning in elevation, the overall pulse-like transmit and receive structure remains unchanged. Therefore, the concurrent imaging aspects can be straightforwardly applied with F-Scan. For instance, assuming a concurrent F-Scan acquisition of two targets 330 km apart, each with a swath width of

30 km. The PRFs used are 5650 Hz (30 % duty cycle) for the SM acquisition and 4600 Hz (15 % duty cycle) for the ST acquisition, while the incidence angles of near range are 31.50° and 54.57° . The transmit, receive and Nadir events for this acquisition are summarized in Fig. 4.11. The plot depicts the events schematically in amplitude, and it is not to scale.

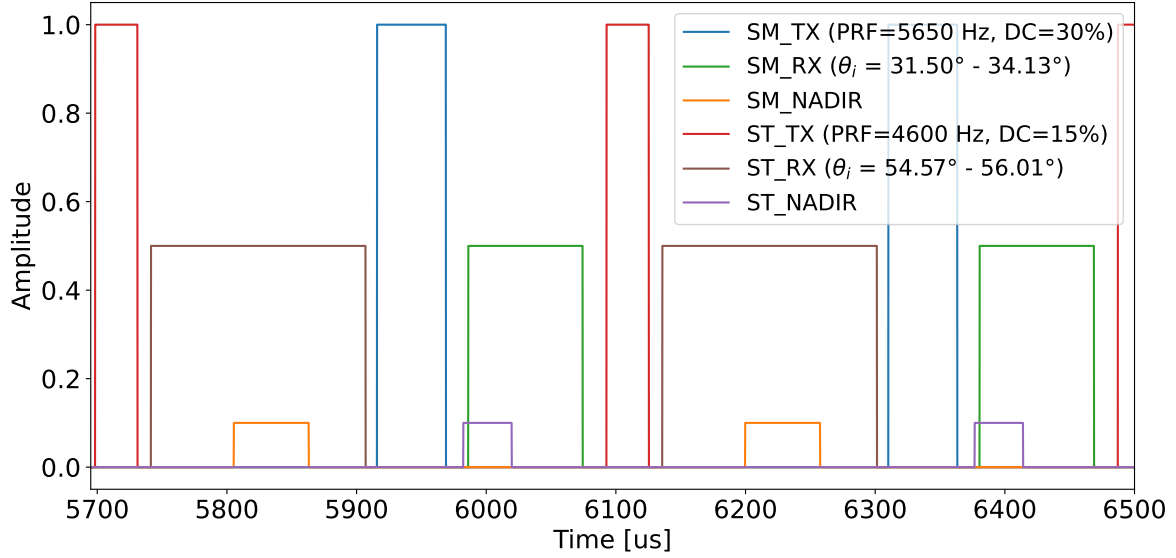


FIGURE 4.11 – Schematic amplitude representation of the events of a concurrent acquisition in time. The targets are 330 km apart.

Due to the special frequency behavior of F-Scan acquisitions, it is also of great interest to visualize the events in the frequency domain, as in Fig. 4.12.

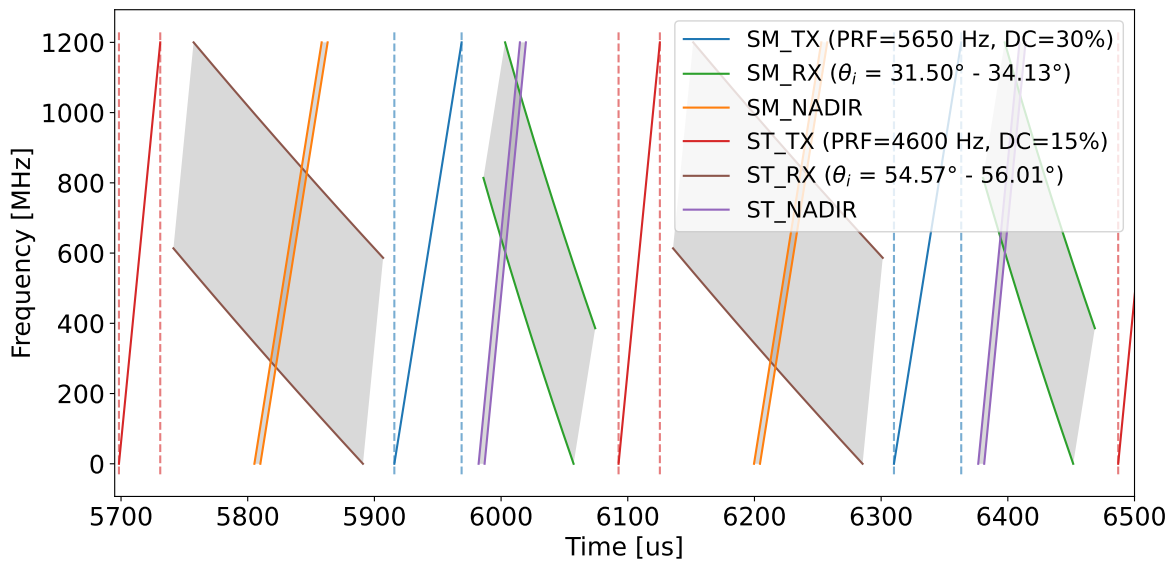


FIGURE 4.12 – Schematic frequency representation of the events of a concurrent acquisition in time. The targets are 330 km apart.

The transmit pulses considered are simply FM linear up-chirps. Consequently, the Nadir echoes are also linear chirps, but with a certain width/duration as a 3° area is considered, as explained in Section 2.2. The received echoes are obtained the same way as described for Figs. 4.8 and 4.9.

An important consideration here is that the prefixes SM (Stripmap) and ST (Staring Spotlight) are used to differentiate the two images. However, the timing analysis is performed exclusively in elevation/range, while the differentiation between these two modes are mainly in azimuth. Therefore, in this part of the analysis, if two Stripmap images or one Stripmap and one Spotlight images are being acquired is irrelevant, as both options are equivalent from a timing perspective. When investigating deeper the antenna modeling or the imaging performance, the modes employed must be well defined.

4.2.3 Interference Assessment

The interference analysis is typically performed in the time by amplitude domain, as introduced in Section 2.2. With the F-Scan, however, an amplitude inspection is insufficient. The interference assessment whenever the F-Scan is involved must be done in the time by frequency domain.

For instance, if Fig. 4.11 depicted a traditional concurrent acquisition (instead of an F-Scan one), it could be concluded that there is no interference between ST Nadir and SM reception, as the Nadir would be focused outside the image. Observing the behavior in frequency as depicted in Fig. 4.12, however, one immediately concludes that there is cross-interference between the ST Nadir and the SM reception. Therefore, to avoid Nadir interference, it must be ensured that the Nadir echoes do not intersect the reception in the time by frequency domain.

Once in the concurrent mode different pulses are transmitted towards each of the scenes, it is important to differentiate when the Nadir interference occurs within the same mode, or between different modes. The reason for this differentiation is that non-identical independent transmit pulses can be used in each mode, enabling the possibility to diminish or even remove the Nadir cross-interference by proper waveform selection. For instance, Villano suggested in (VILLANO; KRIEGER; MOREIRA, 2018) a dual-focus post-processing technique that enables the removal of the Nadir echo by making use of waveform diversity. Alternatively, OFDM as described in Section 3.3 would provide orthogonality, and, therefore, separability between the cross-nadir and the useful echoes, allowing ultimately the removal of the Nadir echoes.

An in-depth investigation of the possibilities and the effects of the techniques that enable the removal of the Nadir cross-interference when using F-Scan is envisaged for

future work. It is a long topic that deserves thorough analyses, and it is not the focus of this research. Nevertheless, once possibilities to remove the Nadir cross-interference have already been introduced in the literature, this sort of interference is considered as acceptable. In other words, only Nadir interference within the same mode is considered as harmful and unavoidable, blocking the use of the respective PRFs.

Concerning the transmit interference, the F-Scan does not change its behavior compared to nominal Stripmap. As described in Section 2.2, one must simply ensure that the received echoes do not overlap with the transmit pulses. From the timing analysis, in conclusion, one can derive the interferences involved to decide if a pair of PRFs can be used in a specific acquisition.

Due to an extra degree of freedom originated from adjusting two PRFs, visualizations as in Fig. 2.3 are no longer possible. However, usually the first step when ordering or designing an acquisition is defining the targets. Given the satellite orbit, one can obtain all the flyovers, and then derive the possible incidence angles for the acquisition. The timing diagram can be adapted so that each axis represents the PRF of one of the modes. For the same targets and parameters as in Fig. 4.11, the adapted timing diagram is presented in Fig. 4.13.

The plots depict the interference events for a range of PRF combinations. Apart from transmit and Nadir interference, the plots also highlight the PRFs that are too high and lead to insufficient echo window (light gray). This is determined simply by checking if the sum of the total echo windows and the transmit pulses is shorter than the effective PRI. Moreover, the PRFs that are too low – effective PRF below 2000 Hz – and lead to insufficient sampling are also highlighted (dark gray). It will be shown in the next sections that these PRFs lead to poor azimuth performance.

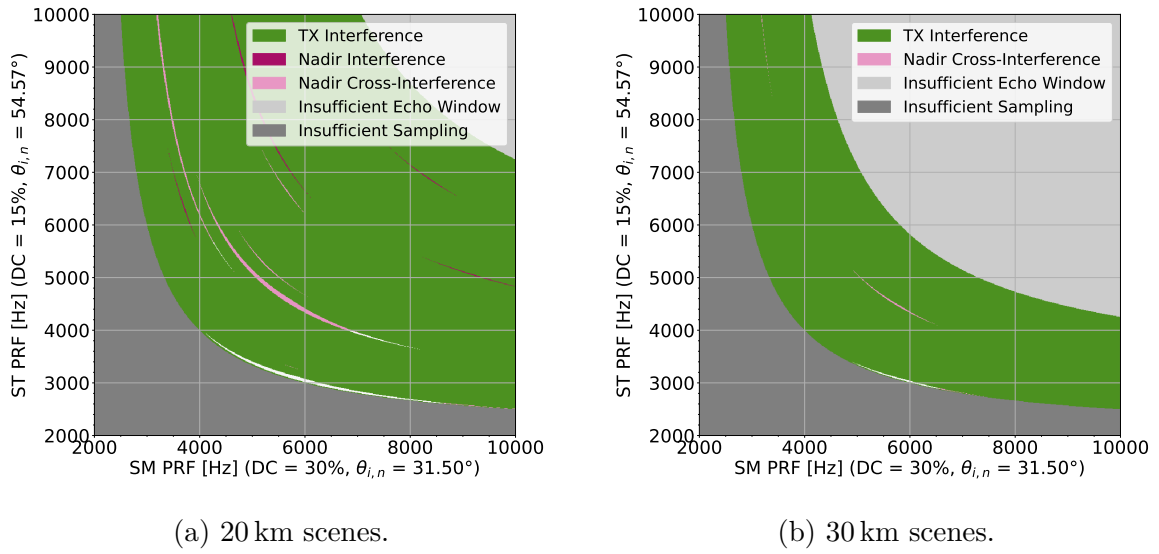


FIGURE 4.13 – Interference matrices for concurrent acquisitions with F-Scan portraying the available PRF combinations and the interference events. The allowed areas are indicated by the white and pink colors. On the left two scenes with 20 km of swath width are considered, while on the right the swaths are increased to 30 km.

From Fig. 4.13 one can derive the PRFs that will lead to a possible acquisition from a timing point of view. As Nadir cross-interference are considered as acceptable, the areas in pink and in white represent the good PRF combinations. Naturally, different acquisition scenarios (incidence angles, duty cycle, scene sizes, satellite height, etc) lead to different interference matrices.

It is expected and observable by comparing Figs. 4.13a and 4.13b that increasing the required swath width reduces the PRF availability. As the scenes get broader, the required total echo windows increase, leading to a lower maximum effective PRF and a bigger light gray area. A similar effect occurs to transmit interferences, where some PRFs are no longer available as they now lead to an overlap between transmission and reception. Even with a visibly lower PRF availability in Fig. 4.13b, there are still some rather small regions in pink and white which enable an acquisition. For instance, the PRFs depicted in Fig. 4.11 are within the pink area of Fig. 4.13b.

At this point of the analysis the timing and interference assessments are already well defined. However, observing, for instance, Fig. 4.12 one can still visualize some unused time, in which the radar is not transmitting nor receiving. This sort of inefficiency originates from various causes. To list a couple, the effective PRF may be far from the maximum PRF (light gray area), or maybe the duty cycles are too low. A better simulation would be to vary both duty cycles and both PRFs, but this excess of variables and possibilities would make the processing impracticable from a computational time point of view.

To simplify the PRF and duty cycle determination, one can first define a minimum duty cycle, such as 15 %, and select the desirable PRFs considering not only the timings as described in this section, but also the ambiguities as will be discussed in the next sections. Then, the duty cycles may be steadily increased checking for interferences. For the same acquisition as in Fig. 4.12, this duty cycle variation leads to the interference plot depicted in Fig. 4.14.

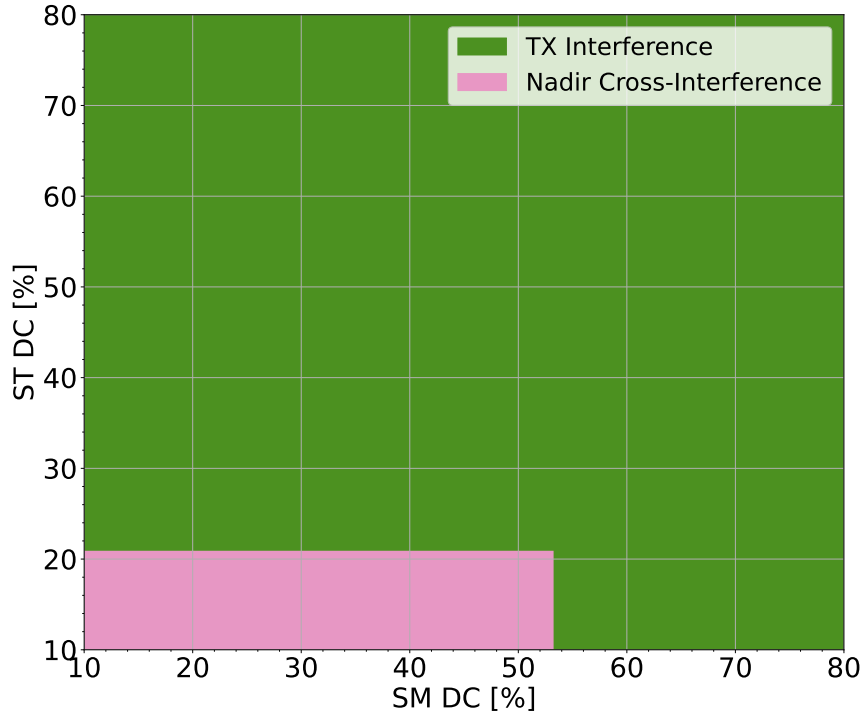


FIGURE 4.14 – Interference events achieved by varying the duty cycles of each mode. The scenes have a swath width of 30 km, near range incidence angles of 31.50° and 54.57° , and the PRFs used are 5650 Hz and 4600 Hz.

To visualize the results of optimizing the duty cycles, Fig. 4.15 shows the acquisition with duty cycles of 53 % (SM) and 21 % (ST). Even though duty cycles higher than 30 % are not envisaged, the key point here is the possibility of increasing the duty cycle without any trade-offs in terms of PRF and scene size. This duty cycle maximization, actually, is desirable, as it increases the SNR, and, consequently, and the image quality.

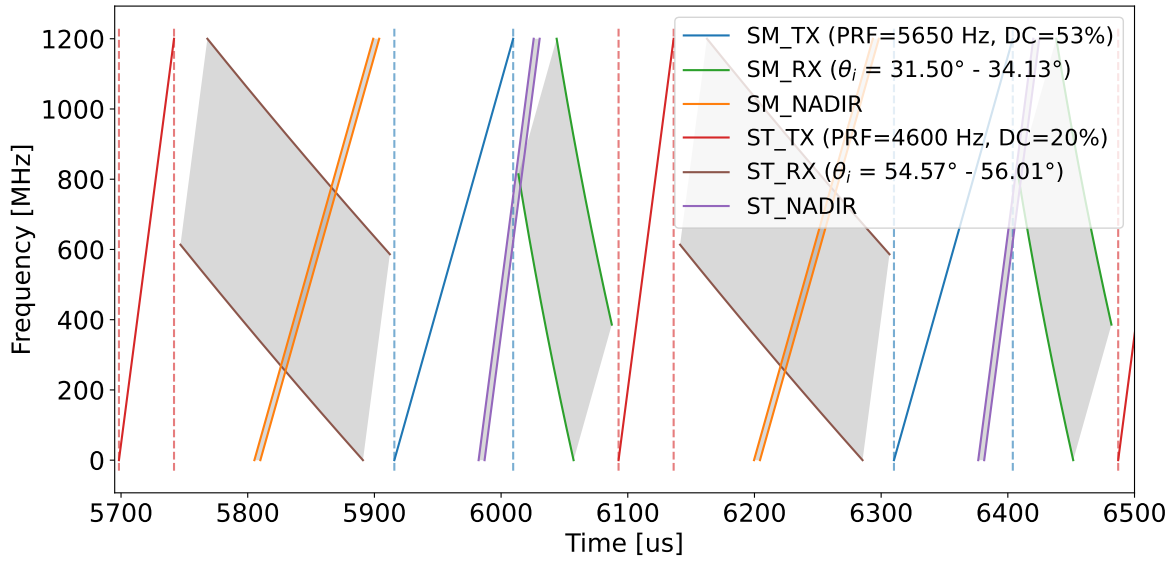


FIGURE 4.15 – Schematic frequency representation of the events of a concurrent acquisition in time. The duty cycles have been maximized to improve the efficiency of the time domain usage.

Finally, it is important to highlight that the plots presented in this section, which are related to a specific acquisition, are for mere explanation of the timing analysis steps. Actually, this investigation is valid for any set of acquisition inputs (e.g. incidence angles, swath widths, minimum duty cycles, etc). Chapter 5 will expand this analysis to a multitude of scenarios.

4.3 Antenna Modeling

The antenna considered in this work was briefly described in Section 4.1. Due to the necessity of calculating ambiguities, and the special behavior of the F-Scan, a more detailed analysis is required. This section aims at describing the characteristics of the antenna that are relevant to support and understand the design of the concurrent mode with F-Scan.

The antenna consists of an array of individual elements aligned in a two dimensional rectangular grid. Within a size of 1.4 m by 6.0 m, the antenna is endowed with 64 by 12 elements in elevation and azimuth, respectively. A special characteristic of this sort of arrangement is the relative independence of each of the axes. For instance, to determine the antenna patterns, one can simply consider two one-dimensional linear arrays (BACHMANN, 2015). In azimuth and elevation, therefore, the angles α_{ant} and β_{ant} are used to define the antenna pattern in each of the directions. Figure 4.16 schematically depicts the antenna described and the angles of interest.

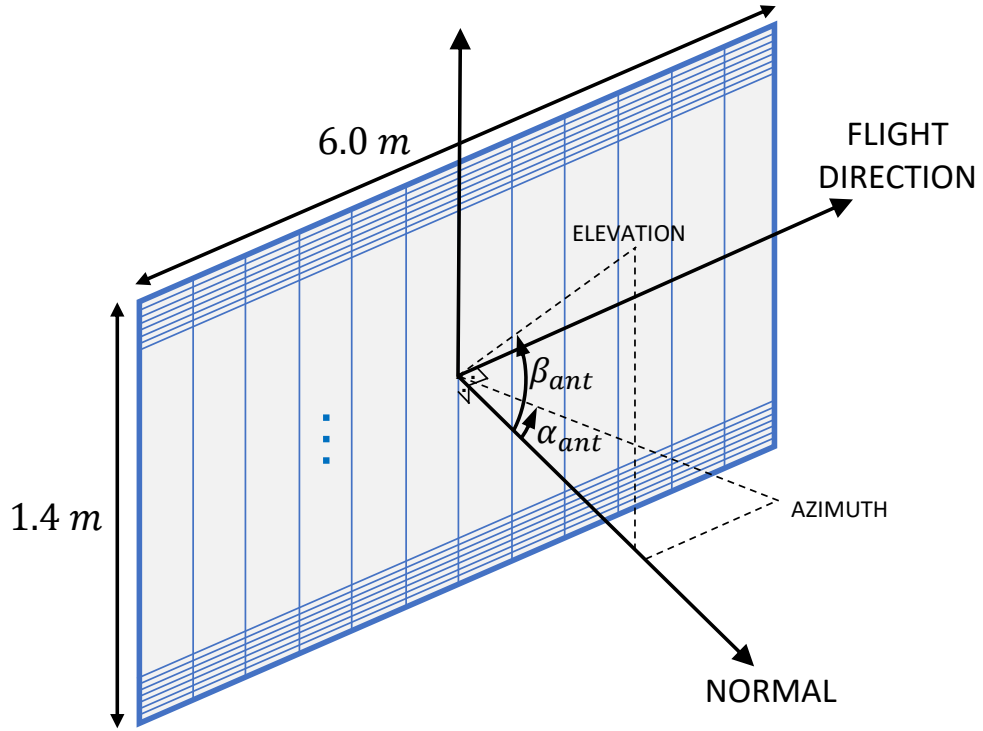


FIGURE 4.16 – Schematic representation of the antenna considered in this thesis.

4.3.1 Azimuth

Once each direction can be analyzed separately, let us take a look into the azimuth direction first, as it represents the traditional and well-known phased-array modeling. First, the array is assumed to be comprised of N individual elements, such that the element i is fed with an amplitude A_i and a phase $(i - 1)\delta$ (phase increment of δ). Figure 4.17 summarizes the linear antenna array considered. Due to the principle of superposition, the antenna electromagnetic far field is given simply by the sum of the individual fields of the elements.

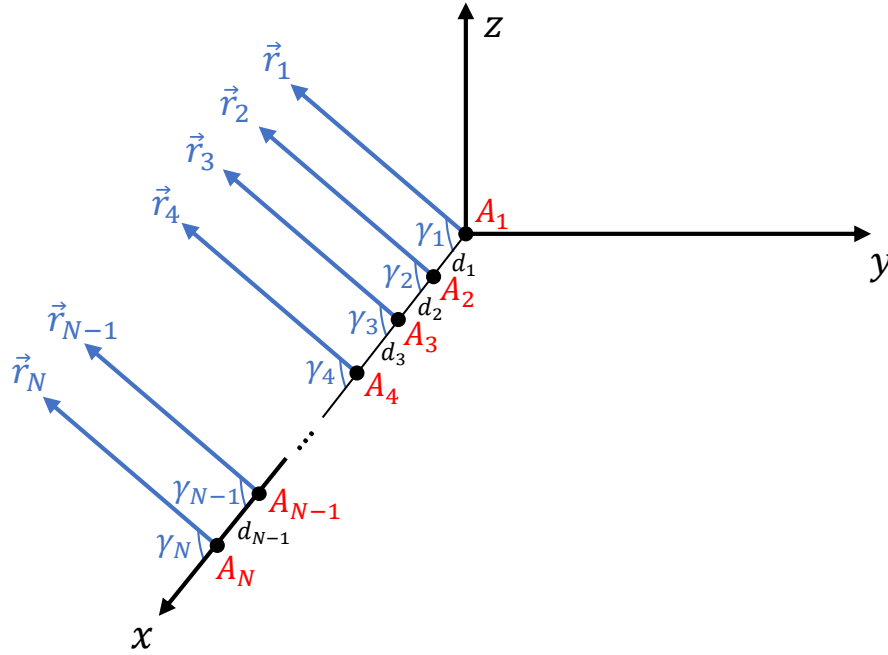


FIGURE 4.17 – Linear phased-array considered to derive the antenna patterns.

The electric far field for an uniformly distributed array ($d_i = d$) can be mathematically written as

$$\vec{E}(\alpha_{ant}, \beta_{ant}) = K \cdot \vec{g}(\alpha_{ant}, \beta_{ant}) \cdot \frac{e^{-jk_0 r}}{r} \cdot \sum_{i=1}^N A_i \cdot e^{j(i-1)\psi}, \quad (4.18)$$

such that K is a constant of proportionality, \vec{g} the element factor, $k_0 = 2\pi/\lambda$ the wave number, $\psi = k_0 d \cos \gamma + \delta$, with $\gamma_i = \gamma$ the angle between the irradiation direction and the antenna array (BALANIS, 2016). Assuming an uniform current distribution and the element to be a slotted waveguide with a radiation pattern in azimuth ($\beta_{ant} = 0$, or xz plane) given by

$$|\vec{g}(\alpha_{ant})| = \left| \frac{\sin(x(\alpha_{ant}))}{x(\alpha_{ant})} \right|, \quad (4.19)$$

with

$$x(\alpha_{ant}) = \frac{\pi \cdot d \cdot \sin(\alpha_{ant})}{\lambda}, \quad (4.20)$$

the magnitude of the electric field in azimuth can be rewritten as

$$|\vec{E}(\alpha_{ant})| = A \cdot |K| \cdot \left| \frac{\sin(x(\alpha_{ant}))}{x(\alpha_{ant})} \right| \cdot \frac{1}{r} \cdot \left| \sum_{i=1}^N e^{j(i-1)\psi} \right|. \quad (4.21)$$

The last factor can be expanded as

$$\sum_{i=1}^N e^{j(i-1)\psi} = 1 + e^{j\psi} + e^{j2\psi} + \dots + e^{j(N-1)\psi} = \frac{1 - e^{jN\psi}}{1 - e^{j\psi}}, \quad (4.22)$$

leading to

$$\sum_{i=1}^N e^{j(i-1)\psi} = \frac{e^{jN\psi/2}}{e^{j\psi/2}} \left(\frac{e^{-jN\psi/2} - e^{jN\psi/2}}{e^{-j\psi/2} - e^{j\psi/2}} \right) = e^{j(N-1)\psi/2} \cdot \left(\frac{\sin\left(\frac{N\psi}{2}\right)}{\sin\left(\frac{\psi}{2}\right)} \right) \quad (4.23)$$

$$\left| \sum_{i=1}^N e^{j(i-1)\psi} \right| = \left| \frac{\sin\left(\frac{N\psi}{2}\right)}{\sin\left(\frac{\psi}{2}\right)} \right|. \quad (4.24)$$

The electric field pattern in azimuth is then given by

$$|\vec{e}(\alpha_{ant})| = \left| \frac{\vec{E}}{\vec{E}_{max}} \right| = \underbrace{\left| \frac{\sin(x(\alpha_{ant}))}{x(\alpha_{ant})} \right|}_{\text{Element Factor}} \cdot \underbrace{\left| \frac{\sin\left(\frac{N\psi}{2}\right)}{N \cdot \sin\left(\frac{\psi}{2}\right)} \right|}_{\text{Array Factor}}. \quad (4.25)$$

The antenna pointing is obtained by the direction α_{ant} which leads to maximum gain. It can be adjusted by tailoring the phase δ to adjust ψ in order to maximize the array factor. By the L'Hospital's rule, the factor is maximized for $\psi = 2\pi k$, with $k \in \mathbb{Z}$. Taking $k = 0$, the phase ramp that leads to, loosely speaking, maximum gain at the azimuth angle α_{max} is

$$\delta = -k_0 d \cos \gamma_{max} \xrightarrow{\alpha_{ant} = \gamma - 90^\circ} \delta = k_0 d \sin \alpha_{max}. \quad (4.26)$$

The factor ψ is then rewritten as

$$\psi = k_0 d (\sin \alpha_{max} - \sin \alpha_{ant}). \quad (4.27)$$

It is important to observe that the term ‘loosely speaking’ was employed because the desired steering is not always achievable. Mathematically, the value obtained in (4.26) does not maximize (4.25) for every element factor and elements spacing d . For isotropic elements, i.e., unitary element factor, the pointing obtained by tailoring the array factor is indeed the direction of maximum gain. This does not necessarily hold true for the slotted waveguide element considered here in this thesis.

Another issue that arises is the periodicity observed in the possible values of ψ . The

array factor is maximized when $\psi = 2\pi k$. Therefore, it must be ensured that only one value of α_{ant} in $[-\pi/2, \pi/2]$ leads to a maximum gain scenario. Let us investigate what constraint is required to avoid these so called grating lobes. Equation (4.27) is then rewritten as

$$\begin{aligned} 2\pi k &= \frac{2\pi}{\lambda} d (\sin \alpha_{max} - \sin \alpha_{ant}) \\ k \frac{\lambda}{d} &= \sin \alpha_{max} - \sin \alpha_{ant} \\ \sin \alpha_{ant} &= \sin \alpha_{max} - k \frac{\lambda}{d} \end{aligned} \quad (4.28)$$

It is clear that for $k = 0$, $\alpha_{ant} = \alpha_{max}$ is the only solution within the interval of interest. Now, to avoid grating lobes, it must be ensured that for $k \neq 0$ there is no solution within the interval. However, it is clear that the sine of a real number is contained within 1 and -1. In other words,

$$\begin{aligned} -1 &\leq \sin \alpha_{max} \leq 1 \\ -1 &\leq \sin \alpha_{ant} + k \frac{\lambda}{d} \leq 1 \\ -1 - k \frac{\lambda}{d} &\leq \sin \alpha_{ant} \leq 1 - k \frac{\lambda}{d} \end{aligned} \quad (4.29)$$

The inequality leads to no solution if $\sin \alpha_{ant} > 1$ or $\sin \alpha_{ant} < -1$ for every k . The critical cases are $k = \pm 1$. Then, for $k = 1$, it must be ensured $1 - \frac{\lambda}{d} < -1$ and for $k = -1$, $-1 + \frac{\lambda}{d} > 1$. These redundant conditions both lead to the required condition to avoid grating lobes, which is

$$\frac{d}{\lambda} < 0.5. \quad (4.30)$$

In summary, having a element spacing lower than half the wavelength is desirable, as no grating lobes are obtained. This approach, however, is typically very expensive as a large number of elements are required, specially at higher frequencies.

Then, it is of obvious interest to check the element spacing of the system under analysis. Once the antenna size and the number of elements are known, the ratio is given by

$$\left(\frac{d}{\lambda} \right)_{Az, HRWS} = \frac{6.0 \text{ m}}{12 \cdot 0.0306 \text{ m}} = 16.3. \quad (4.31)$$

The condition to avoid grating lobes (4.30) is not being respected, and by a large factor. With $k = \pm 1$ in (4.28), the first grating lobes are already at $\pm 3.56^\circ$. In other words, many grating lobes will be present in the antenna pattern. If the elements were isotropic, the theoretical antenna pattern at boresight that would be obtained is depicted in Fig. 4.18.

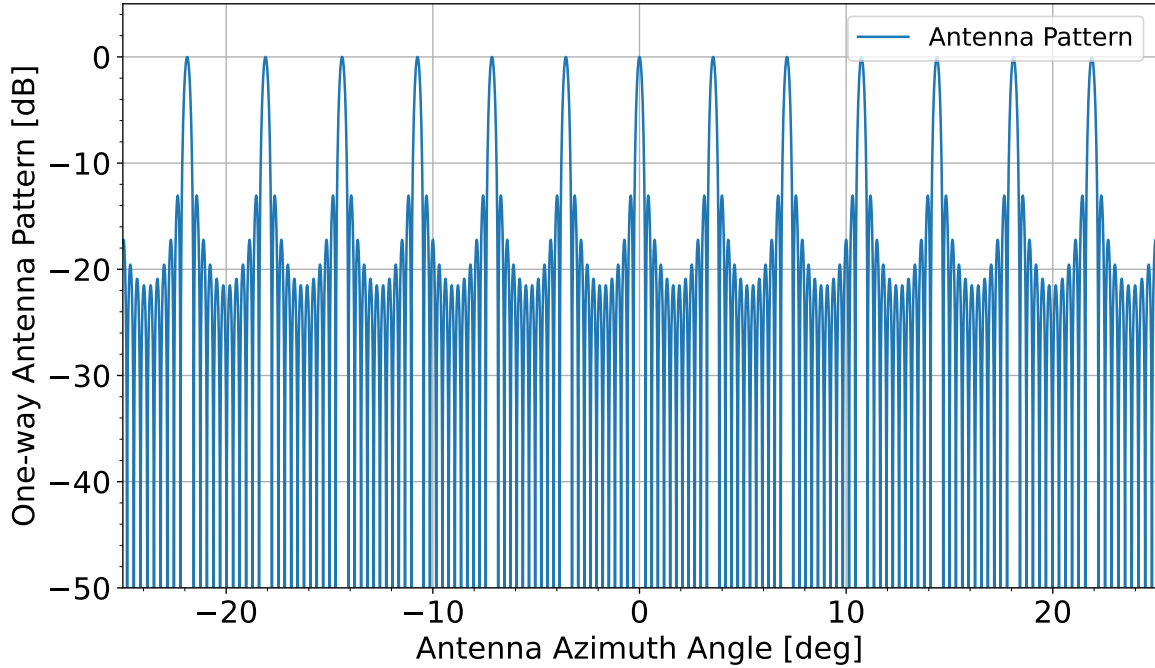


FIGURE 4.18 – Theoretical antenna pattern in azimuth if isotropic elements were considered.

However, the element factor considered is actually not isotropic. Considering not only the array factor, but also the element factor, the final result is actually a usable pattern. Figure 4.19 depicts the antenna pattern for boresight (pointing at 0°), highlighting the contribution from each of the factors. An interesting and extremely helpful behavior is observed: at $\alpha = \sin^{-1} \frac{\lambda}{d} = 3.5^\circ$, the maxima of the array factor coincide with the nulls of the element factor. This leads to a nice canceling of the grating lobes, and ultimately to an antenna pattern with much better sidelobes.

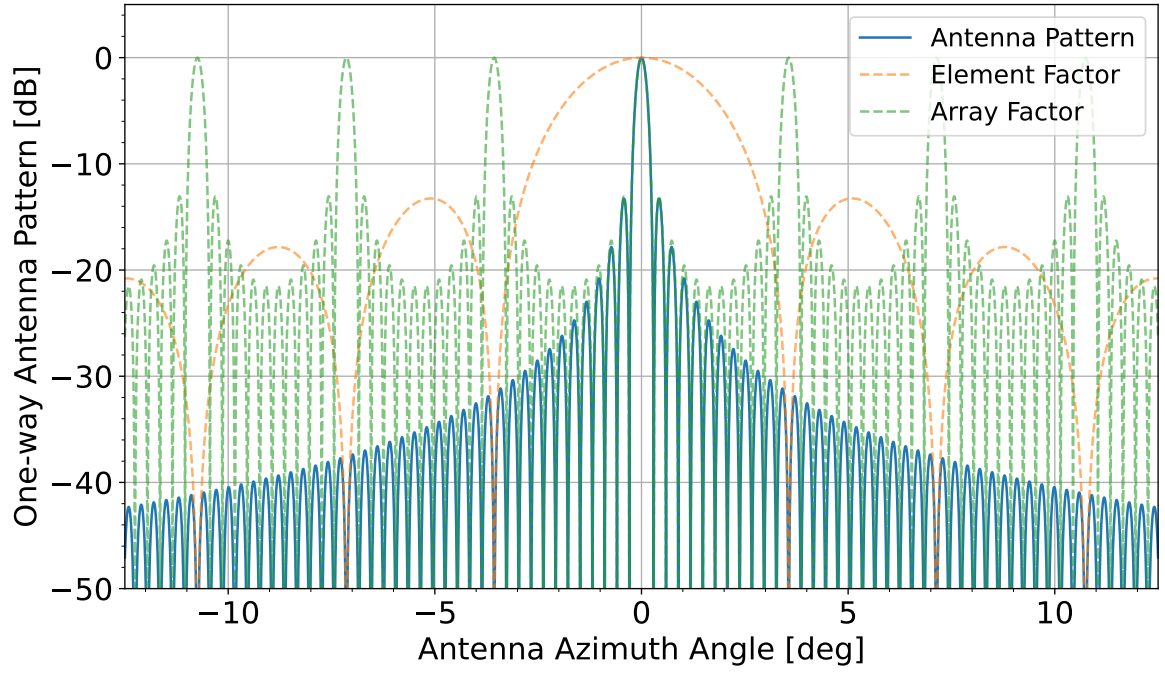


FIGURE 4.19 – Theoretical antenna pattern in azimuth at boresight.

Due to the d/λ factor of 16, the steering capabilities of this antenna in azimuth are very limited. When aiming at a pointing other than boresight by adjusting the phase ramp, the array factor is the one being adjusted. The final antenna pattern is then obtained simply by multiplying the unchanged element factor by this shifted array factor. For a steering of only $+1^\circ$, Fig. 4.20 depicts the antenna pattern obtained. A strong grating lobe is already visible.

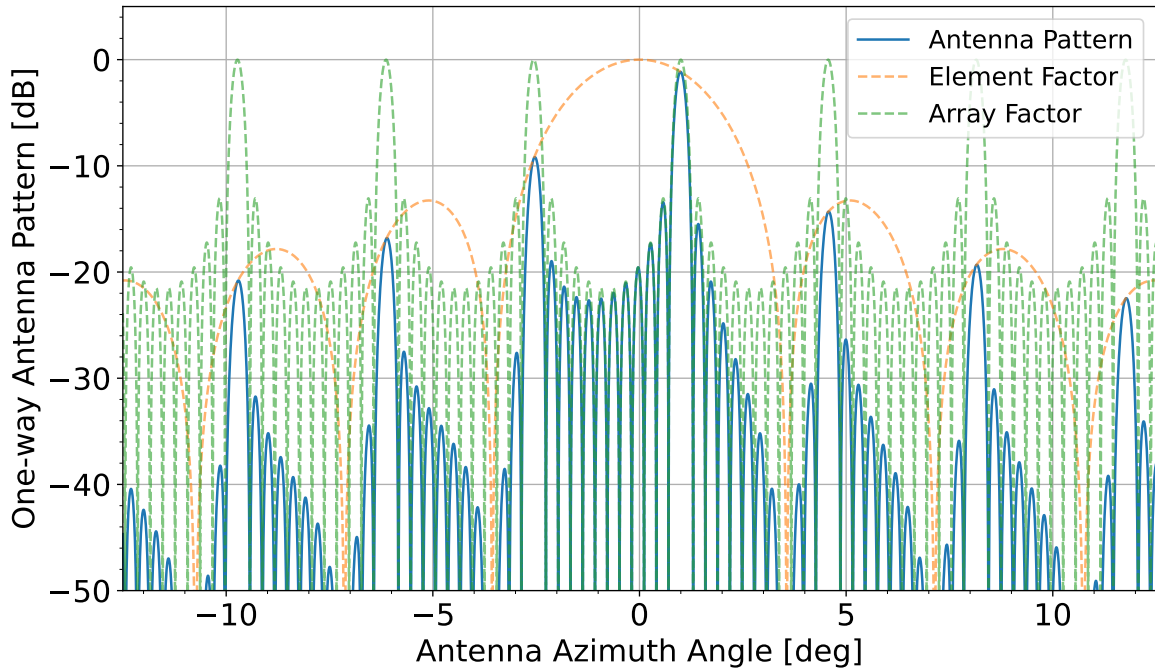


FIGURE 4.20 – Theoretical antenna pattern in azimuth for a $+1^\circ$ steering.

Steering in the azimuth direction is of great interest in some imaging modes. For instance, the Staring Spotlight mode as introduced in (MITTERMAYER *et al.*, 2014) requires a steering of 2.2° . If this sort of steering were attempted with the antenna described in this thesis, the image quality – more specifically the azimuth ambiguity-to-signal ratio – would be strongly degraded by the grating lobes.

To overcome this limited steering capabilities, the antenna would either need to be smaller or have more elements. Naturally, each of these ideas come with its own trade-offs. Reducing the antenna size would lead to broader beams and lower gains, deteriorating the SNR. On the other hand, adding elements would maintain the gain and reduce the grating lobes, but increase the total cost of the system. In summary, the antenna steering is quite limited with the antenna envisaged for the upcoming HRWS system. If higher steering angles are desirable, the system will likely need to rely on mechanical steering of the platform. Therefore, concurrent Stripmap with Spotlight imaging modes must be discarded in this investigation, as the Spotlight performance would be insufficient with the limited steering. Finally, this thesis will focus on simultaneous Stripmap imaging, aiming at maximizing the swath width while achieving good resolution and image quality.

4.3.2 Elevation

The antenna in elevation is also a phased-array with similar element pattern as in azimuth. However, the antenna is not only shorter, but also has a higher number of

elements. Therefore, it suffers much less from grating lobes than the antenna in azimuth. Its spacing factor is

$$\frac{d}{\lambda} = \frac{1.4 \text{ m}}{64 \cdot 0.0306 \text{ m}} = 0.715. \quad (4.32)$$

From (4.28) and (4.32), grating lobes only start to appear in the antenna pattern for steering angles higher than 25° . Assuming that the satellite is rolled by 33.8° – antenna boresight pointing at a look angle of 33.8° – grating lobes only appear for look angles lower than 8.8° (incidence angle of 9.5°) and higher than 58.8° (incidence angle of 67.6°). These regions, however, are beyond the desired look angle range of interest, as the image quality is strongly deteriorated (layover, foreshortening, shadows, lack of resolution, etc).

In elevation, therefore, it is clear that the antenna does not suffer from grating lobes. This is considered by design as steering in elevation for a SAR system is mandatory. It is clear that a fixed look angle would not provide enough imaging flexibility. Steering in elevation is even more important for a system aiming at using the F-Scan technique, which intrinsically requires steering capabilities.

The phase ramp required to achieve an arbitrary pointing was obtained in (4.26). For a fixed phase ramp, the equation shows a direct dependency of the frequency and the steering. This is the origin of the frequency scanning, reaching different pointing angles for different frequencies. For small steering angles, the relation between wavelength and angle is visibly linear.

The frequency scanning requires not only the pointing, but also a specific sweeping. In other words, it is necessary to define the pointing not only for one frequency, but for both the minimum and maximum frequencies. These two requirements cannot be achieved simply by adjusting the phase ramp. Therefore, one extra degree of freedom is required.

In (ROEMER, 2017), Roemer suggests the use of not only the phase shifters, but also of true time delay lines (TTDL). Moreover, not every element requires its dedicated TTDL, actually several adjacent elements can share one TTDL. The time delay is in the order of picoseconds, and is here represented by the symbol $\Delta\tau$. It was shown that this extra degree of freedom allows for an independent control of the beam dispersion (sweeping) and the beam pointing direction. The antenna pointing is then expressed by

$$\sin \beta_{ant} = \frac{c_0}{d} \left(\frac{\delta}{2\pi f} - \Delta\tau \right). \quad (4.33)$$

Equation (4.33) highlights the role of the phase shifters and of the TTDLs in the beam pointing. Clearly, the phase shift is the frequency dependent factor, while the time delay is not. So, in short, the TTDLs define the pointing of the beam, and the phase shifters

define the total scanning as the frequency varies.

For the up-chirps as described in Section 4.2, the antenna must point towards the far range look angle β_f ($\beta_{ant,f}$ in the antenna coordinate system) with the minimum frequency $f_{min} = 9.2$ GHz. The transmission ends when the antenna is pointing towards the near range look angle β_n ($\beta_{ant,n}$ in the antenna coordinate system) with the maximum frequency $f_{max} = 10.4$ GHz. These two relations together with (4.33) lead to a simple system of equations with two equations and two variables. Solving for δ and $\Delta\tau$, the phase ramp and the time delay for any arbitrary scan are given by

$$\left\{ \begin{array}{l} \delta = \frac{2\pi d}{c_0} \frac{(\sin \beta_{ant,f} - \sin \beta_{ant,n})}{\frac{1}{f_{min}} - \frac{1}{f_{max}}} \\ \Delta\tau = \frac{d}{c_0} \left(\frac{f_{min} \cdot \sin \beta_{ant,f} - f_{max} \cdot \sin \beta_{ant,n}}{f_{max} - f_{min}} \right) \end{array} \right. \quad (4.34a)$$

$$\left\{ \begin{array}{l} \delta = \frac{2\pi d}{c_0} \frac{(\sin \beta_{ant,f} - \sin \beta_{ant,n})}{\frac{1}{f_{min}} - \frac{1}{f_{max}}} \\ \Delta\tau = \frac{d}{c_0} \left(\frac{f_{min} \cdot \sin \beta_{ant,f} - f_{max} \cdot \sin \beta_{ant,n}}{f_{max} - f_{min}} \right) \end{array} \right. \quad (4.34b)$$

For instance, let us visualize two different scenarios. First, the antenna is sweeping from $+2^\circ$ to -2° . This leads to a phase ramp of 147.0° and a time delay of 41.8 ps. On a second scenario, where the antenna scans from $+16^\circ$ to $+10^\circ$, the obtained phase shift is 214.8° and the time delay is 44.6 ps. Using the values obtained and replacing in (4.33), the pointing for every frequency within the bandwidth can be obtained. The antenna pointing angle versus the instantaneous frequency plot for each of the described scenarios is depicted in Fig. 4.21.

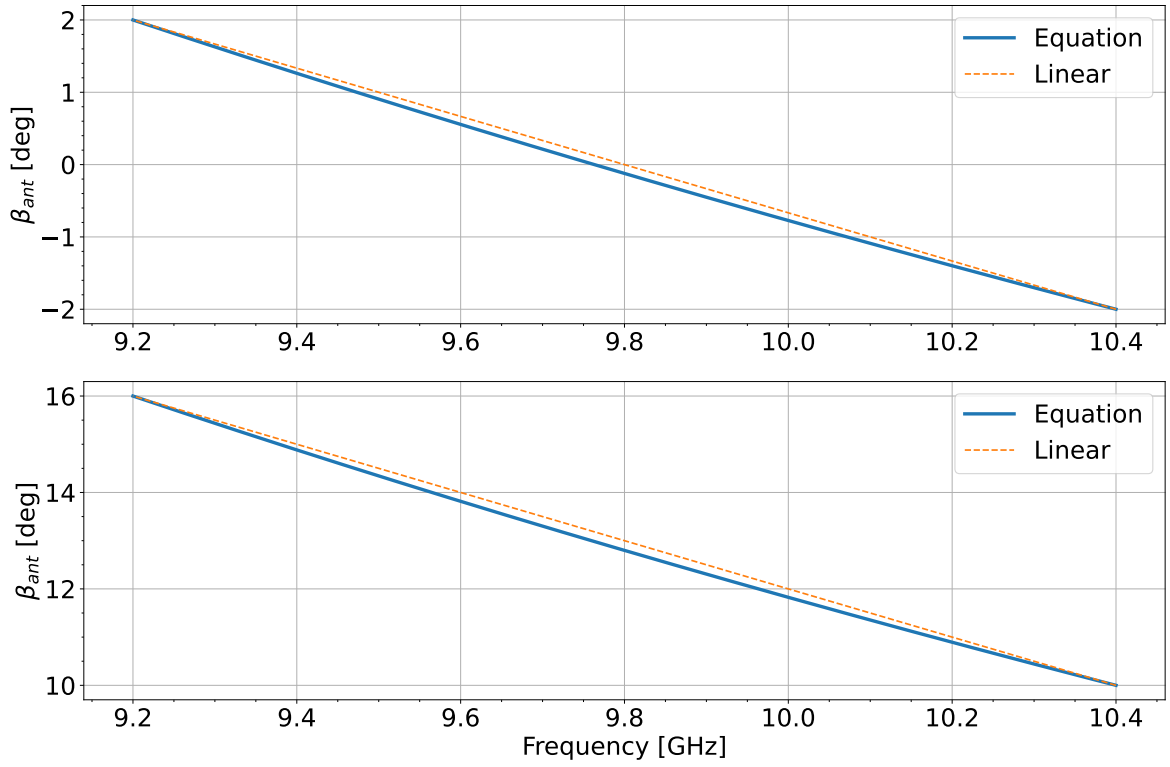


FIGURE 4.21 – Frequency scanning for two arbitrary scenarios. On the upper plot, the antenna is sweeping from the look angles 35.8° to 31.8° . On the lower plot, the scan is from 49.8° to 43.8° . The plot highlights the nearly linear frequency scanning.

The pointing obtained by the equation is in blue, while the perfectly linear scanning is in orange. The objective of the plot is to highlight how close to linear the scanning is, justifying, therefore, the assumption of linearity made in Section 4.2.

Even though the extra time delay was introduced, the antenna pattern in elevation can still be obtained by (4.25). The main difference now is an extra phase shift given by $\omega\Delta\tau$. So, as a matter of antenna pattern generation, an equivalent δ' is sufficient. For the center frequency of 9.8 GHz and a pointing of 15° , Fig. 4.22 depicts the antenna pattern obtained in elevation. It can be seen that due to the elements being small, the element factor in elevation is much closer to an isotropic radiator than in azimuth. Moreover, with a steering lower than the 25° previously calculated, no grating lobes are observed.

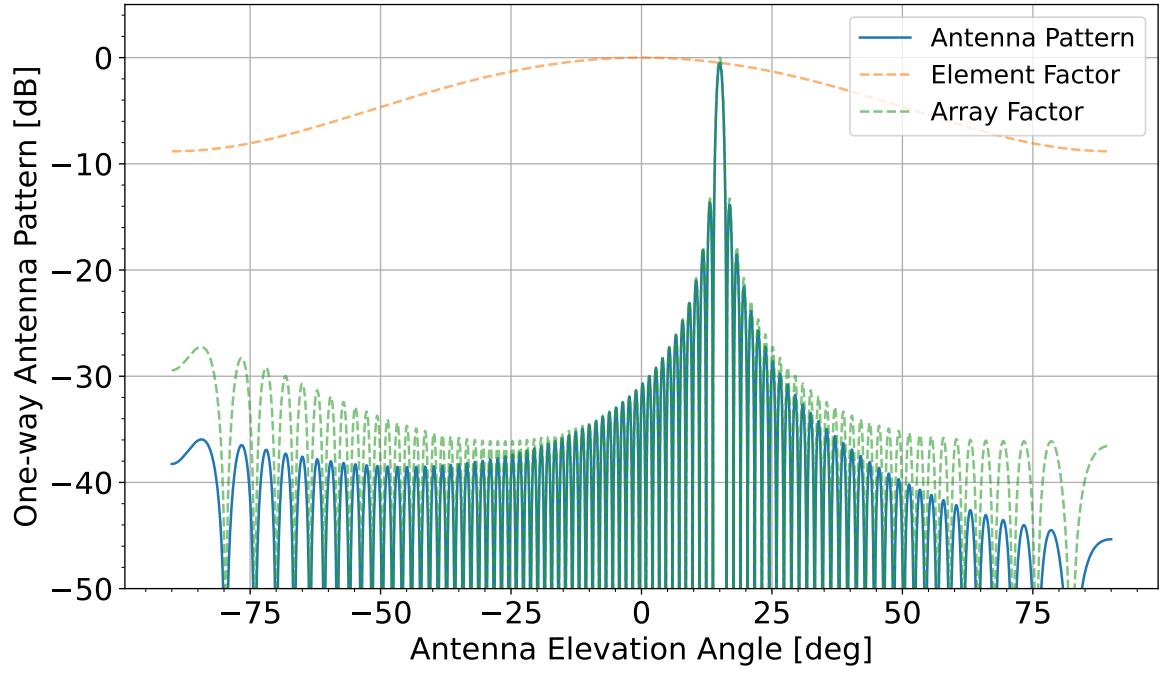


FIGURE 4.22 – Theoretical antenna pattern in elevation for a steering of 15° and a frequency of 9.8 GHz.

As a matter of simplification, the center frequency of 9.8 GHz is considered in the most part of the analysis in range/elevation. It is clear that the antenna pattern, more specifically the half power beamwidth, does change with frequency, as shown in

$$\text{HPBW} = \frac{0.886 \cdot \lambda}{N \cdot d \cdot \cos \beta}. \quad (4.35)$$

However, the maximum wavelength error relative to the center wavelength is relatively small (about 6%), so that the center frequency is a good representative for initial performance assessments. For visualization of the tiny differences, the antenna pattern scanning in frequency is shown for a sweeping from $+3^\circ$ to -3° in Fig. 4.23.

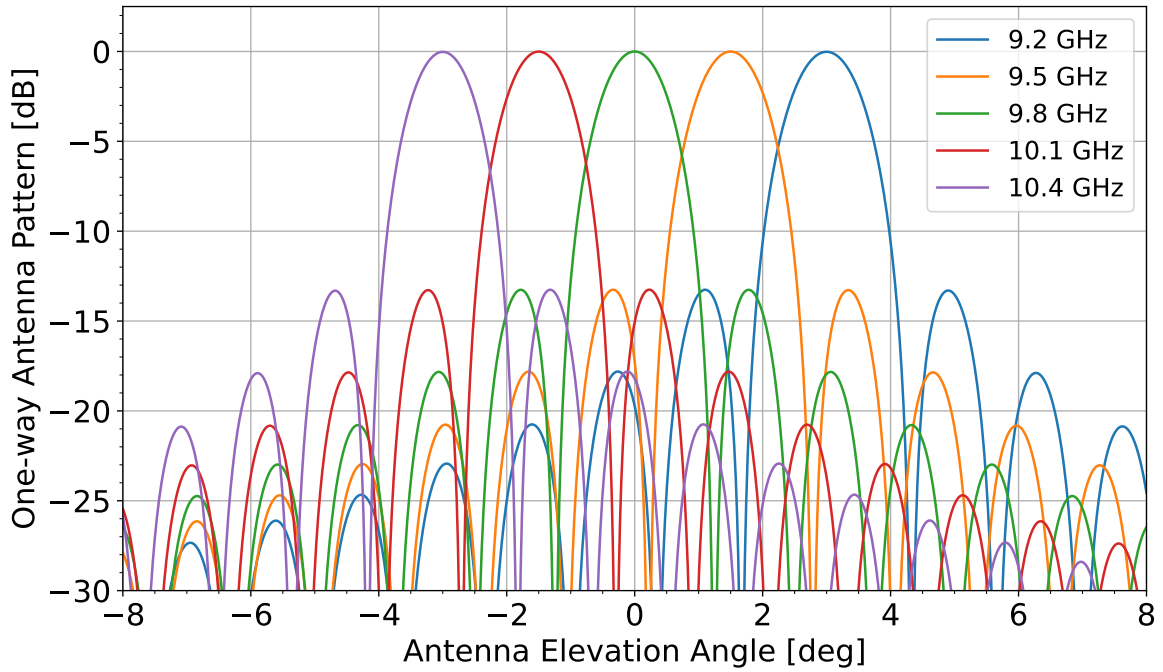


FIGURE 4.23 – Theoretical antenna frequency scanning in elevation for a sweeping from $+3^\circ$ to -3° .

4.4 Concurrent F-Scan Ambiguity Calculations

From the timing and interference assessments, the PRFs that are suitable for any specific concurrent F-Scan acquisition are known. Moreover, the antenna patterns both in azimuth and elevation are also already well determined. With this information linked to the satellite orbit and attitude, finally performance investigations can be performed. The main concerns that were observed in concurrent imaging acquisitions were image degradation due to strong ambiguities, and lack of availability for nominal swath widths (KRAUS *et al.*, 2022). This section aims at discussing the behavior of ambiguities when the F-Scan technique is considered for concurrent acquisitions.

4.4.1 Azimuth Ambiguities

The F-Scan is a technique in elevation, so that the ambiguities calculation in azimuth is not affected by it. On the other hand, the concurrent aspect does influence the azimuth performance. As introduced in Section 2.3, because two images are being simultaneously generated, and sharing the sampling, the effective sampling rate (PRF) must be considered in the azimuth analysis.

With an longer antenna of 6.0 m, in comparison to the 4.8 m of TerraSAR-X, it is clear

that the maximum azimuth resolution is degraded for single-channel Stripmap acquisitions due to the lower half power beamwidth. On the bright side, it allows for the use of lower PRFs with a better ambiguity performance in azimuth. Lowering the PRF leads then to longer echo windows and larger swaths. The loss in azimuth resolution can be compensated, if required, by the DPCA technique.

As Spotlight imaging has shown not to be of interest in concurrent acquisitions due to the lack of electronic steering capabilities (see subsection 4.3.1), the ambiguity analysis here focuses on Stripmap acquisitions. For the 6.0 m antenna with 12 elements previously described, the Stripmap azimuth ambiguity-to-signal ratio is depicted in Fig. 4.24.

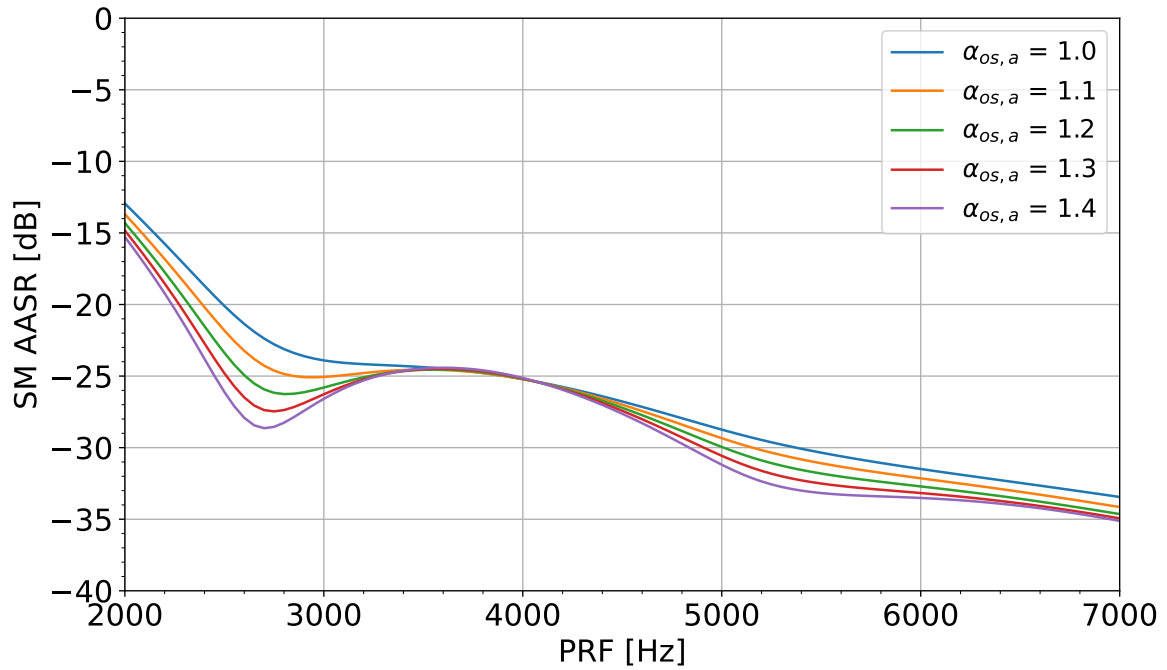


FIGURE 4.24 – Azimuth ambiguity-to-signal ratio for Stripmap acquisitions with a 6.0 m phased-array antenna with 12 elements. A Hamming window with $\alpha = 0.6$ and multiple oversampling factors ($\alpha_{os,a}$) are considered.

Comparing to Fig. 2.13, a gain of approximately 5 dB is achieved at the lower PRF range. This improvement is sufficient to enable the use of the lower PRF range. Previously the minimum PRF was limited to 2500 Hz, but now it can be extended to 2000 Hz. It is important to notice that this value is only a hard limit. In real scenarios, the effective PRF will be shown in the next chapter to be mostly concentrated between 2500 Hz and 3000 Hz.

4.4.2 Range Ambiguities

The azimuth ambiguities assessment with concurrent F-Scan was shown not to be much different than for traditional SAR imaging. The assessment in range, however, changes quite a lot. It must be stated that the origin of the ambiguities is still the same, i.e., spurious and desired echoes arriving at the antenna concomitantly. Nevertheless, both the concurrent and the F-Scan aspects lead to some specificities that change the range ambiguity-to-signal ratio analysis.

First, the concurrent imaging aspect implies the use of different antenna patterns in elevation for each mode/target area. The patterns point at targets which are usually very distant to each other (100 km or more), so that they cannot be approximated to be the same. As a consequence, two sorts of ambiguities appear: those spurious echoes that are transmitted and received with the same antenna pattern – named as same mode ambiguities –, and those echoes that are transmitted and received with different antenna patterns – named as cross-ambiguities. Moreover, the flexibility of having two different PRFs and duty cycles for each mode also shifts the positions of the ambiguities.

Concerning the F-Scan, it implies that each point-target on Earth is not imaged by a static (invariant in frequency) antenna pattern, but by a sweeping one. Therefore, the assessment of the target echoes power and the ambiguities power is not as straightforward as in traditional imaging, where the antenna pattern in elevation is static for each point-target. The approaches to consider each of these nuances in the range ambiguity assessment are described in this subsection. Numerical results for an exemplary acquisition are also presented.

So as to visualize the ambiguity positions in a variable PRF and duty cycle scenario with F-Scan, a time by frequency plot similar to the one presented in Fig. 4.12 is of great help. For this purpose, let us assume an acquisition with two arbitrary modes named here as SM and ST. The objective is to understand and determine where the ambiguities for a given point-target within one of the scenes are coming from. Assuming a point target A imaged with a center frequency f_A by the SM mode, a simplified timing plot for this acquisition is presented in Fig. 4.25. The plot is not highlighting the ST received echoes nor the rest of the SM targets as this data is not relevant to the desired objective of determining the ambiguity positions for the target A .

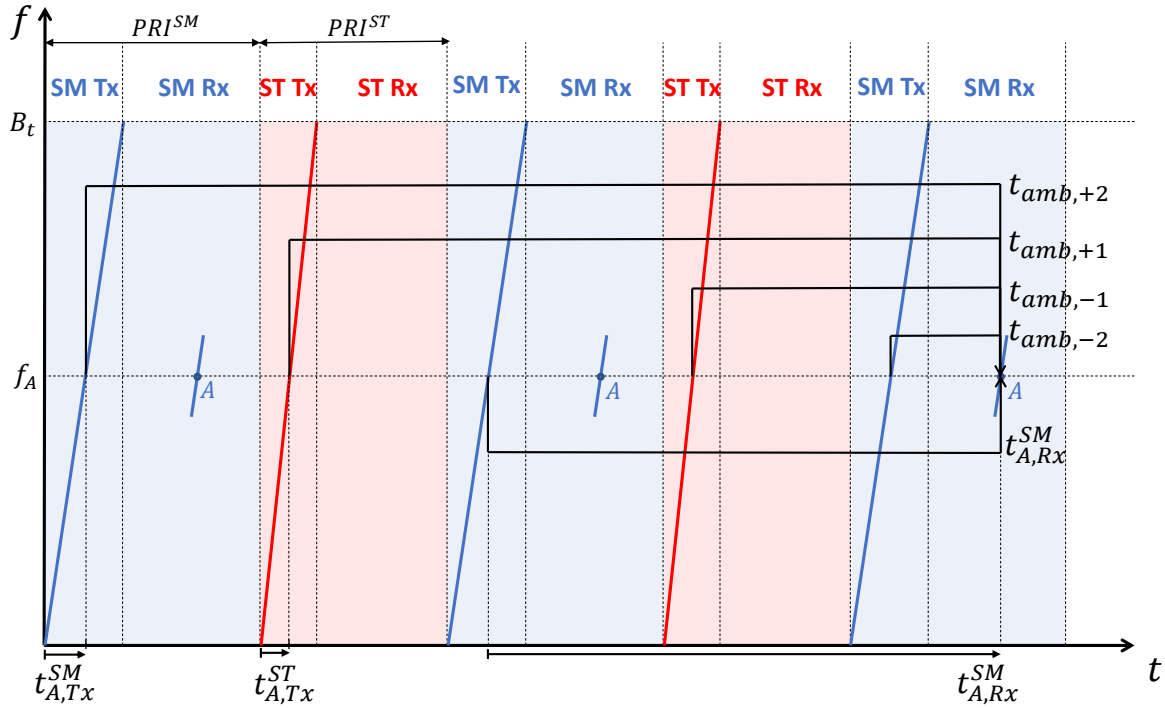


FIGURE 4.25 – Time by frequency plot for an arbitrary acquisition. The objective of this representation is to facilitate the understanding of the origin of the ambiguities in a concurrent F-Scan scenario.

The approach in this thesis is to consider that ambiguities in range only originate from signals with the same frequency/bandwidth as the target. In reality, many other spurious echoes overlap with the target in time. Nevertheless, once they have a different frequency, they may be actually interfering with another target of the scene. It is important to reiterate that the F-Scan processing idea is to differentiate the targets within the swath by their different frequencies.

In Fig. 4.25 the echo delay for the target of interest is represented by the variable $t_{A,Rx}^{SM}$. The instant within the transmission that each mode transmits with the frequency f_A are given by $t_{A,Tx}^{SM}$ and $t_{A,Tx}^{ST}$. Considering the linear up-chirps, the following ambiguity delays can be derived:

$$\begin{cases} t_{amb,-2} = t_{A,Rx}^{SM} - (\text{PRI}^{SM} + \text{PRI}^{ST}) \end{cases} \quad (4.36a)$$

$$\begin{cases} t_{amb,-1} = t_{A,Rx}^{SM} + \frac{f_A}{B_t} \cdot (t_p^{SM} - t_p^{ST}) - \text{PRI}^{SM} \end{cases} \quad (4.36b)$$

$$\begin{cases} t_{amb,+1} = t_{A,Rx}^{SM} + \frac{f_A}{B_t} \cdot (t_p^{SM} - t_p^{ST}) + \text{PRI}^{ST} \end{cases} \quad (4.36c)$$

$$\begin{cases} t_{amb,+2} = t_{A,Rx}^{SM} + (\text{PRI}^{SM} + \text{PRI}^{ST}) \end{cases} \quad (4.36d)$$

For the depicted scenario, it is clear that the even ambiguities come from the same mode transmission, while the odd ones are cross-ambiguities. This differentiation is important as the gains must be calculated using the proper antenna patterns.

The rest of the ambiguities ($t_{amb,\pm 3}$, $t_{amb,\pm 4}$, etc) can be straightforwardly derived from the values obtained in (4.36) by

$$\begin{cases} t_{amb,-k} = t_{amb,-k+2} - (\text{PRI}^{SM} + \text{PRI}^{ST}), \forall k \in \mathbb{N} \mid k \geq 3 & (4.37a) \\ t_{amb,k} = t_{amb,k-2} + (\text{PRI}^{SM} + \text{PRI}^{ST}), \forall k \in \mathbb{N} \mid k \geq 3. & (4.37b) \end{cases}$$

Naturally, the ambiguities timings still have to respect Earth's limits, such that points with echo delays lower than the Nadir or higher than Earth's furthest line-of-sight position are not considered as ambiguities as they simply do not exist.

Another possibility with the concurrent imaging is to receive, for instance, the SM echoes after an ST transmission, and vice-versa. This inversion, fortunately, does not change the way the ambiguities are calculated. Figure 4.26 depicts the timings for this inverted situation considering the very same parameters as before. It can be seen that the timings of the ambiguities do not change.

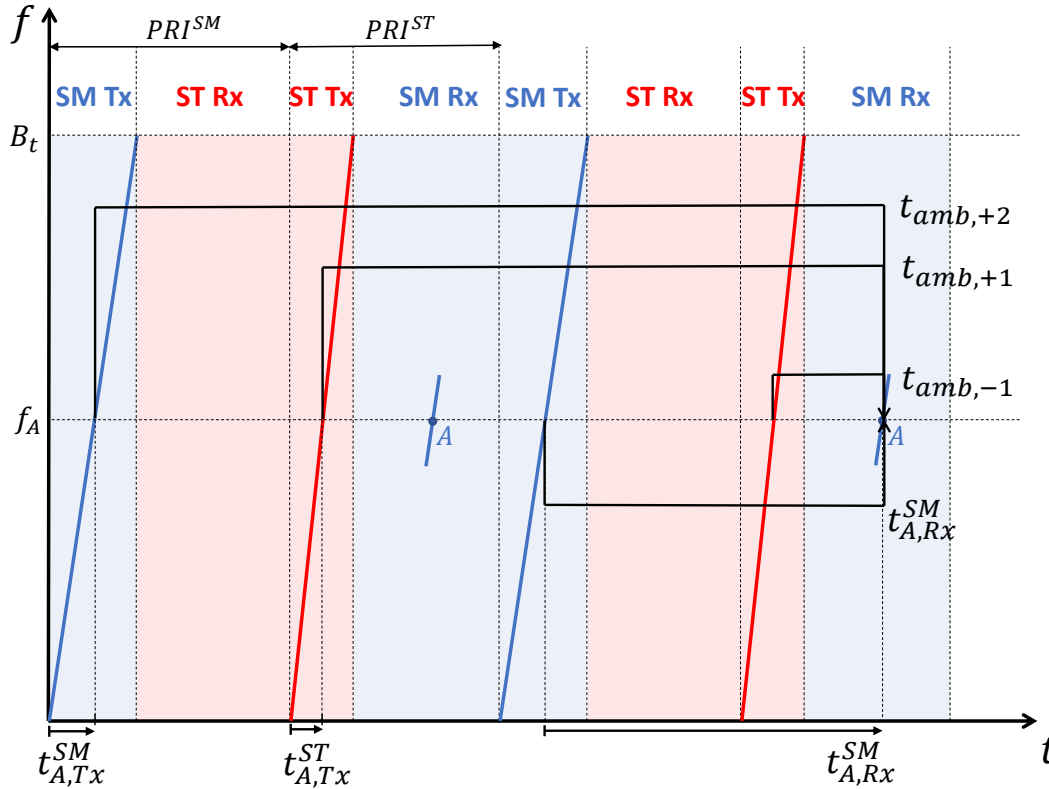


FIGURE 4.26 – Time by frequency plot for an arbitrary acquisition in which the SM echoes are received in the ST echo window, and vice-versa.

It is important to highlight that for this invariability to be possible, one must define the mode PRI as the time duration between the beginning of the respective mode transmission and the end of the following reception. The mode that is actually received in the echo window does not affect the mode PRI. Alternatively, defining the PRI of a mode as the sum of its transmit and receive durations would imply variable PRFs and duty cycles depending on the number of traveling pulses, which could be a potential source of confusion and misunderstandings.

Once the ambiguity positions are well known considering the concurrent aspects, the next step is to calculate the power coming from the target and the ambiguities. Special care must be taken for cross-ambiguities, as the signals are transmitted with one pattern, and received by a different one. In these situations the one-way patterns in transmit and receive must be multiplied so as to achieve the proper gain on receive.

Concerning the F-Scan aspects, the antenna sweeping introduces variable gain to both the target and the ambiguities. The contribution of the sweeping antenna pattern to the echoes power can be considered in two different ways. For a point-target withing the scene, one alternative, and actually more precise, is to discretize the sweeping. This is done by generating numerous antenna patterns relative to the illumination (dwell) time of the given target. For each of these patterns, the point-target and the ambiguities gains can be derived. The RASR can then be ultimately obtained.

The afore-explained approach, however, is not very efficient from a computational point of view, as it requires the generation of a large number of antenna patterns. A more practical and sufficiently precise method is considered in this thesis. The proposed method originates from the overall antenna pattern, specially the first sidelobes, not changing significantly over the sweeping.

The idea consists of using only one antenna pattern, the one pointing with maximum gain towards the target of interest. Next, the target is considered to be extended, with width given by the half power beamwidth of the pattern in elevation. This new equivalent extended target has a near and far range, which then can be used to derive the areas of the ambiguities using the timings previously derived. Finally, the RASR is calculated by

$$\text{RASR}_{\text{F-Scan}} = \frac{\sum_{k=1}^N P_{\text{amb},k}}{P_{\text{target}}} = \frac{\sum_{k=1}^N \frac{t_{\text{dwell},k}}{\beta_{f,k} - \beta_{n,k}} \int_{\beta_{n,k}}^{\beta_{f,k}} \frac{G_{\text{two-way},k} \cdot \sigma_{0,k}}{\sin \theta_{i,k} \cdot R_k^3} d\beta}{\frac{t_{\text{dwell},0}}{\beta_{f,0} - \beta_{n,0}} \int_{\beta_{n,0}}^{\beta_{f,0}} \frac{G_{\text{two-way},0} \cdot \sigma_{0,0}}{\sin \theta_{i,0} \cdot R_0^3} d\beta}, \quad (4.38)$$

with the main differences to (2.5) being the integral and the dwell time. The integral is required to obtain the average gain due to the sweeping aspect of the F-Scan, while

the dwell time considers for how long that ambiguous target is effectively illuminated including the distinctions in PRF, duty cycle and sweeping speed between the modes.

The limits of the integrals represent the near and far range look angles of the equivalent target area. For instance, considering a target in the SM scene, the point-target is assumed to be at $\beta_0 = (\beta_{n,0} + \beta_{f,0})/2$, with $\beta_{f,0} = \beta_{n,0} + \text{HPBW}^{SM}$. Similarly, the same mode ambiguity targets are at $\beta_k = (\beta_{n,k} + \beta_{f,k})/2$, with $\beta_{f,k} = \beta_{n,k} + \text{HPBW}^{SM}$. The area is considered to have an angular width given by the HPBW as it represents the antenna sweeping when illuminating any target.

For cross-mode ambiguities, however, the look angle extension of the equivalent area cannot be simply obtained by the other mode half power beamwidth, in this case HPBW^{ST} , as it does not correctly represent the ST sweeping that leads to the SM effective target bandwidth. Due to the linear scanning, if HPBW^{ST} leads to B_{eff}^{ST} , then the sweeping that leads to B_{eff}^{SM} is given by $\text{HPBW}^{ST} \cdot \frac{B_{eff}^{SM}}{B_{eff}^{ST}}$. Therefore, for cross-mode ambiguities,

$$\beta_k = (\beta_{n,k} + \beta_{f,k})/2, \text{ with } \beta_{f,k} = \beta_{n,k} + \text{HPBW}^{ST} \cdot \frac{B_{eff}^{SM}}{B_{eff}^{ST}}.$$

As a matter of visualization, it is useful to plot the ambiguity areas in the adjusted antenna pattern. Considering the previously introduced exemplary acquisition depicted in Fig. 4.12, Fig. 4.27 shows the self-ambiguity areas in red and the target equivalent area in blue for the near range of the SM image. The gain depicted by the y-axis is the two-way SM antenna pattern adjusted by the backscatter, slant range and sine of the incidence angle. A similar plot for the ST acquisition is depicted in Fig. 4.28.

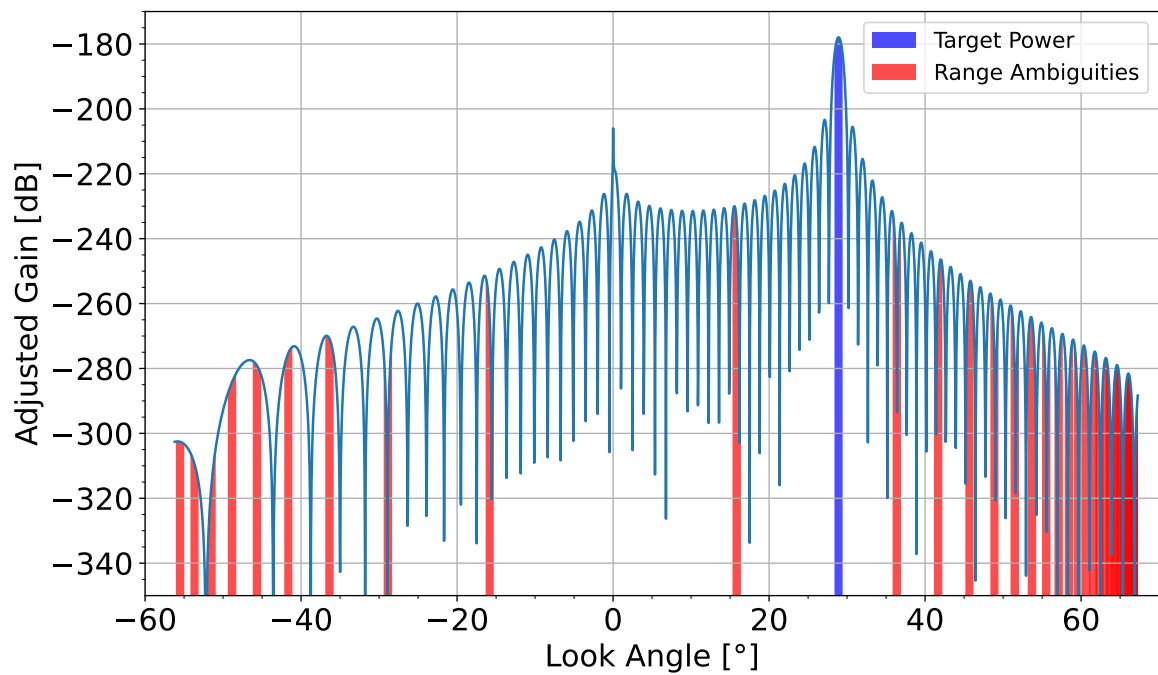


FIGURE 4.27 – SM same mode range ambiguity and target areas for a concurrent F-Scan imaging with PRFs 5650 Hz and 4600 Hz. The near range targets are at look angles of 28.9° (SM) and 48.9° (ST).

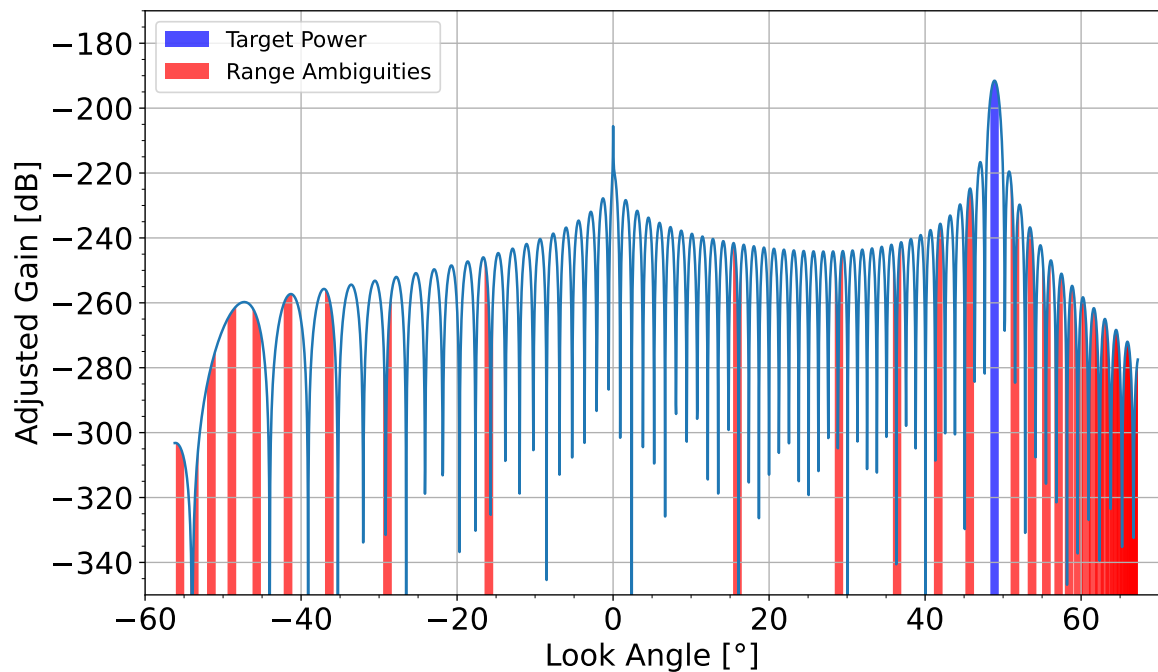


FIGURE 4.28 – ST same mode range ambiguity and target areas for a concurrent F-Scan imaging with PRFs 5650 Hz and 4600 Hz. The near range targets are at look angles of 28.9° (SM) and 48.9° (ST).

The cross-ambiguities can also be shown in a similar plot. However, it is important to use the proper antenna pattern. Once different patterns are used in transmit and receive, the effective two-way pattern is given by the multiplication of the one-way patterns. The adjustments by backscatter, slant range and incidence angle do not change, as they are look angle dependent only. Figures 4.29 and 4.30 depict the range cross-ambiguities for the SM and ST acquisitions, respectively.

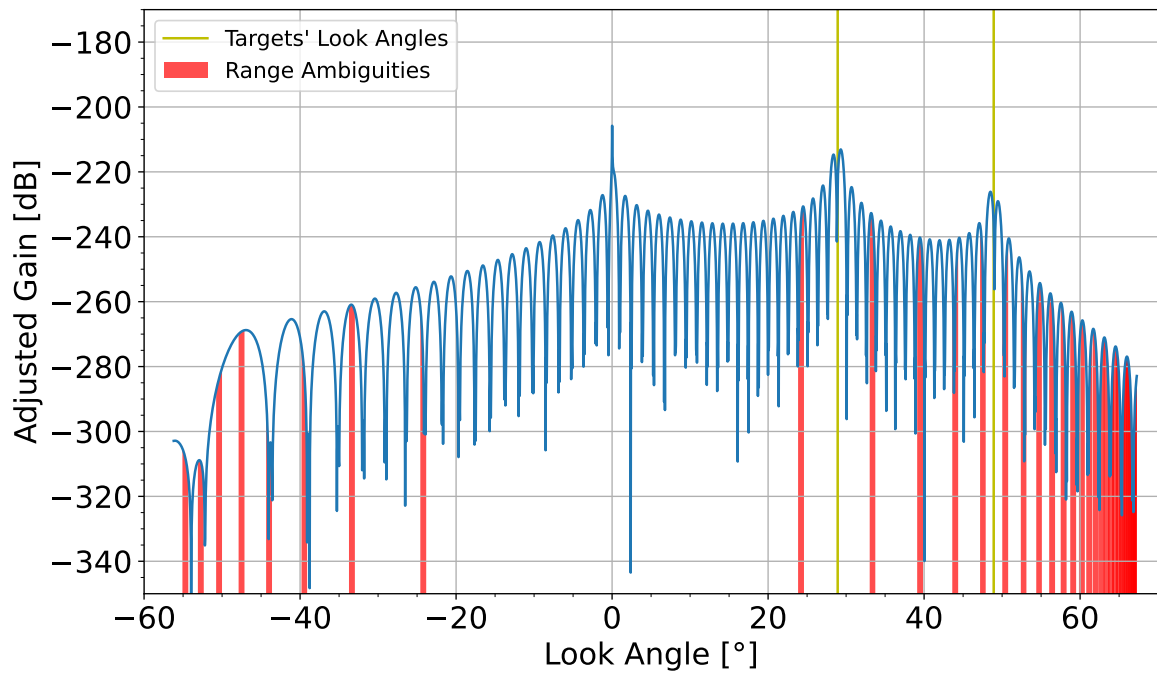


FIGURE 4.29 – SM cross mode range ambiguity areas for a concurrent F-Scan imaging with PRFs 5650 Hz and 4600 Hz. The near range targets are at look angles of 28.9° (SM) and 48.9° (ST).

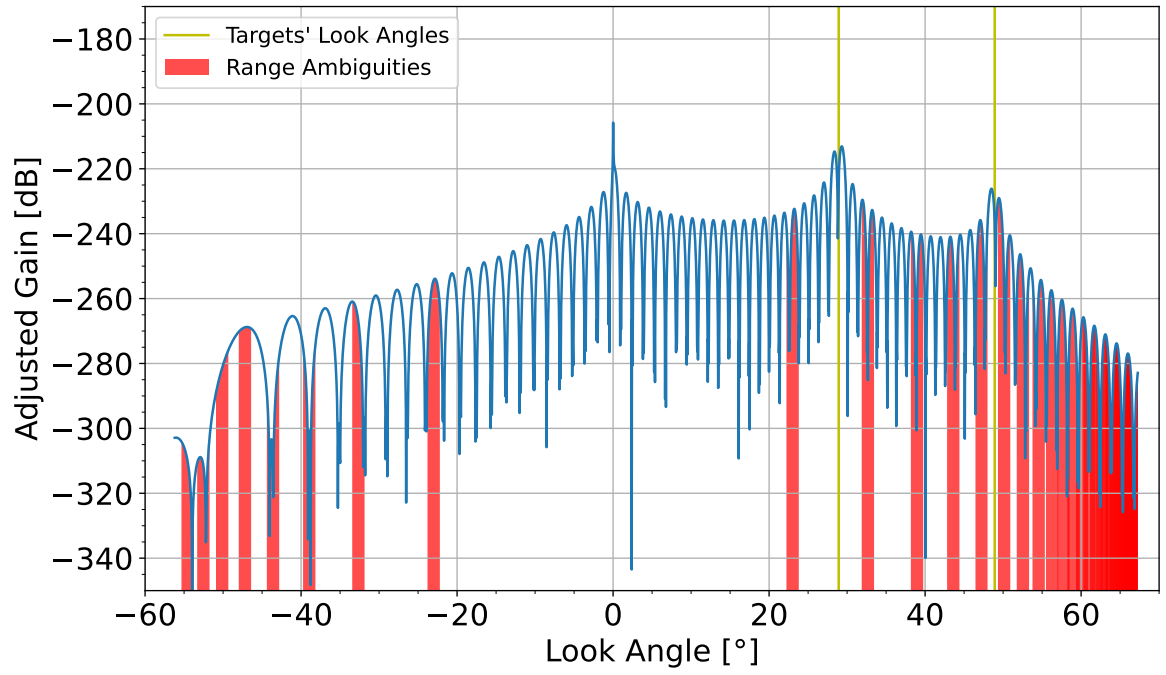


FIGURE 4.30 – ST cross mode range ambiguity areas for a concurrent F-Scan imaging with PRFs 5650 Hz and 4600 Hz. The near range targets are at look angles of 28.9° (SM) and 48.9° (ST).

Finally, this assessment can be extended and performed for any pair of PRFs. From the timing analysis, it was shown that not every PRF is suitable for the acquisition. Then, using the available PRF mask obtained in Fig. 4.13a, only the suitable PRFs need to be investigated in terms of range ambiguities. For each of the acquisitions, the final RASR values are depicted in Figs. 4.31 and 4.32.

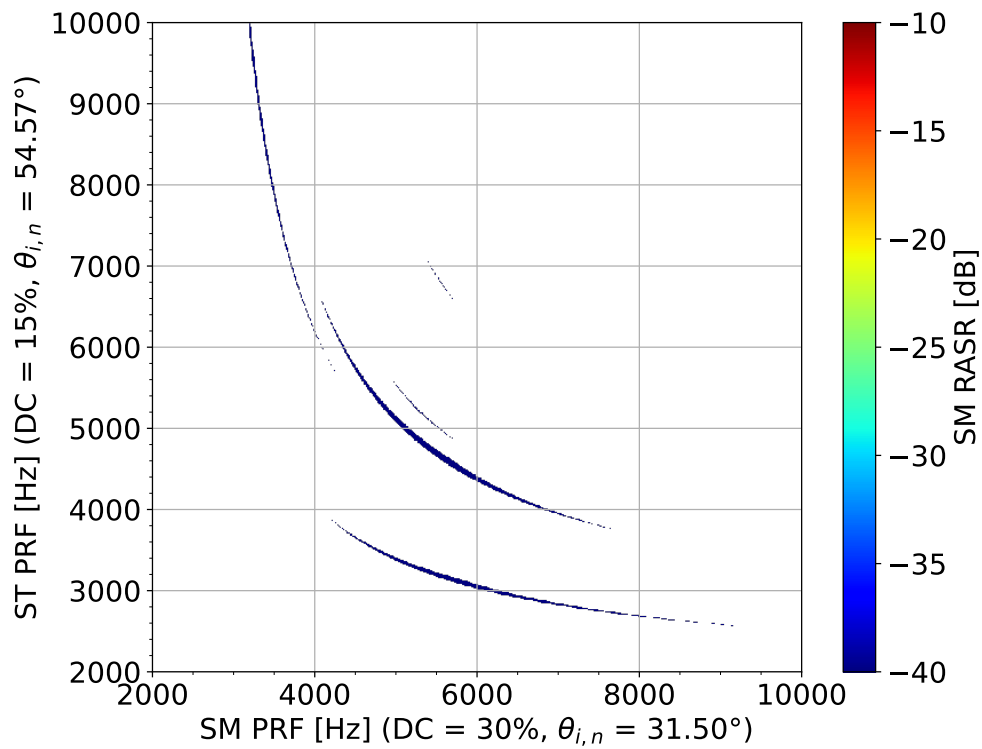


FIGURE 4.31 – SM RASR assessment as a function of the PRFs for a concurrent F-Scan acquisition with targets at look angles of 28.9° (SM) and 48.9° (ST).

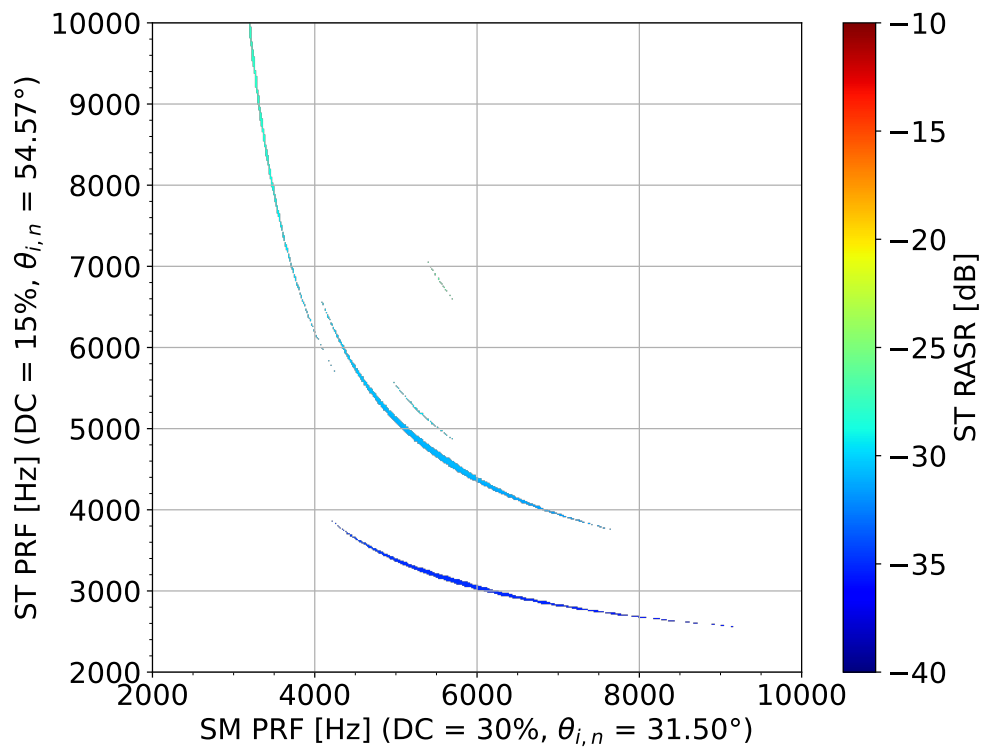


FIGURE 4.32 – ST RASR assessment as a function of the PRFs for a concurrent F-Scan acquisition with targets at look angles of 28.9° (SM) and 48.9° (ST).

Figures 4.31 and 4.32 show RASR values better than -40 dB for the ST acquisition, and better than -28 dB for the SM one. Typically ambiguities are required to be better than -20 dB. Therefore, the values achieved in this simulated acquisition represent an excellent performance.

Among the many PRF combination possibilities, one could, for instance, go for a higher effective PRF, as it would result in better azimuth performance. Alternatively, it is also possible to choose a lower PRF and try to maximize the duty cycles. Personally, due to the results shown in Fig. 4.24, I believe a PRF maximization would be ideal, as it would improve azimuth ambiguities and resolution.

The scenario depicted here is only one among the endless imaging possibilities. Therefore, to get a better picture of the overall performance of the designed mode, a global simulation must be performed. The objective of the next chapter is to derive and analyze the designed concurrent F-Scan mode on a global scale.

5 Global performance

The previous chapters introduced the concurrent imaging mode with F-Scan. For the system envisaged to be the next generation of high-resolution wide-swath SAR systems, the timings, interference, antenna design, and ambiguities were derived. These derivations were visualized for an exemplary acquisition, showing excellent performance. That was, however, only one example among the many global possibilities. To get a more generalized understanding of the mode performance, this chapter aims to derive the performance of the novel mode on a global scale.

The first step towards achieving this goal is to simulate multiple random pairs of targets around the globe. For this purpose, 10000 target pairs are considered. The distance between the targets is conditioned to be between 80 km and 350 km. However, this distance cannot be arbitrary in any direction, as offsets in azimuth are not relevant. This holds because targets at different azimuth positions do not require concurrent imaging but simply two different acquisitions at different moments in time. The lower limit of 80 km was chosen as targets within this distance do not require concurrent imaging, as F-Scan scenes of up to 80 km are already foreseen (BARTUSCH *et al.*, 2021b). On the other hand, the upper limit is simply because distances higher than 350 km would lead to the targets outside the desired incidence angle range.

To overcome this azimuth offset issue, the targets are initially aligned at the same latitude. The latitude range considered is between -70° and $+70^\circ$. Due to the orbit inclination, the beams are tilted in different directions in the ascending and descending orbits. In other words, the satellite has its closest approach to each target at different instants. Therefore, to align the targets in azimuth, one of the targets has to be adjusted for every flyover. This adjustment is simply the orthogonal projection of one of the targets into the line connecting the other target and the orthogonal projection of the satellite on its ground track.

Figures 5.1 and 5.2 show this target adjustment for both the ascending and descending orbits. The initial targets are depicted as 1 and 2, while the adjusted one by 2*. A red arrow is used to highlight the target position adjustment. This step is important to enable the timing analysis for one fixed platform position. The orthogonal projection guarantees

that both targets (1 and 2) will be within the final images.

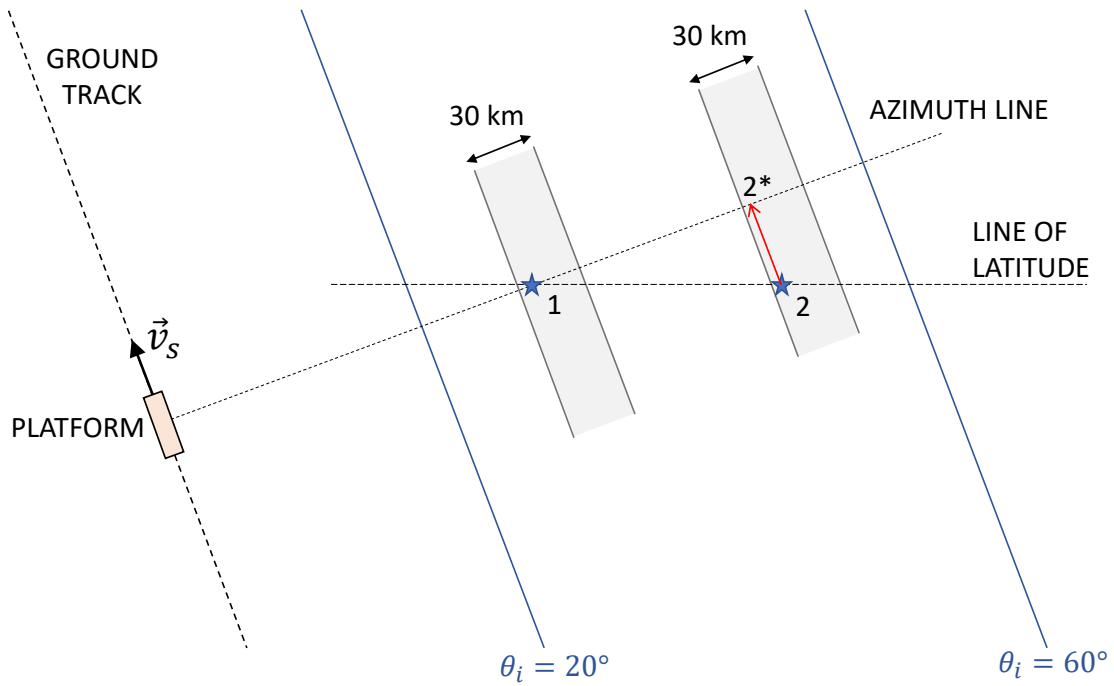


FIGURE 5.1 – Target azimuth adjustment for an ascending orbit imaging.

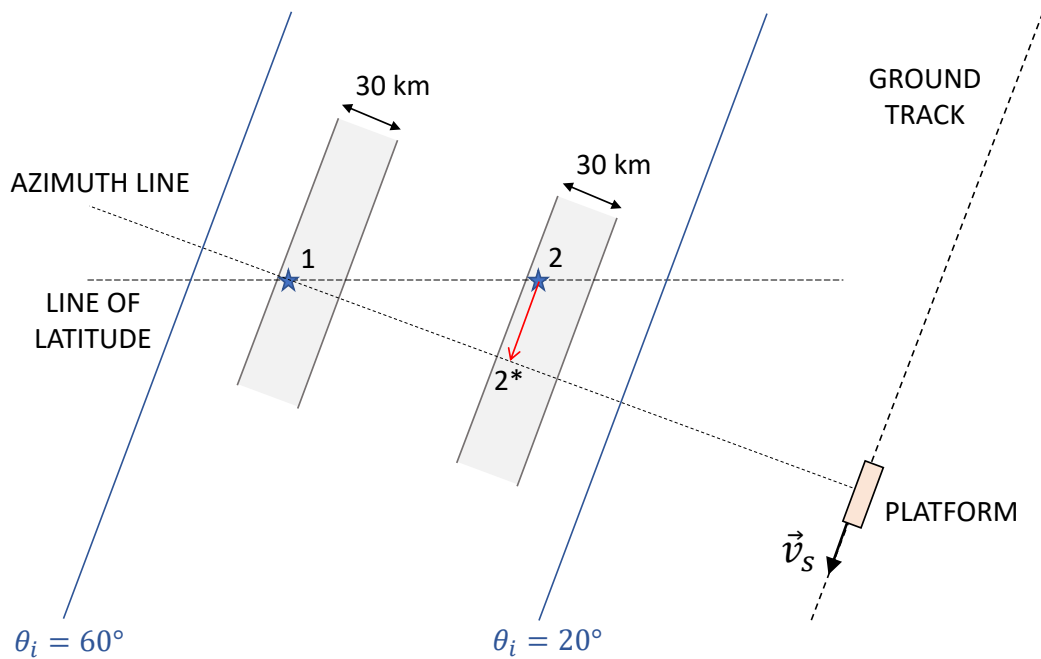


FIGURE 5.2 – Target azimuth adjustment for a descending orbit imaging.

Another constraint for the target scenes is the required swath. For the results presented in this chapter, 30 km scenes (ground range) are considered. The randomized targets are

always assumed to be set at the near range for ascending orbits and at the far range for descending orbits. This definition ensures that the final imaged scenes are roughly the same regardless if an ascending or a descending acquisition is selected. Important to notice that the orbit inclination depicted in Figs. 5.1 and 5.2 are exaggerated for visualization. In reality, the inclination is approximately 97.4° .

Limits have to be defined on the allowed incidence angles to avoid strong degradation and distortion of the images. In this simulation, a minimum and maximum incidence angles at the near range of 20° and 60° have been considered. These values were chosen as they are typical for data acquisition with TerraSAR-X (EINEDER *et al.*, 2013).

For the pulse design, as previously justified, a minimum effective PRF of 2000 Hz paired with duty cycles of 15 % and linear up-chirps are considered. The individual mode PRFs are limited to 10000 Hz as higher values would not only lead to a lack of echo window length to receive the echoes but also to deterioration in the range ambiguities. Due to the computational complexity being $O(n^2)$ in PRF, the PRF range array is discretized with a 50 Hz step size to achieve reasonable computing time. This limitation leads to slightly lower availability and average performance but is already enough to draw the overall mode performance.

In each of the simulations, an important decision is the PRF selection. This goes beyond the determination if the acquisition is possible or not from a timing point of view. Actually, for most of the simulated targets, many PRFs are possible, as it was shown in Fig. 4.13, for instance. Due to the degraded azimuth performance (due to the concurrent aspect) and excellent range performance (due to the F-Scan aspect), the highest effective PRF is desirable. Another interesting PRF is the one closest to the DPCA target obtained in (4.1), as it allows for better azimuth reconstruction (KRIEGER; GEBERT; MOREIRA, 2004). In summary, for each simulation two effective PRFs will be selected: the highest available and the closest to the DPCA target. The highest available PRF case is analyzed in Section 5.1, in which DPCA is not considered. Section 5.2, on the other hand, shows the results for the PRFs closest to the target DPCA one.

Ultimately, for each pair of selected PRFs, performance parameters will be retrieved. Namely, azimuth and range ambiguities and resolutions are of great interest. Concerning the processed Doppler bandwidth, the azimuth resolution that would be achieved by $\frac{v_g}{\text{PRF}_{eff}}$ is limited to half the antenna size. In other words, if $\text{PRF}_{eff} > \frac{2v_g}{L} \approx 2371\text{Hz}$, then the remaining available bandwidth is not processed, and an oversampling factor is considered. Processing beyond this bandwidth – equivalent to approximately the -6 dB points of the two-way pattern – would lead to SNR degradation. This oversampling is then used to improve the azimuth ambiguities. It will be shown that the achieved resolution is not exactly half the antenna length due to the Hamming window applied.

The performance of any mode is clearly not uniform globally. Depending on the latitude and the target positions relative to the satellite orbit, different performances are achieved. This is especially true for concurrent F-Scan acquisitions, in which the extra degree of freedom that is the distance between the targets makes each pair of targets unique. Therefore, due to this big variance in performance between the randomized targets, density plots are used to depict the performance. These plots will show a higher probability density with colors shifted towards the red and lower densities towards the blue.

For instance, starting with the number of overpasses of the satellite over the two targets, Fig. 5.3 shows the distribution of how many times both simulated target scenes are completely within the required incidence angle range for one orbit cycle. It can be seen that there is a great concentration at four overpasses, with two being the minimum. Moreover, the mean number of flyovers is about five and 90 % of the acquisitions have eight or less flyovers. Finally, as expected, due to the orbit geometry, there are more opportunities at higher latitudes than at the Equator. This sort of visualization will be used in the following sections to observe the performance behavior of the mode.

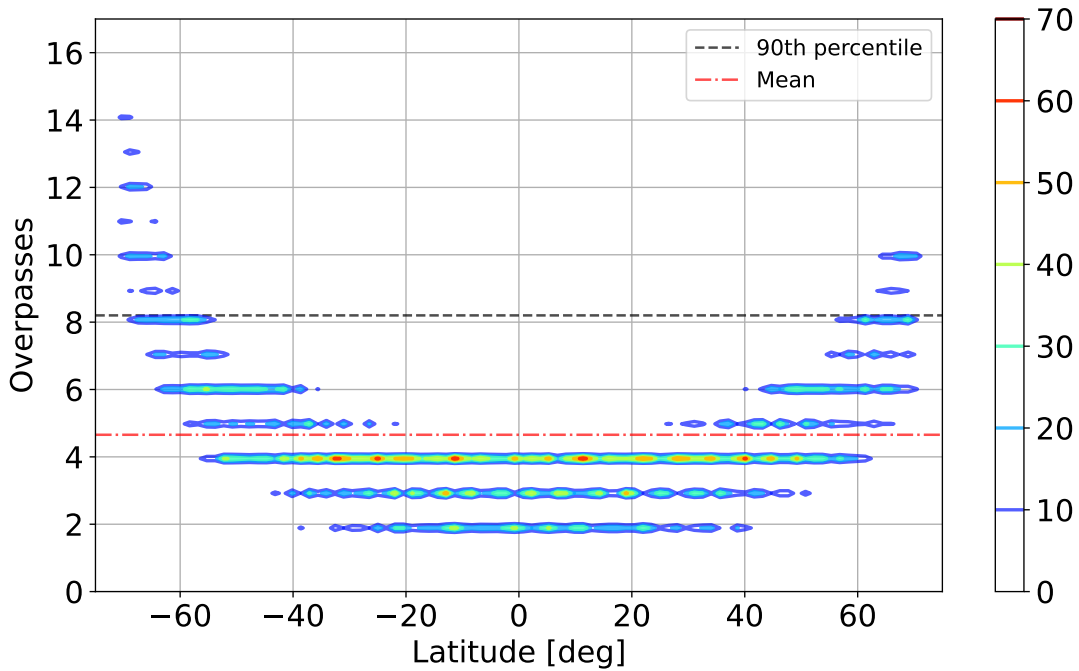


FIGURE 5.3 – Number of flyovers of the satellite over the target areas within one orbit cycle.

The timing analysis is performed for each overpass to obtain the PRFs of interest. Then, for each of the PRFs, the imaging performance is assessed for both target scenes.

5.1 Global Performance without DPCA

Due to the intrinsic range/azimuth separation, for the sake of clarity it is worth separating the results in two subsections. First, range performance will be shown, followed by azimuth.

5.1.1 Range

In range, the main parameters involved are ambiguity, slant and ground range resolutions, incidence angles, PRFs and target distances. Initially, the resolution achieved by the mode is investigated. The slant range resolution δ_{rg} can be calculated by (4.10). Due to the wide range of incidence angles, the ground range resolution δ_{gr} is also of interest, and is obtained by

$$\delta_{gr} = \frac{\delta_{rg}}{\sin \theta_i} = \frac{0.886 \cdot c_0}{2 \cdot B_{eff} \cdot \sin \theta_i} \cdot \gamma_{w,r}. \quad (5.1)$$

The slant range resolution as a function of the incidence angle of the scene centers is depicted in Fig. 5.4. It is shown that the range resolution is well contained below 0.55 m, with its mean at 0.42 m. Due to the Hamming window applied, the resolution is degraded by a factor of 32 %. Nevertheless, the window brings great benefits not only in terms of azimuth ambiguities but also of sidelobe ratios. For instance, this considered Hamming window improves the theoretical peak-to-sidelobe ratio (PSLR) from 13.2 dB to 45.3 dB. Achieving high sidelobe suppression is essential, especially in urban and industrial environments, where the presence of many strong scatterers may conceal adjacent objects with lower radar cross-section (RCS). The same trade-off between resolution and sidelobe ratio is present in azimuth.

Fig. 5.4 also shows that targets at higher incidence angles have better resolution. This is expected as at these higher incidence angles the 30 km scene represents a smaller angular aperture. Therefore, the HPBW of the antenna in elevation is more significant, so that the dwell time relative to the pulse duration is increased. Ultimately, the effective bandwidth is also increased.

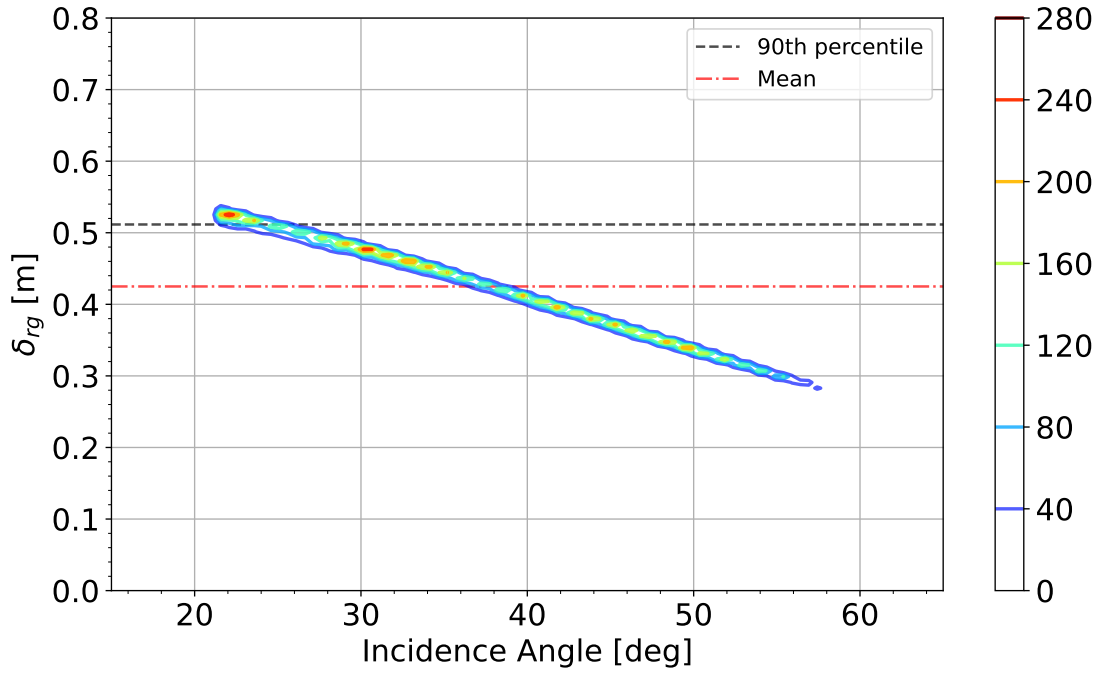


FIGURE 5.4 – Slant range resolution as a function of the incidence angle of the scene center for the simulated targets. The selected PRF is the highest available.

The fact that lower incidence angles are imaged with lower resolution raises concern about the ground range resolution. Consequently, this parameter is also of interest and is depicted in Fig. 5.5. It can be seen that the ground range resolution at the scene center is mostly sub-meter, with a maximum of about 1.4 m for targets at 20°. On average, the ground range resolution is still around 0.8 m, representing excellent performance.

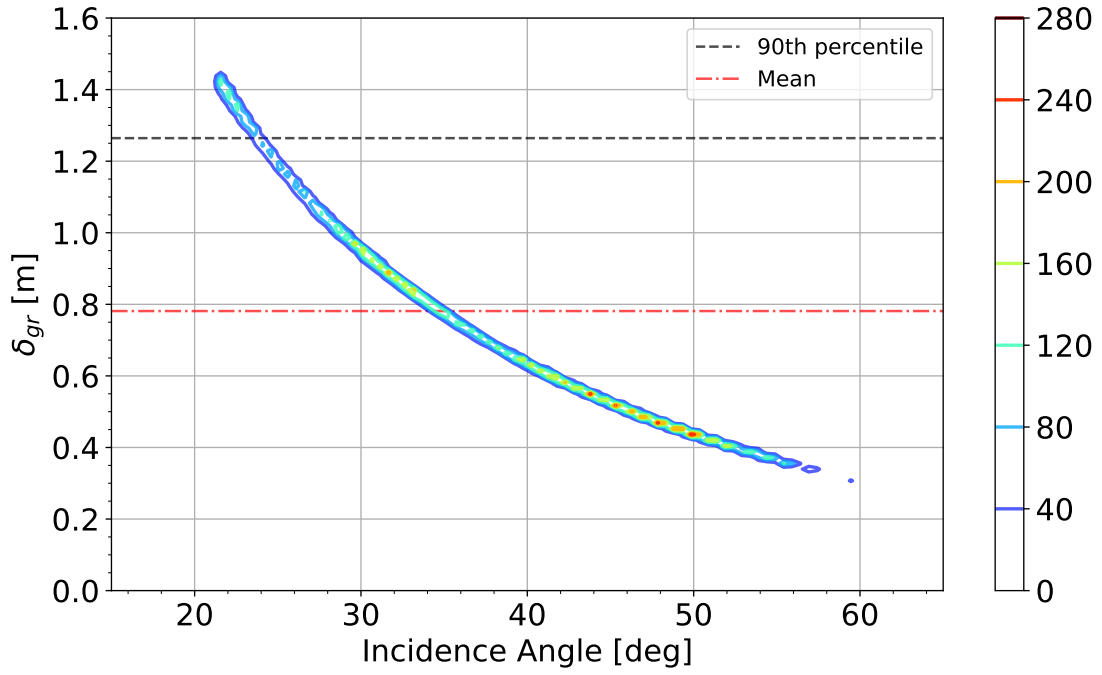


FIGURE 5.5 – Ground range resolution as a function of the incidence angle of the scene center for the simulated targets. The selected PRF is the highest available.

It is also important to observe if the range resolution is affected by the distance between the targets. Fig. 5.6 depicts how the slant range resolution of the scene at the lower incidence angle ($\delta_{rg,near}$) varies with the distance. It becomes clear that the distance between the scenes does not deteriorate the range resolution. Actually, the resolution is mostly invariant with respect to the distance.

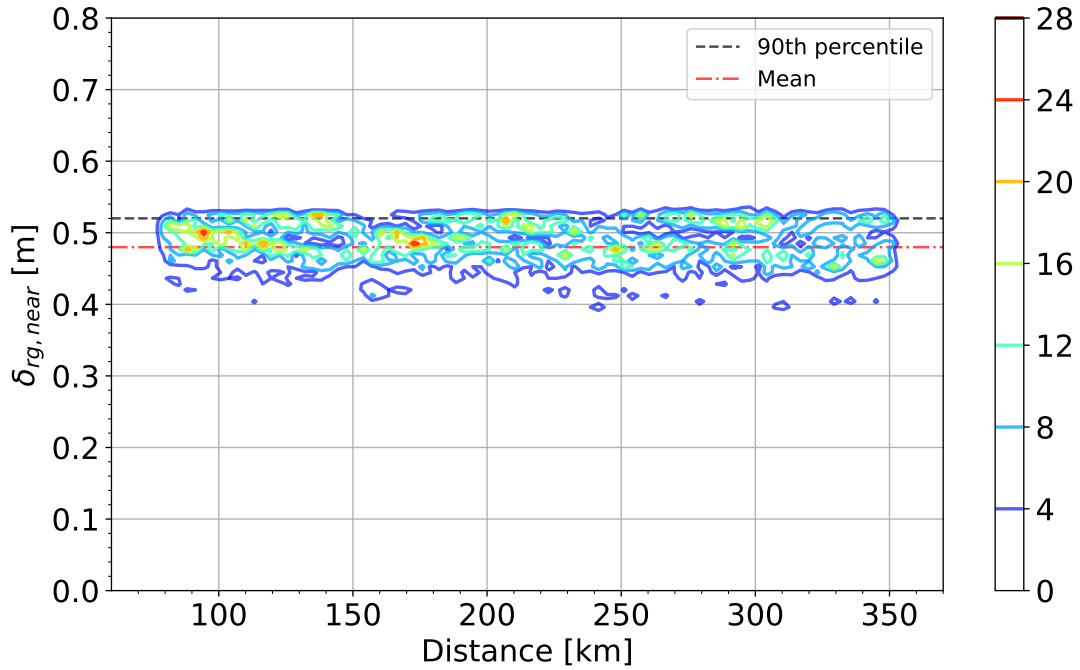


FIGURE 5.6 – Slant range resolution as a function of the distance between the simulated targets. The selected PRF is the highest available.

Following the investigation with range ambiguities, Fig. 5.7 depicts the RASR as a function of the incidence angle of the scene center. In these simulations, the RASR is given as roughly the worst case within the scene. It is calculated as the worst value among near range, scene center, and far range. The plot shows that the RASR is mostly below -30 dB, with the worst case at about -24 dB at high incidence angles. These values represent, once again, excellent results. Moreover, performance degradation for higher incidence angles can be seen. This behavior is the same for traditional imaging modes, as the ambiguity areas become closer to the target, leading to higher ambiguity power.

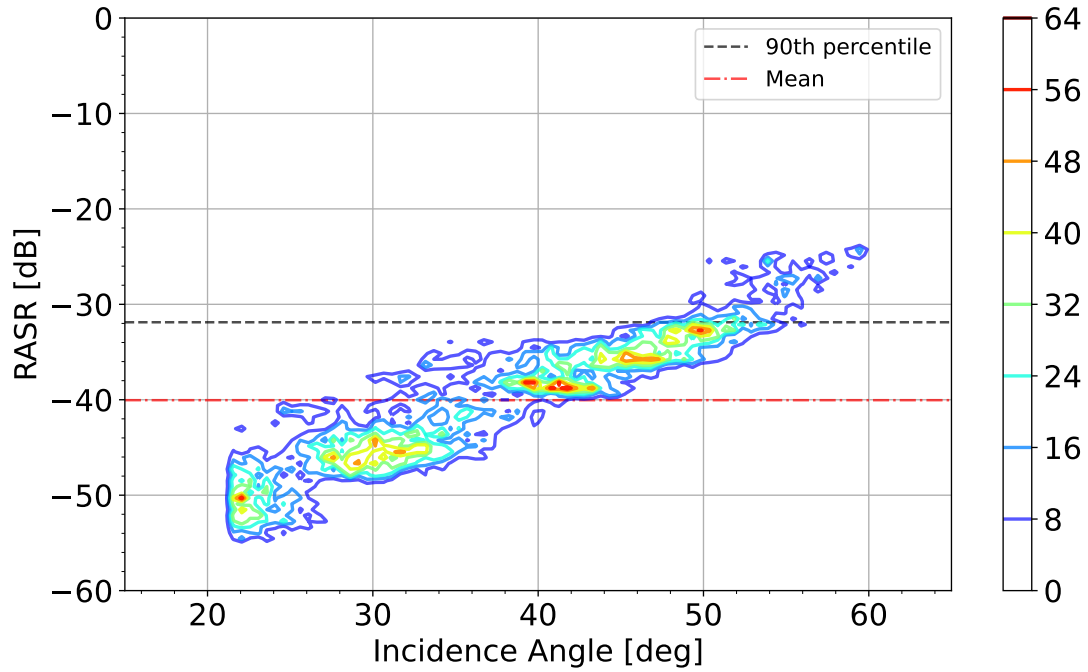


FIGURE 5.7 – RASR as a function of the incidence angle of the scene center for the simulated targets. The selected PRF is the highest available.

It is also important to observe if the distance between the targets deteriorates the range ambiguity performance. Figure 5.8 shows the RASR for the scene at the higher incidence angle (RASR_{far}). The far scene was chosen as it has worse range ambiguities when compared to the other scene, which is at a lower incidence angle. Naturally, for distances higher than 300 km, the far scene ends up at a high incidence angle, meaning, therefore, slightly degraded ambiguity performance. However, apart from these higher distances, the distance is shown to have little influence over the RASR overall.

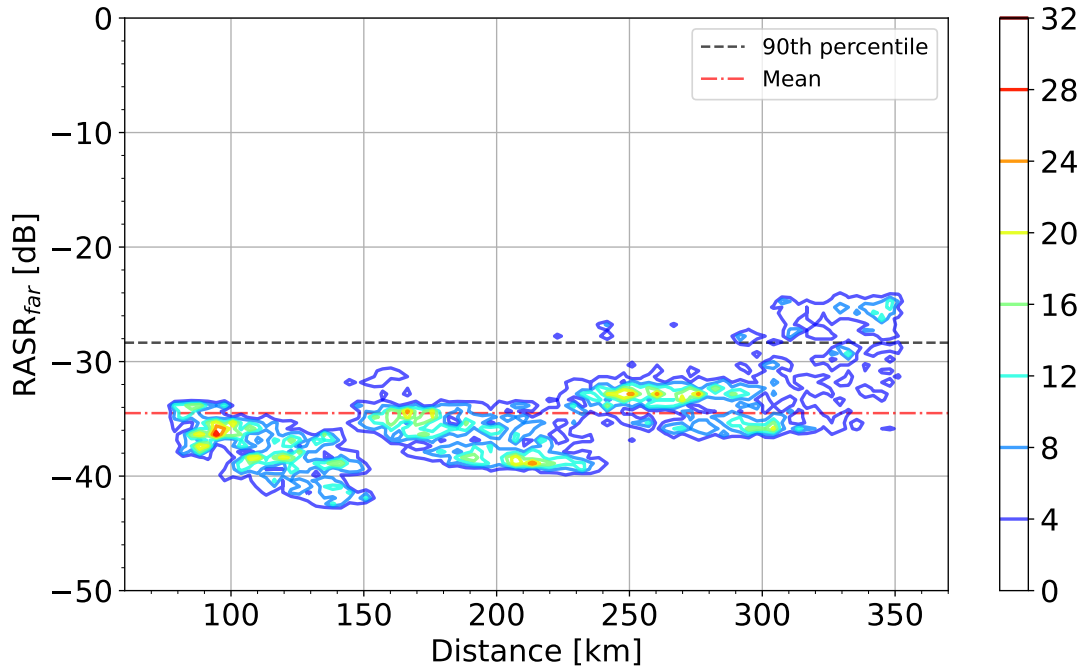


FIGURE 5.8 – RASR as a function of the distance between the simulated targets. The selected PRF is the highest available.

Finally, even though resolution and ambiguities are not directly connected, it is interesting to understand the trade-off between these parameters. Figure 5.9 shows that one is maximized when the other is minimized. In other words, it is not possible to achieve the best performance in both range resolution and range ambiguity. As it was shown, these parameters are actually more dependent on the incidence angle but now it becomes clear that they cannot be concomitantly improved by selecting the highest available PRF.

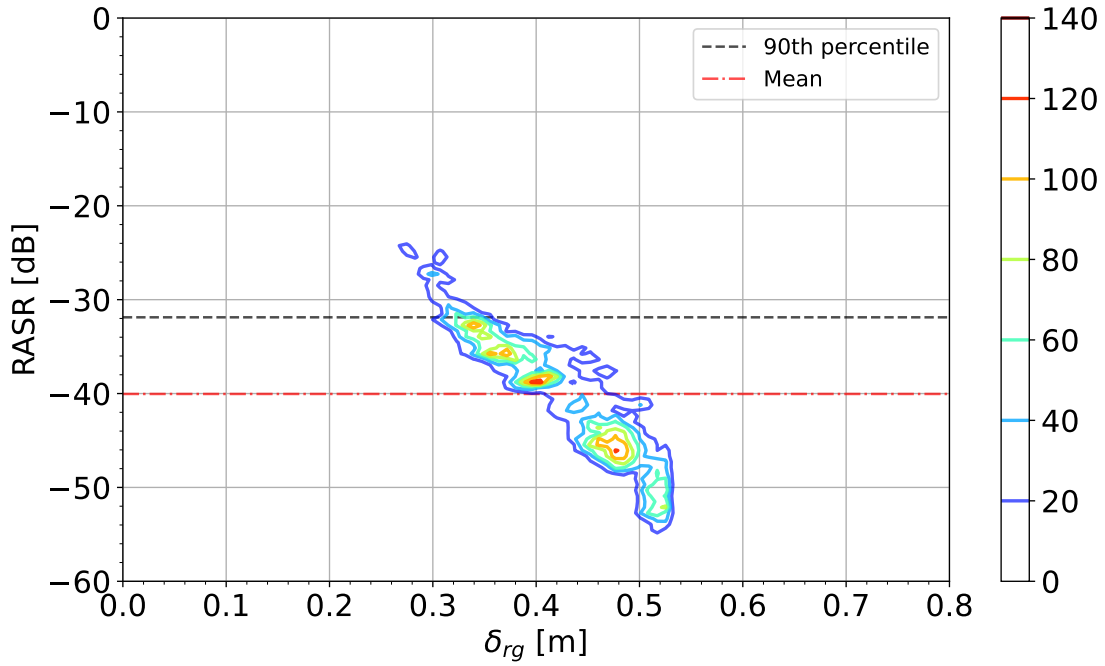


FIGURE 5.9 – RASR as a function of the slant range resolution of the simulated targets. The selected PRF is the highest available.

In summary, the performance in range achieved by selecting the highest available PRF is excellent. Not only sub-meter resolution can be achieved, but also the RASR is kept mostly below -30 dB. This improvement is chiefly a consequence of the broad system bandwidth of 1200 MHz, and of the frequency scanning technique, which improves the time domain usage and spreads the bandwidth across the scene.

5.1.2 Azimuth

A similar analysis can be performed in azimuth, i.e., the investigation of resolution and ambiguity ratio. In concurrent mode acquisitions, both scenes have the same sampling in azimuth given by the effective PRF. After applying an oversampling factor, as in (2.11), the effective processed azimuth bandwidth is given by $\Delta f_{d,eff}$. Naturally, different oversampling factors can be applied to each of the target scenes if desired. Hence, the azimuth resolution for Stripmap acquisitions is obtained by

$$\delta_{az} = \frac{0.886 \cdot v_g}{\Delta f_{d,eff}} \cdot \gamma_{w,a}, \quad (5.2)$$

where $v_g \approx 7114$ m/s is the satellite ground speed, and $\gamma_{w,a} \approx 1.32$ is the broadening factor in azimuth due to the Hamming window (CUMMING; WONG, 2005).

As previously mentioned, the maximum processed Doppler bandwidth is set at 2371 Hz,

so that the best resolution achieved is

$$\delta_{az} = \frac{0.886 \cdot 7114 \text{ m/s}}{2371 \text{ Hz}} \cdot 1.32 = 3.5 \text{ m} \quad (5.3)$$

If the effective PRF of the acquisition is lower than 2371 Hz, then the resolution will be higher than 3.5 m.

Finally, Fig. 5.10 depicts the azimuth resolution as a function of the incidence angle for the simulated targets. The figure shows that the vast majority of the acquisitions manage to achieve the nominal resolution.

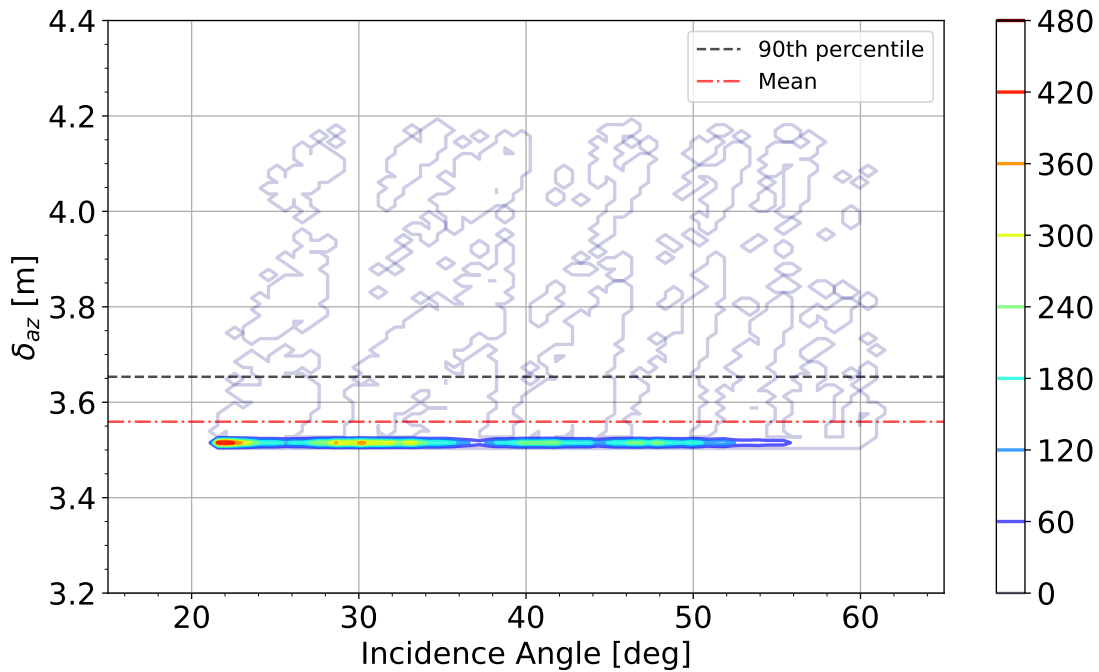


FIGURE 5.10 – Azimuth resolution as a function of the incidence angle of the scene center for the simulated targets. The selected PRF is the highest available.

A very similar plot is obtained when the azimuth resolution is plotted as a function of the distance between the targets. Consequently, the distance has also no effect over the resolution in azimuth.

Concerning the ambiguities in azimuth, it is clear that there is a direct relation between the effective PRF and the AASR, as it was shown in Fig. 4.24. For the simulation in question, the AASR distribution as a function of the effective PRF is depicted in Fig. 5.11. The plot shows an average AASR of -20 dB, with 90 % of the cases better than -17 dB.

In some acquisitions the AASR drops to undesirable values, in which the image quality may be degraded depending on the characteristics of the scenes. These acquisitions are

those in which low PRFs have to be used. The necessity of using low PRFs in these cases typically does not come from the necessity of receiving data for a long period of time. Actually, in these scenarios a great part of the receive echo window is simply not used. The need for low PRFs is driven by how strict the target scenes are defined. To recapitulate, not only two 30 km scenes are being targeted, but also their exact location with no flexibility. For instance, if only a specific point target within each scene were required, there would be some flexibility on the 30 km swath position, allowing for higher effective PRFs.

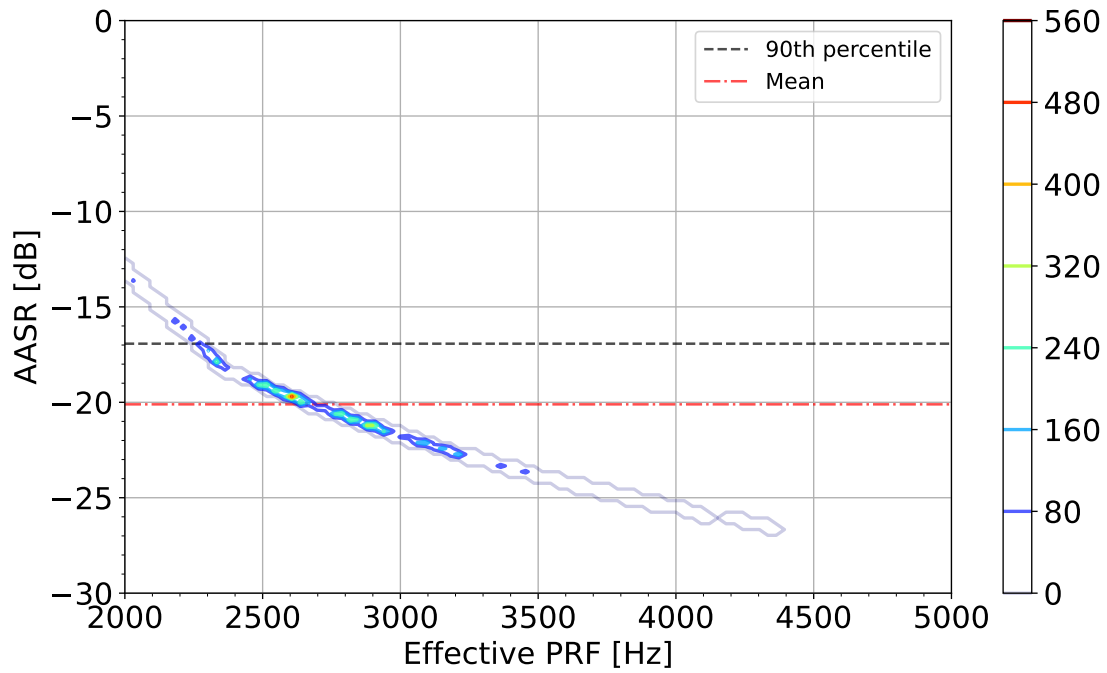


FIGURE 5.11 – AASR as a function of the effective PRF used in the acquisitions. The selected PRF is the highest available.

The AASR can also be seen in two other domains of interest: incidence angle and distance between the targets. These results are depicted in Figs. 5.12 and 5.13. Both figures show little influence of the incidence angle or distance on the AASR.

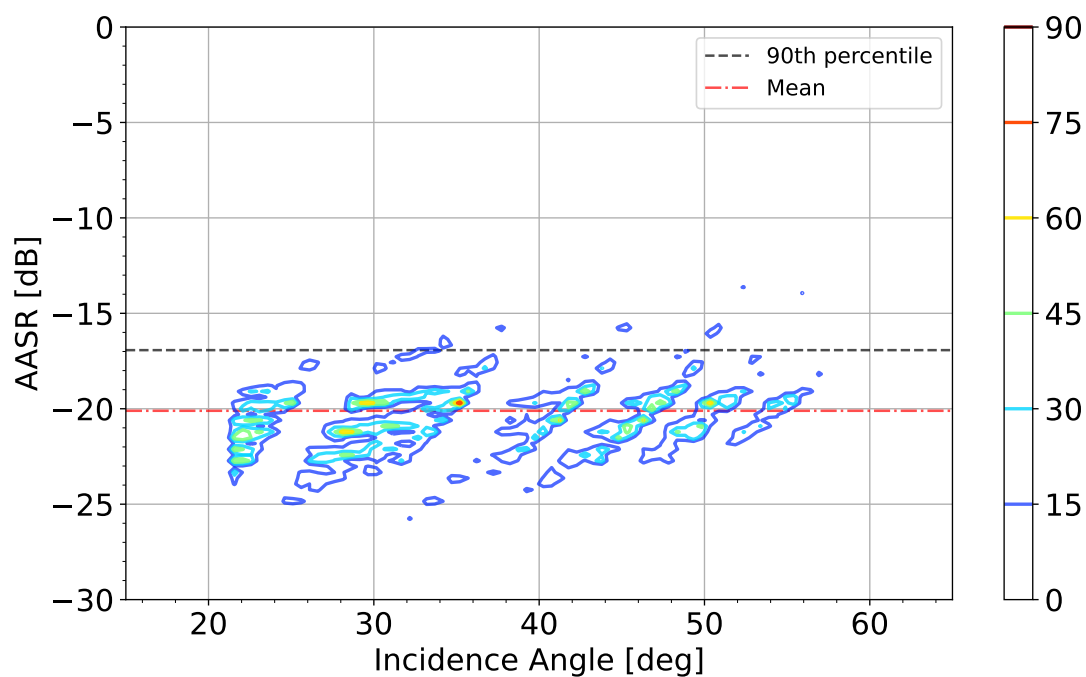


FIGURE 5.12 – AASR as a function of the incidence angle of the scene center for the simulated targets. The selected PRF is the highest available.

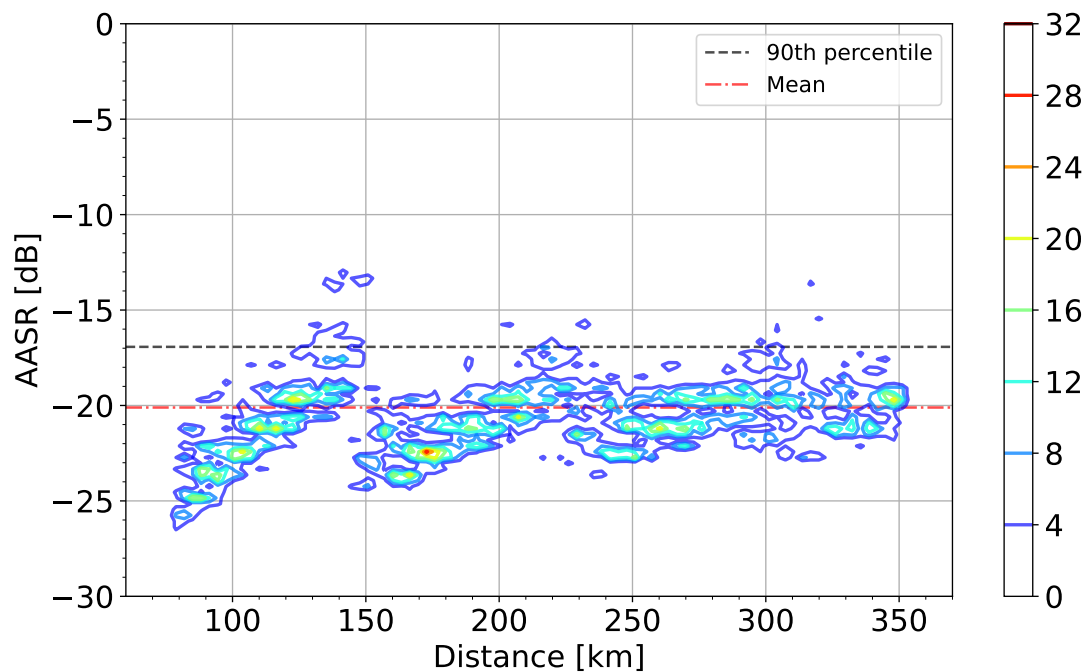


FIGURE 5.13 – AASR as a function of the distance between the simulated targets. The selected PRF is the highest available.

5.1.3 Unavailable Acquisitions

The performance shown in this section is relative to those acquisitions that would be successfully acquired. However, some of the random targets were not available from a PRF point of view, given the restrictions defined. The reason for this unavailability has already been described, but in summary, it originated from the minimum effective PRF limit of 2000 Hz (that would lead to poor azimuth performance) and the rigid 30 km scenes. In the scenario and restrictions considered in this section, an availability of 97.90 % was achieved. This represents an extremely satisfactory result, as most of the acquisitions can be successfully acquired. This remaining 2.1 % can probably be obtained by introducing more flexibility to the scenes. In other words, the swaths would not necessarily need to be reduced but slightly shifted.

Selecting only the unfeasible acquisitions, Fig. 5.14 depicts the target distance and latitude of these unavailable targets. Two trends can be observed in the plot. First, a certain discretization in the distance domain is clear, especially at about 140 km, but also at 240 km and 340 km. This distance discretization comes from the unavoidable transmit interferences. Secondly, it is also clear that at higher latitudes, the availability increases again. This is a direct consequence of Fig. 5.3, i.e., there are more flyovers and imaging opportunities at higher latitudes.

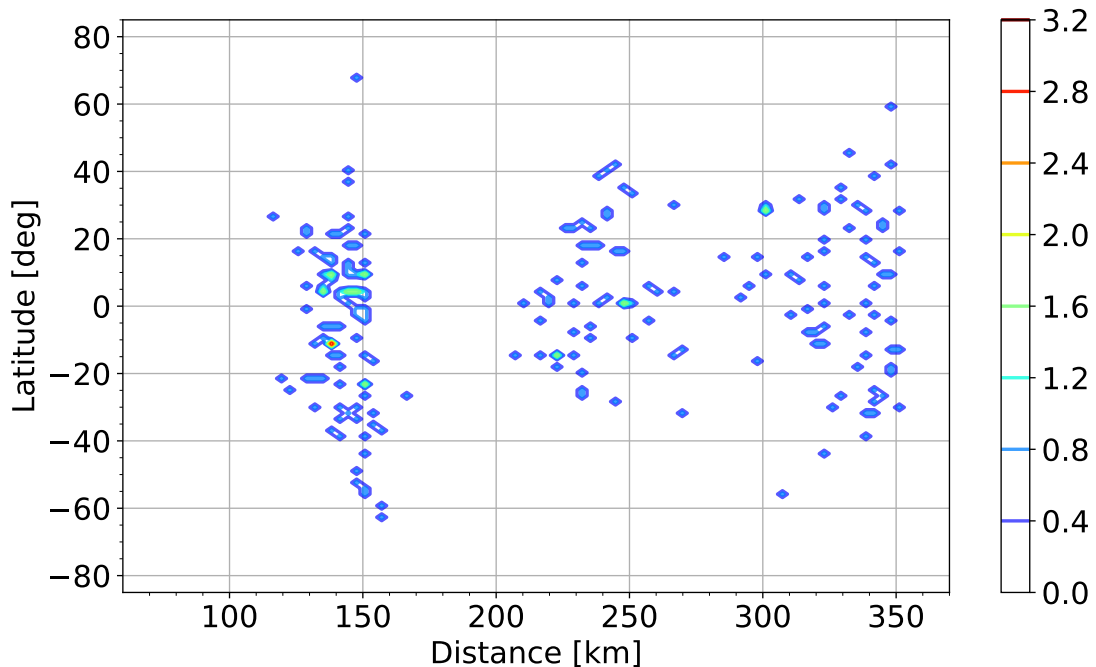


FIGURE 5.14 – Latitude-distance bivariate distribution of the unavailable targets when DPCA is not considered.

5.2 Global Performance with DPCA

In this section, the performance of the mode considering the DPCA restrictions will be analyzed. The PRF selection consists of finding the available PRFs closest to the target DPCA PRF. However, some limit has to be set around the target PRF to avoid strong image quality degradation in the azimuth reconstruction. In this simulation, an offset of up to 200 Hz is considered as acceptable. In other words, only the effective PRF range between 2335 Hz and 2735 Hz is considered, and the closest one to the target is selected. Deviating from the DPCA PRF naturally leads to image quality degradation. The parameters that are affected (and how intense the degradation is) strongly depend on the reconstruction method (CERUTTI-MAORI *et al.*, 2014).

5.2.1 Range

In range, the DPCA, a technique in azimuth, does not influence performance. Therefore, the slant range resolution and the range ambiguities depicted in Figs. 5.15 and 5.16 are quite similar to the scenario where DPCA was not considered. Once again, the range performance is excellent throughout the whole incidence angle range.

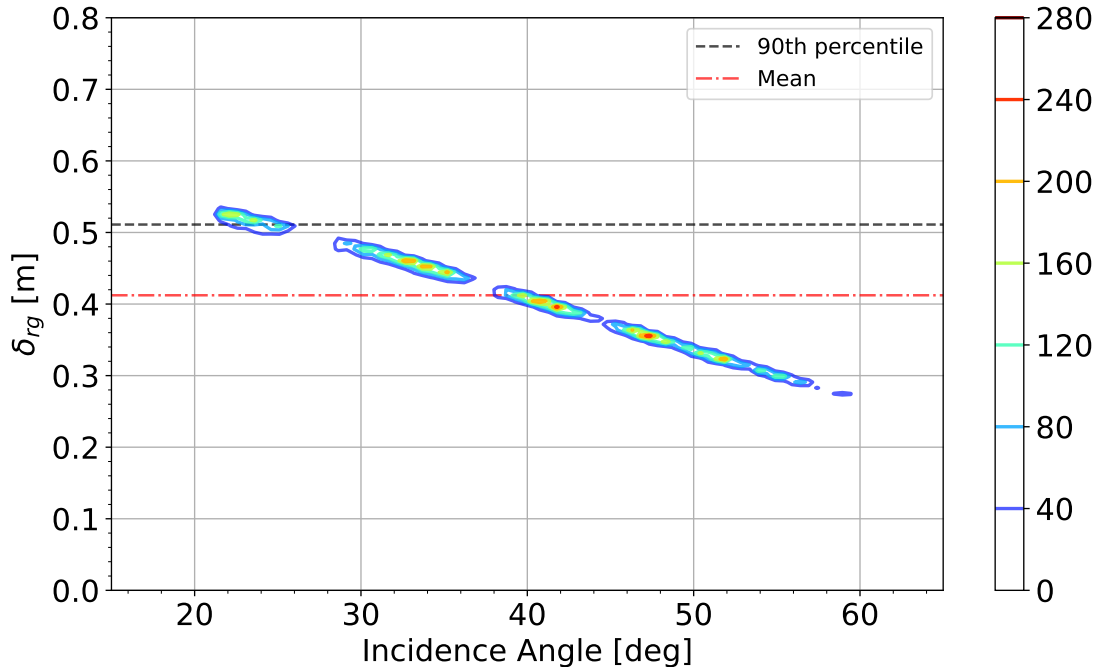


FIGURE 5.15 – Slant range resolution as a function of the incidence angle of the scene center for the simulated targets. The selected PRF is the closest possible to the target DPCA.

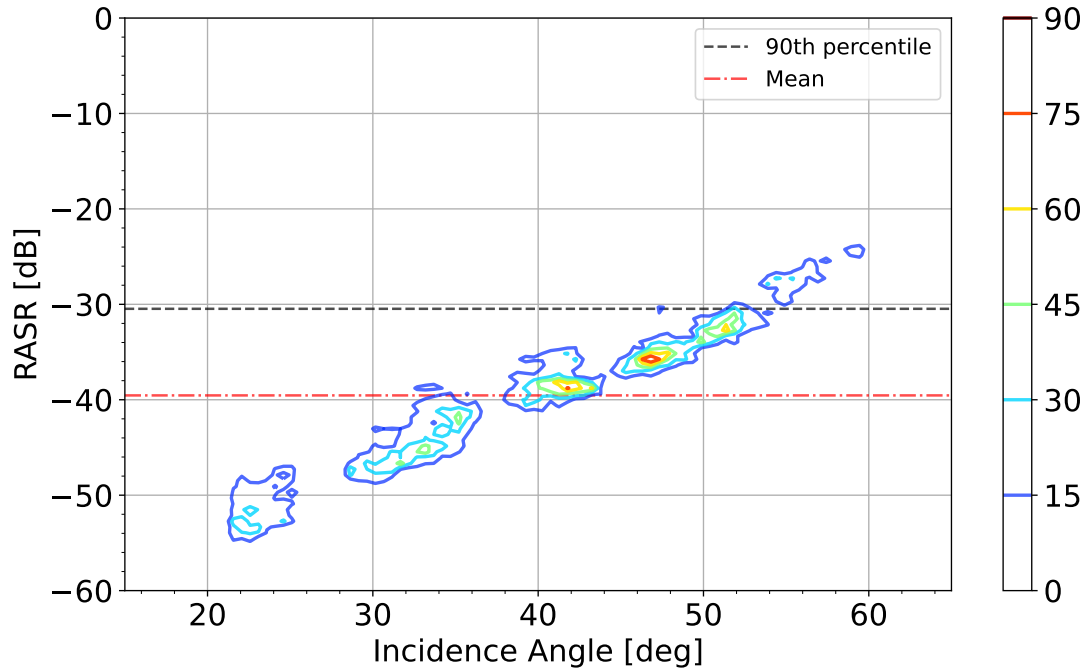


FIGURE 5.16 – RASR as a function of the incidence angle of the scene center for the simulated targets. The selected PRF is the closest possible to the target DPCA.

The most apparent difference in these plots compared to the previous ones is some discontinuities in the incidence angle domain. These empty regions represent those incidence angles that are never imaged. This is an immediate consequence of the PRF restriction. Due to this limitation, i.e., some incidence angles not being available with the PRF range considered, it will be shown in the following subsections that the overall availability decreases, as expected.

5.2.2 Azimuth

If in range the performance is similar, in azimuth, on the other hand, it changes significantly. Even though DPCA involves restrictions on the PRF, its improvements in terms of azimuth resolution are extremely valuable. The DPCA here considers four phase centers, so that the resolution is also improved by the same factor. Figure 5.17 depicts the azimuth resolution achieved as a function of the incidence angle of the scene center. From the plot, it becomes evident that excellent sub-meter performance is made possible by the DPCA technique. Naturally, it must be recollected that the trade-offs to get this improvement are the increased data rate by a factor of four, the increased system complexity, and the limited PRF availability.

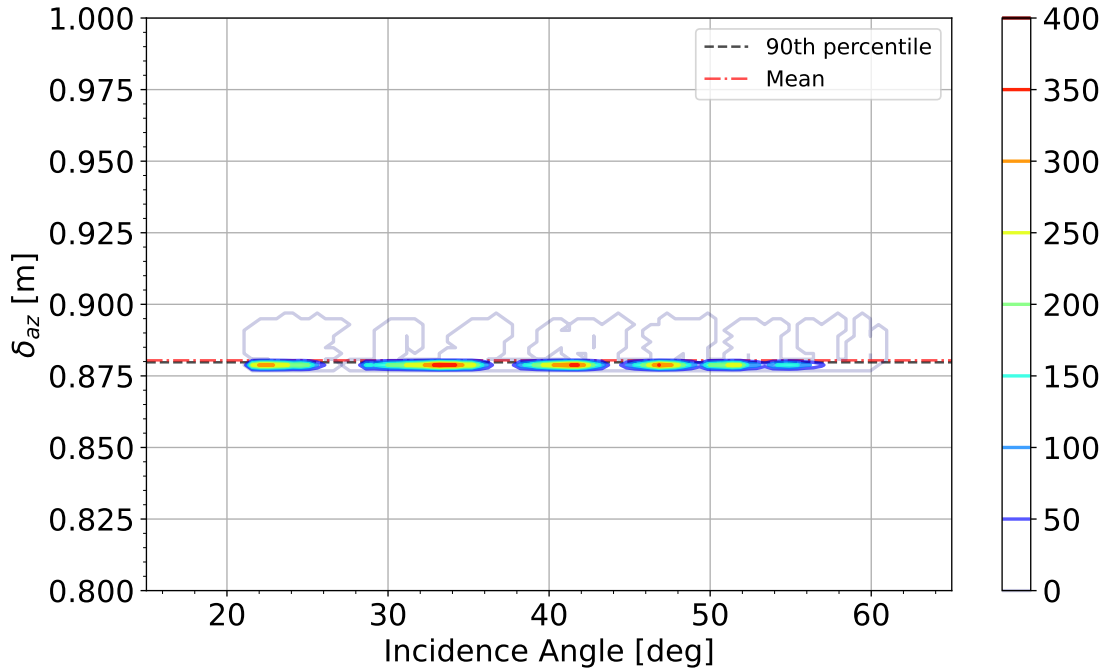


FIGURE 5.17 – Azimuth resolution as a function of the incidence angle of the scene center for the simulated targets. The selected PRF is the closest possible to the target DPCA.

Due to the PRF limitation, the AASR is consequently also more concentrated. The AASR achieved as a function of the effective PRF is depicted in Fig. 5.18. An interesting aspect of this plot is how it is indeed possible to obtain the peak of the used effective PRFs to coincide with the DPCA target, highlighted by the dotted green line. Moreover, 75 % of the possible acquisitions are within approximately ± 100 Hz of the DPCA PRF. Achieving this proximity is important as it helps to improve the quality of the azimuth reconstruction.

The AASR is mostly contained between -18 dB and -20 dB, representing a reasonably good performance. For instance, the TerraSAR-X requirement for Stripmap acquisitions is ambiguity levels better than -17 dB (EINER *et al.*, 2013).

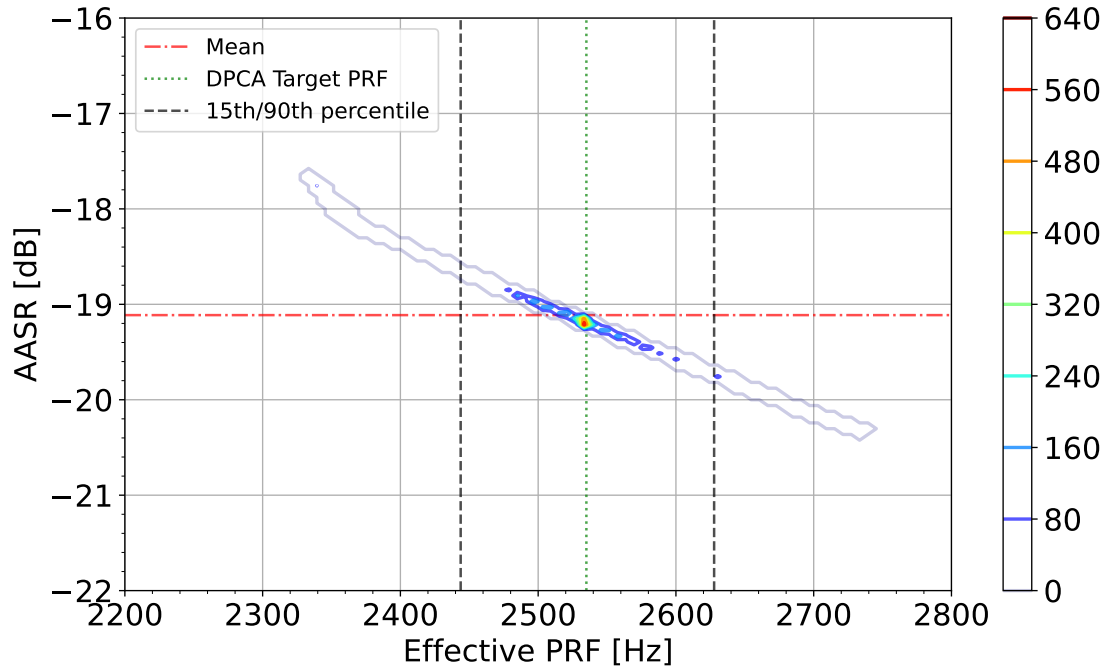


FIGURE 5.18 – AASR as a function of the effective PRF used in the acquisitions. The selected PRF is the closest possible to the target DPCA.

The plots showing the AASR as a function of the incidence angle and the distance between the targets show an invariant behavior and are, therefore, omitted here.

5.2.3 Unavailable Acquisitions

The limitation in the PRF range to allow the use of DPCA reflects directly into the global imaging availability. In the scenario and restrictions considered in this section, an availability of 75.82% was achieved. Considering the flexibility and quality of the image – simultaneous disjoint two 30 km scenes with sub-meter resolution paired with good ambiguity performance – and the relatively simple and inexpensive system compared to the DBF ones, the availability obtained is excellent.

To enable this mode for every target globally, a few possibilities can be considered. First, it is clear that reducing the scene sizes or allowing the scenes to be slightly shifted would immediately increase the availability. Alternatively, increasing the allowed PRF range would consequently also increase the availability. This approach, however, would require more careful analysis, as the image degradation of non-uniform reconstruction would be more relevant.

The latitude-by-distance histogram of the unavailable acquisitions is depicted in Fig. 5.19. As there are more unavailable acquisitions, a broader distribution is obtained. Some

concentration around specific distances is still visible, for instance, around 140 km, but overall the unavailability is quite spread over the distance and latitude domains.

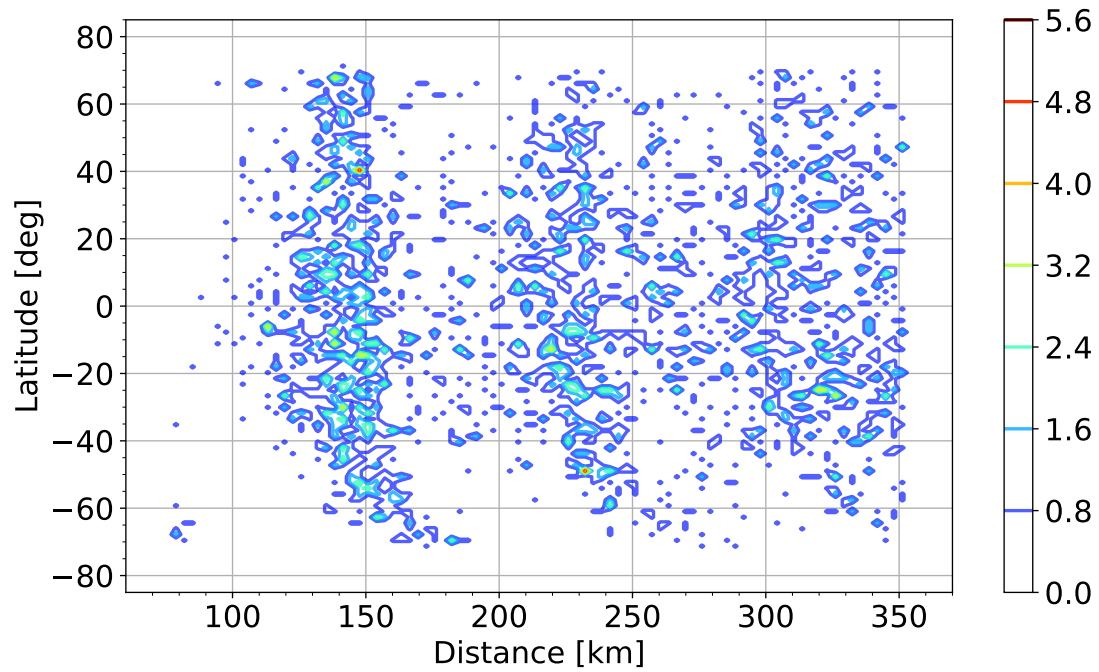


FIGURE 5.19 – Latitude-distance bivariate distribution of the unavailable targets when DPCA is considered.

6 Conclusion

6.1 Final Remarks

This thesis presented a follow-up development of the concurrent imaging mode. Techniques involving waveform encoding, MIMO channels, digital beamforming, and scanning in elevation were investigated. The frequency scanning (F-Scan) technique provided a good trade-off between cost and performance. Consequently, the application of the concurrent mode considering the F-Scan was investigated in more detail.

The proposed technique resulted in performance gains. Namely, two disjoint 30 km scenes with an average resolution of $0.78 \text{ m} \times 3.5 \text{ m}$ in ground range by azimuth were shown to be acquirable with a wide success rate of 97.90 %. Regarding ambiguities, the scenes present average ambiguity rates of -40 dB and -20 dB in range and azimuth, respectively. Moreover, the target positioning is highly flexible due to two main factors. First, they can be separated by a distance of anywhere between 80 km and 350 km. Second, the targets are not simply imaged within the scenes but are exactly at near range. This means that the targets required as input are not only the point-targets but the whole 30 km scenes, which is much harder to achieve.

Furthermore, the DPCA technique was also considered to improve the azimuth resolution without sacrificing the swath width. The DPCA leads to a new requirement, namely a more strict PRF range to allow for nearly uniform azimuth reconstruction. Naturally, this limited PRF range leads to the lower global availability of 75.8 %. In these acquisitions, however, the average resolution achieved was $0.73 \text{ m} \times 0.88 \text{ m}$ in ground range by azimuth, while the ambiguity performance is mostly unaffected.

In summary, coarsely speaking, a two dimensional average resolution of 0.65 m^2 could be obtained in three out of four scenarios. In the remaining acquisitions, this resolution is degraded to 2.7 m^2 . The ambiguities are generally not a concern, but in sensitive regions, such as water body-to-city transitions, the azimuth ambiguities may be slightly degraded and visible. These situations are possible, but with a relatively low probability, as shown in Figs. 5.11 and 5.18. In terms of sidelobe performance, the two-dimensional resolution depicted here is already degraded by the Hamming window by about 70 % to achieve

excellent sidelobe suppression in both range and azimuth (in the order of -40 dB, ideally).

The performance achieved in the concurrent mode with F-Scan and DPCA (HRWS mission antenna size and bandwidth considered) can be compared to what can be obtained with the current state-of-the-art systems, such as TerraSAR-X. Table 6.1 summarizes the performance improvement. The improved performance is depicted on the left, while the current capabilities are on the right.

From the table it becomes clear that the performance is improved in every aspect. First, the maximum distance can be increased due to the possibility of acquiring at higher incidence angles. This is a consequence of the improved range ambiguity performance brought by the F-Scan. Besides, F-Scan also helps to increase the swath width by 50%, while still achieving very high availability. In terms of resolution, the much higher bandwidth combined with DPCA leads to a roughly tenfold improvement in the two dimensional resolution. Finally, ambiguities, which were previously a big concern, now depict a very good performance.

TABLE 6.1 – Summary of the performance improvement of the concurrent imaging mode achieved with the F-Scan and DPCA in comparison with traditional Stripmap mode (RIBEIRO *et al.*, 2022). The ambiguity ratios considered are the 90th percentile.

	F-Scan (HRWS)	Traditional SM (TSX)
Antenna size	1.4 m (El.) / 6.0 m (Az.)	0.7 m (El.) / 4.8 m (Az.)
Bandwidth	1200 MHz	100 MHz
Swath width	2x 30 km	2x 20 km
Distance (swaths)	80 - 350 km	80 - 250 km
Ambiguity ratios	-32 dB (Rg.) / -17 dB (Az.)	-15 dB (Rg.) / -13 dB (Az.)
Resolution ($\theta_i = 25^\circ$)	1.15 m ² (DPCA) / 4.6 m ²	12.8 m ²
Resolution ($\theta_i = 45^\circ$)	0.45 m ² (DPCA) / 1.8 m ²	7.6 m ²
Availability rate	75.82% (DPCA) / 97.90%	~100%*

*Only obtained when giving flexibility to the position of the targets. The targets would not need to be at an specific position in the image, but anywhere within it.

Considering that this performance can be obtained with an analog/hybrid beamforming system, which is much more inexpensive than a fully digital beamforming one, the proposed technique can be considered a highly valuable tool in case of a real deployment. Moreover, it is important to highlight that the concurrent mode is not intended to be the main operational mode of the system but to serve as an auxiliary possibility in scenarios of high demand for acquisitions or tight time schedules.

6.2 Outlook for Further Work

The results obtained in this thesis already represent an improvement compared to the original concurrent mode presented in (KRAUS *et al.*, 2022; RIBEIRO *et al.*, 2022). However, there are still some points that can be further investigated.

First, the SNR is an important parameter that deserves a more in-depth analysis. However, it is highly dependent on the system parameters, so its investigation requires a higher knowledge of the real system than what was available for this thesis. Due to the bigger antenna and the scanning characteristics, the F-Scan is expected to achieve great NESZ performance (YOUNIS *et al.*, In review).

Second, the cross-nadir was considered not harmful to the final image due to the possibility of using waveform encoding techniques to eliminate it. A more comprehensive investigation of these possibilities alongside the F-Scan and the concurrent mode would be extremely valuable. This is a step that would need to be carefully done so as to allow cross-nadir interference in real systems.

Additionally, the use of DPCA raises concerns due to the non-uniform reconstruction. In this thesis, an arbitrary range of 200 Hz around the target DPCA PRF was considered. However, a thorough understanding of the azimuth losses when the effective sampling deviates from the target would allow the determination of a much better and more reliable PRF range. Therefore, this new analysis would likely change – either positively or negatively – the final availability of the mode.

Further discussion on when the F-Scan is no more worth being used compared to the traditional Stripmap mode is also of great interest. For instance, at very high incidence angles, the angular target scene size is already roughly similar to the antenna half-power beamwidth. Therefore, it may not be worth using the F-Scan in these situations as lots of energy are transmitted towards outside the target scene. This decision involves defining the parameters that must be compared in these extreme situations, such as SNR, RASR, and range resolution.

Finally, this thesis did not present the use of OFDM with F-Scan. However, such a possibility was shortly investigated and seemed promising. In typical Stripmap acquisitions, the OFDM waveforms have strong auto-correlation sidelobe peaks at distances equivalent to half the transmit pulse duration (KRIEGER *et al.*, 2012). However, with F-Scan, this effect likely does not happen because the frequency band is spread across the scene. Moreover, due to the narrower beam and the F-Scan one-to-one relation between look angle and frequency, the areas that cause the cross-correlation peaks are imaged with a much lower gain, reducing dramatically the decorrelation especially at lower incidence angles. This would remove the necessity of using DBF, allowing the use of OFDM with

F-Scan. Further investigation is required to fully understand the behavior of F-Scan with OFDM for extended scenes.

Bibliography

AGENZIA SPAZIALE ITALIANA. **COSMO-SkyMed seconda generazione:** system and products description. [Roma]: ASI, 2021.217 p. (CE-UOT-2021-002) Available at: <https://earth.esa.int/eogateway/documents/20142/37627/COSMO-SkyMed-Second-Generation-Mission-Products-Description.pdf>. Accessed on: 20 july 2021.

AKHTAR, J.; GESBERT, D. Extending orthogonal block codes with partial feedback. **IEEE Transactions on Wireless Communications**, IEEE, v. 3, p. 1959–1962, 2004. ISSN 1558-2248.

ALAMOUTI, S. A simple transmit diversity technique for wireless communications. **IEEE Journal on Selected Areas in Communications**, v. 16, n. 8, p. 1451–1458, 1998.

BACHMANN, M. **Antenna Pattern Modeling and Calibration for Spaceborne SAR Systems**. Thesis (PhD) – Karlsruher Institut für Technologie (KIT), Karlsruhe, 2015.

BALANIS, C. A. **Antenna theory: analysis and design**, 4th ed. Hoboken, NJ: Wiley, 2016. ISBN 9781118642061.

BARTUSCH, M. *et al.* HRWS: the upcoming german X-Band spaceborne SAR mission. *In: EUROPEAN CONFERENCE ON SYNTHETIC APERTURE RADAR*, 13th., 2021. **Proceedings** [...]. Berlin: VDE, 2021. p. 1–4. Online event.

BARTUSCH, M. *et al.* German X-Band spaceborne SAR heritage and the future HRWS mission. *In: IEEE INTERNATIONAL GEOSCIENCE AND REMOTE SENSING SYMPOSIUM.*, 2021, Brussels. **Proceedings** [...]. Piscataway: IEEE, 2021.

CALABRESE, D. *et al.* Discrete stepped strip (DI2S) for multi-swath acquisitions. *In: IEEE ASIA-PACIFIC CONFERENCE ON SYNTHETIC APERTURE RADAR*, 5th., 2015, Singapore: **Proceedings** [...]. Piscataway: IEEE, 2015. p. 191–195.

CARRARA, W. G.; GOODMAN, R. S.; MAJEWSKI, R. M. **Spotlight synthetic aperture radar**. Norwood, MA: Artech House, 1995.

CERUTTI-MAORI, D. *et al.* MIMO SAR processing for multichannel high-resolution wide-swath radars. **IEEE Transactions on Geoscience and Remote Sensing**, IEEE, v. 52, p. 5034–5055, 2014. ISSN 1558-0644.

- CUMMING, I. G.; WONG, F. H. **Digital signal processing of synthetic aperture radar data: algorithms and implementation**. Norwood, MA: Artech House, 2005. ISBN 9781580530583.
- CURLANDER, J.; MCDONOUGH, R. **Synthetic aperture radar: systems and signal processing**. New York: Wiley, 1991. ISBN 9780471857709.
- CURRIE, A.; BROWN, M. Wide-swath SAR. **IEE Proceedings F: Radar and Signal Processing**, v. 139, n. 2, p. 122–135, 1992.
- EINEDER, M. *et al.* (eds) **TerraSAR-X**. Ground segment. Basic product specification document. [S.l.]: DLR, 2013. 126 p. (TX-GS-DD-3302). Available at: <https://sss.terrasar-x.dlr.de/docs/TX-GS-DD-3302.pdf>. Accessed on: 25 apr. 2021.
- ESA COMMUNICATION DEPARTMENT. **Bulletin number 157**. [S. l.]: ESA, 2014. Available at: <https://esamultimedia.esa.int/multimedia/publications/ESA-Bulletin-157/offline/download.pdf>. Accessed on: 20 apr. 2021.
- GARMATYUK, D. S. Simulated imaging performance of UWB SAR based on OFDM. *In: IEEE INTERNATIONAL CONFERENCE ON ULTRA-WIDEBAND*, 2006, Waltham. **Proceedings** [...]. Piscataway: IEEE, 2006. p. 237–242.
- GEBERT, N.; KRIEGER, G.; MOREIRA, A. Digital beamforming on receive: Techniques and optimization strategies for high-resolution wide-swath SAR imaging. **IEEE Transactions on Aerospace and Electronic Systems**, v. 45, n. 2, p. 564–592, Apr 2009.
- HARRIS, F. On the use of windows for harmonic analysis with the discrete fourier transform. **Proceedings of the IEEE**, Institute of Electrical and Electronics Engineers (IEEE), v. 66, n. 1, p. 51–83, 1978.
- HE, F.; DONG, Z.; LIANG, D. A novel space–time coding Alamouti waveform scheme for MIMO-SAR implementation. **IEEE Geoscience and Remote Sensing Letters**, v. 12, n. 2, p. 229–233, Feb 2015.
- HISDESAT. **PAZ image product guide**. 2.0. Madri: Hisdesat Servicios Estratégicos, 2021. (PAZ-HDS-GUI-001) Available at: <https://www.hisdesat.es/wp-content/uploads/2021/06/PAZ-HDS-GUI-001-PAZ-Image-Products-Guide-issue-2.pdf>. Accessed on: 25 July 2021.
- HUBER, S. *et al.* Tandem-L: A technical perspective on future spaceborne SAR sensors for Earth observation. **IEEE Transactions on Geoscience and Remote Sensing**, v. 56, n. 8, p. 4792–4807, Aug 2018.
- KAHLE, R.; D’AMICO, S. The TerraSAR-X precise orbit control - concept and flight results. *In: International Symposium on Space Flight Dynamics (ISSFD)*. Laurel, MD: [s.n.], 2014.
- KIM, J.; WIESBECK, W. Investigation of a new multifunctional high performance SAR system concept exploiting MIMO technology. *In: IEEE INTERNATIONAL GEOSCIENCE AND REMOTE SENSING SYMPOSIUM*, 2008, Boston. **Proceedings** [...]. Piscataway: IEEE, 2008.

- KIM, J. *et al.* A novel OFDM waveform for fully polarimetric SAR data acquisition. *In: EUROPEAN CONFERENCE ON SYNTHETIC APERTURE RADAR*. 8th., 2010, Aachen. **Proceedings** [...]. Berlin: VDE, 2010. p. 1–4.
- KIM, J.-H. *et al.* A novel OFDM chirp waveform scheme for use of multiple transmitters in SAR. **IEEE Geoscience and Remote Sensing Letters**, v. 10, n. 3, p. 568–572, May 2013.
- KIM, J.-H. *et al.* Spaceborne MIMO synthetic aperture radar for multimodal operation. **IEEE Transactions on Geoscience and Remote Sensing**, v. 53, n. 5, p. 2453–2466, May 2015.
- KRAUS, T. *et al.* TerraSAR-X staring spotlight mode optimization and global performance predictions. **IEEE Journal of Selected Topics in Applied Earth Observations and Remote Sensing**, v. 9, n. 3, p. 1015–1027, 2016.
- KRAUS, T. *et al.* Concurrent imaging for TerraSAR-X: wide-area imaging paired with high-resolution capabilities. **IEEE Transactions on Geoscience and Remote Sensing**, v. 60, n. 5220314, Jan. 2022.
- KRIEGER, G. MIMO-SAR: opportunities and pitfalls. **IEEE Transactions on Geoscience and Remote Sensing**, v. 52, n. 5, p. 2628–2645, May 2014.
- KRIEGER, G.; GEBERT, N.; MOREIRA, A. Unambiguous SAR signal reconstruction from nonuniform displaced phase center sampling. **IEEE Geoscience and Remote Sensing Letters**, v. 1, n. 4, p. 260–264, Oct 2004.
- KRIEGER, G. *et al.* MIMO-SAR and the orthogonality confusion. *In: IEEE INTERNATIONAL GEOSCIENCE AND REMOTE SENSING SYMPOSIUM*, 2012, Munich. **Proceedings** [...]. Piscataway: IEEE, 2012.
- LIU, S.; ZHANG, Z.; YU, W. A space-time coding scheme with time and frequency comb-like chirp waveforms for MIMO-SAR. **IEEE Journal of Selected Topics in Signal Processing**, v. 11, n. 2, p. 391–403, Mar 2017.
- MACHADO, R.; UCHOA-FILHO, B. A hybrid transmit antenna/code selection scheme using space-time block codes. *In: 2004 IEEE Wireless Communications and Networking Conference*. Atlanta, GA, USA: IEEE, 2004.
- META, A. *et al.* TOPS imaging with TerraSAR-X: Mode design and performance analysis. **IEEE Transactions on Geoscience and Remote Sensing**, v. 48, n. 2, p. 759–769, Feb 2010.
- MITTERMAYER, J. *et al.* MirrorSAR: An HRWS add-on for single-pass multi-baseline SAR interferometry. **IEEE Transactions on Geoscience and Remote Sensing**, v. 60, p. 1–18, 2022.
- MITTERMAYER, J. *et al.* The TerraSAR-X staring spotlight mode concept. **IEEE Transactions on Geoscience and Remote Sensing**, v. 52, p. 3695–3706, 2014.
- MOREIRA, A. *et al.* Tandem-L: A highly innovative bistatic SAR mission for global observation of dynamic processes on the Earth's surface. **IEEE Geoscience and Remote Sensing Magazine**, v. 3, n. 2, p. 8–23, Jun 2015.

MOREIRA, A. *et al.* A tutorial on synthetic aperture radar. **IEEE Geoscience and Remote Sensing Magazine**, v. 1, n. 1, p. 6–43, Mar 2013.

NASA. **NISAR**: GET to know SAR: Overview. [Washington, DC]: NASA, Available at: <https://nisar.jpl.nasa.gov/mission/get-to-know-sar/overview>. Accessed on: 04 Apr. 2021.

NATIONAL IMAGERY AND MAPPING AGENCY. **Technical Report 8350.2 Third Edition**. [S.l.], 2000. Available at: <https://gis-lab.info/docs/nima-tr8350.2-wgs84fin.pdf>.

RIBEIRO, J. P. T. *et al.* Multiple PRI technique for concurrent imaging mode using TerraSAR-X. *In*: IEEE RADAR CONFERENCE, 2022, New York. **Proceedings** [...]. Piscataway: IEEE, 2022.

ROEMER, C. Introduction to a new wide area SAR mode using the F-SCAN principle. *In*: IEEE INTERNATIONAL GEOSCIENCE AND REMOTE SENSING SYMPOSIUM, 2017, Fort Worth. **Proceedings** [...]. Piscataway: IEEE, 2017. p. 3844–3847.

ROEMER, C. **HIGH resolution wide swath synthetic aperture system**. Applicant: Airbus Defence and Space GmbH. WO 2019/015911 A1. Publication Date: 24 Jan 2019.

ROEMER, C. *et al.* Frequency scanning applied to wide area SAR imaging. *In*: EUROPEAN CONFERENCE ON SYNTHETIC APERTURE RADAR, 12th, 2018, Aachen. **Proceedings** [...]. Berlin: VDE, 2018. p. 1–5.

SUESS, M.; GRAFMUELLER, B.; ZAHN, R. A novel high resolution, wide swath SAR system. *In*: IEEE INTERNATIONAL GEOSCIENCE AND REMOTE SENSING SYMPOSIUM, 2001, Sydney. **Proceedings** [...]. Piscataway: IEEE, 2001. p. 1013–1015

SUESS, M.; WERNER WIESBACK, W. **Side-looking synthetic aperture radar system**. Applicant: EADS Astrium GmbH. EP 1 241 487 B1. Publication Date: 18 Sept. 2002.

ULABY, F.; DOBSON, M. C. **Handbook of Radar Scattering Statistics for Terrain**. Norwood, MA: Artech House, 1988.

VILLANO, M.; KRIEGER, G.; MOREIRA, A. Staggered SAR: High-resolution wide-swath imaging by continuous PRI variation. **IEEE Transactions on Geoscience and Remote Sensing**, v. 52, n. 7, p. 4462–4479, Jul. 2014.

VILLANO, M.; KRIEGER, G.; MOREIRA, A. Nadir echo removal in synthetic aperture radar via waveform diversity and dual-focus postprocessing. **IEEE Geoscience and Remote Sensing Letters**, v. 15, n. 5, p. 719–723, Mar 2018.

WANG, W.-Q. Space–time coding MIMO-OFDM SAR for high-resolution imaging. **IEEE Transactions on Geoscience and Remote Sensing**, v. 49, n. 8, p. 3094–3104, Aug 2011.

WILEY, C. A. Synthetic aperture radars. **IEEE Transactions on Aerospace and Electronic Systems**, AES-21, n. 3, p. 440–443, 1985.

WITTING, M. *et al.* Status of the european data relay satellite system. *In*: International Conference on Space Optical Systems and Applications (ICSOS), 2012, Ajaccio. **Proceedings** [...]. Piscataway: IEEE, 2012.

WOLLSTADT, S.; MITTERMAYER, J. Nadir margins in TerraSAR-X timing commanding. *In*: **Proceedings of the Committee on Earth Observation Satellites (CEOS)**. [S.l.: s.n.], 2008. p. 4.

YOUNIS, M. *et al.* Frequency scan for time-of-echo compression in sar systems. *In*: IEEE INTERNATIONAL GEOSCIENCE AND REMOTE SENSING SYMPOSIUM, 2021, Brussels. **Proceedings** [...]. Piscataway: IEEE, 2021.

YOUNIS, M. *et al.* A synthetic aperture radar imaging mode utilizing frequency scan for time-of-echo compression. In review.

YOUNIS, M.; LOPEZ-DEKKER, P.; KRIEGER, G. MIMO SAR operation modes and techniques. *In*: EUROPEAN CONFERENCE ON SYNTHETIC APERTURE RADAR, 10th, 2014, Berlin. **Proceedings** [...]. Berlin: VDE, 2014. p. 1–3.

ZAN, F. D.; GUARNIERI, A. M. TOPSAR: Terrain observation by progressive scans. **IEEE Transactions on Geoscience and Remote Sensing**, v. 44, n. 9, p. 2352–2360, Sep 2006.

FOLHA DE REGISTRO DO DOCUMENTO

1. CLASSIFICAÇÃO/TIPO DM	2. DATA 28 de novembro de 2022	3. DOCUMENTO Nº DCTA/ITA/DM-127/2022	4. Nº DE PÁGINAS 129
5. TÍTULO E SUBTÍTULO: Concurrent Imaging Mode Applied to High-Resolution Wide-Swath SAR Imaging			
6. AUTOR(ES): João Pedro Turchetti Ribeiro			
7. INSTITUIÇÃO(ÕES)/ÓRGÃO(S) INTERNO(S)/DIVISÃO(ÕES): Instituto Tecnológico de Aeronáutica – ITA			
8. PALAVRAS-CHAVE SUGERIDAS PELO AUTOR: Synthetic Aperture Radar (SAR); Concurrent Imaging Mode; TerraSAR-X; Ambiguities; Timing Analysis; F-Scan			
9. PALAVRAS-CHAVE RESULTANTES DE INDEXAÇÃO: Radar de abertura sintética; Processamento de imagens; Solução de ambiguidades inteiras; Rastreamento (posição); Telecomunicações; Engenharia eletrônica.			
10. APRESENTAÇÃO: (X) Nacional () Internacional ITA, São José dos Campos. Curso de Mestrado. Programa de Pós-Graduação em Engenharia Eletrônica e Computação. Área de Telecomunicações. Orientador: Prof. Dr. Renato Machado. Coorientador: Thomas Kraus. Defesa em 23/11/2022. Publicada em 2022.			
11. RESUMO: <p>Radar de abertura sintética (SAR) está gradualmente se tornando a referência no imageamento da superfície terrestre devido à sua funcionalidade em qualquer condição climática e independência da luz solar. A sua crescente qualidade de imagem atrelada às capacidades de polarimetria, interferometria e tomografia o tornam uma solução tecnológica bastante atrativa para o monitoramento contínuo de fenômenos globais (tais como derretimento de geleiras, desmatamento e cobertura de gelo marítimo), vigilância, agricultura e outras diversas aplicações. Dessa forma, o imageamento de faixas largas com alta resolução (HRWS) é uma linha de pesquisa essencial para a futura geração de sistemas SAR.</p> <p>Uma das técnicas recentemente propostas para aumentar a capacidade e flexibilidade dos sistemas é o modo de imageamento simultâneo. Esse modo permite aquisições simultâneas de duas áreas por meio do aumento da frequência de repetição de pulso e intercalando a transmissão e recepção de ambos os modos pulso a pulso. Devido a limitações intrínsecas de sistema, essa técnica aplicada a sistemas operacionais atuais, tal como o satélite alemão TerraSAR-X, apresenta fortes compromissos em termos de uma largura de faixa mais limitada e um aumento dos níveis de ambiguidade.</p> <p>Nesta dissertação de mestrado, várias técnicas são investigadas a fim de aprimorar o modo de imageamento simultâneo considerando o escopo da próxima geração de sistemas SAR. Dado que esses sistemas ainda estão em desenvolvimento e não há restrições estritas sobre o que está disponível, uma vasta gama de tecnologias e possibilidades são analisadas neste trabalho, como multiplexação por divisão de frequência ortogonal (OFDM), varredura de frequência (F-Scan) e técnica de antena de centros de fase deslocada (DPCA). O F-Scan demonstrou cumprir bem os requisitos, alcançando melhorias significativas não apenas no desempenho do alcance, mas também no tamanho da cena, tudo isso em um sistema relativamente simples e barato. Finalmente, simulações de desempenho global e previsões de melhoria são realizadas no âmbito da próxima missão alemã em banda X HRWS, que está planejada para usar o F-Scan operacionalmente.</p>			
12. GRAU DE SIGILO: (X) OSTENSIVO () RESERVADO () SECRETO			